University of Zagreb

Faculty of Science

Department of Physics

Mateo Kruljac

CAVITY COOLING AND

SELF-ORGANIZATION OF ATOMS USING

AN OPTICAL FREQUENCY COMB

DOCTORAL DISSERTATION

Zagreb, 2022

University of Zagreb

Faculty of Science

Department of Physics

Mateo Kruljac

CAVITY COOLING AND

SELF-ORGANIZATION OF ATOMS USING

AN OPTICAL FREQUENCY COMB

DOCTORAL DISSERTATION

Supervisor:

dr. sc. Ticijana Ban

Zagreb, 2022

Sveučilište u Zagrebu
Prirodoslovno-matematički fakultet
Fizički odsjek

Mateo Kruljac

HLAĐENJE I SAMOORGANIZACIJA ATOMA U OPTIČKOM REZONATORU KORIŠTENJEM OPTIČKOG FREKVENTNOG ČEŠLJA

DOKTORSKI RAD

Mentor:
dr. sc. Ticijana Ban

Zagreb, 2022

Supervisor information

Dr. sc. Ticijana Ban was born in Pula, Croatia in 1972. She graduated from the Faculty of Science at the University of Zagreb in 1997 with a degree in Physics. She received her PhD in Physics in 2003 with the doctoral thesis titled: "Photoassociation and Photodissociation of Alkali Molecules" with dr. sc. Goran Pichler as her supervisor. Under the Fulbright research grant in 2010 she worked as a visiting scientist at JILA (Boulder, Colorado) in the group of Prof. Jun Ye. She is currently employed as a Permanent Senior Scientist at the Institute of Physics in Zagreb where she leads the Quantum technologies group, and is currently serving as a Deputy director. Her main scientific interests include experimental studies of the interaction of cold atoms inside high-finesse optical resonators with frequency comb excitation, and quantum memories based on electromagnetically-induced transparency in hot rubidium vapours.

Acknowledgements

Abstract

In this thesis I present the results of research on two topics in the field of cold atomic ensembles interacting with laser light. In both cases we use a mode-locked femtosecond laser, whose spectrum generates a frequency comb (FC), to induce light forces on the atoms.

In the first part of the thesis, we investigate the FC-induced force in dense ensembles of cold atoms in free space. We report a modification of the light force compared to single-atom physics, which is a signature of collective effects. We conclude that the dominant contribution to the modification of the FC-induced force is the attenuation of beam intensity as it propagates through the cloud, according to the Beer-Lambert law. We show that the models developed for the interaction of cold atoms and continuous-wave (cw) lasers can be used to explain the measured FC force. The understanding of FC-induced force is significant for experiments employing FC cooling of atoms, and for demonstration of multi-mode quantum memories.

In the second part of the thesis, I present the results of interaction of cold atoms inside a high-finesse optical cavity, using cw and FC excitation in longitudinal geometry (pumping through the cavity mirrors). For the case of cw pump, we measured a bimodal spatial distribution of atoms, a clear signature of the interaction of atoms with the intra-cavity optical potential. To distinguish between cavity effects and the loading of atoms in a conservative lattice potential, we use numerical calculations, which simulate the experimental results very well. Using an FC in longitudinal geometry, we report on the interaction of cold atoms with a multitude of off-resonant FC modes, seen as enhancement or reduction of transmitted FC light due to dispersive action of atoms. We also measured the effects of interaction in the spatial distribution of atoms, pointing to the possibility of a cavity-enhanced cooling, heating or trapping of atoms using off-resonant FC modes. In the final part, we present the results of transversal pumping geometry using an FC. These results open a way to new research of developing and implementing cavity cooling and trapping techniques using multi-mode excitation.

Keywords: optical frequency comb, cold atoms, dense atomic ensembles, optical cavity, cavity cooling of atoms, collective light-atom interaction

Prošireni sažetak

U ovome doktorskom radu predstavljeni su rezultati istraživanja u Grupi za kvantne tehnologije na Institutu za fiziku, pod mentorstvom dr. sc. Ticijane Ban. Istraživanje je započeto u sklopu HrZZ projekta „Optomehanika uzrokovana frekventnim češljem", a obuhvaća eksperimentalni rad u području hladnih atoma nastalih u magneto-optičkoj stupici s ciljem istraživanja radijativnih sila na hladne atome koje nastaju kao rezultat obasjavanja atoma laserskom svjetlošću kontinuiranog i pulsnog zračenja. Doktorski rad podijeljen je tematski u dvije cjeline. U prvoj cjelini istražuje se radijativna sila uzrokovana optičkim frekventnim češljem na gusti oblak hladnih atoma koji se nalazi u slobodnom prostoru. Cilj ovog istraživanja bio je proučavanje utjecaja kolektivnih efekata na radijativnu silu uzrokovanu pulsnom pobudom. U drugoj cjelini atomi su smješteni unutar visoko-reflektirajućeg optičkog rezonatora te obasjani frekventnim češljem u longitudinalnoj geometriji (pumpanjem kroz zrcala rezonatora) i transverzalnoj geometriji. Cilj ovog istraživanja bio je ispitati utjecaj kompleksnog potencijala koji nastaje vezanjem frekventnog češlja i modova optičkog rezonatora na hladne atome. Očekuje se da takav potencijal dovodi do hlađenja i zarobljavanja atoma potpomognutih optičkim rezonatorom. U ovom doktorskom radu po prvi se put izgradio eksperiment koji omogućava proučavanje dinamike hladnih atoma u kompleksnom optičkom potencijalu unutar multi-modnog optičkog rezonatora i po prvi su put opaženi efekti interakcije hladnih atoma s poljem frekventnog češlja unutar visoko-reflektirajućeg rezonatora. Navedena eksperimentalna istraživanja jedinstvena su u dosadašnjoj literaturi i predstavljaju glavni rezultat ovog doktorskog rada.

Doktorski rad organiziran je na sljedeći način.

U Uvodu se obrazlažu područje i ciljevi istraživanja iz obje tematike rada, te sadržaj doktorskog rada.

U drugome poglavlju uvode se teorijski formalizam i osnovni pojmovi nužni za razumijevanje tematike istraživanja. Teorijski dio obuhvaća opis radijativnih sila na atome, svojstva optičkih rezonatora i frekventnog češlja, kao i kvantno-mehanički pristup interakcije atoma i svjetlosti u rezonatoru, a koji daje uvid u nove efekte poput hlađenja i samo-organizacije atoma.

U trećem poglavlju istražuje se radijativna sila na atome inducirana frekventnim češljem

u gustom oblaku hladnih atoma u slobodnom prostoru. Opažena je promjena sile u odnosu na rijetki oblak, što ukazuje na postojanje kolektivnih efekata. Ispitan je utjecaj koherentnih i ne-koherentnih kolektivnih efekata te je zaključeno da je dominantan doprinos promjeni sile u gustom oblaku atoma rezultat Beer-Lambertovog zakona koji opisuje atenuaciju svjetlosti pri propagaciji kroz gusti medij, a rezultat je više-brojnog raspršenja svjetlosti unutar gustog medija. Dodatno, pokazano je da se eksperimentalni rezultati mogu objasniti modelima koji su razvijeni za slučaj međudjelovanja hladnih atoma i lasera kontinuiranog zračenja, što ukazuje da, za dane eksperimentalne parametre, od mnoštva spektralnih modova optičkog frekventnog češlja dominantno međudjelovanje s atomima dolazi prvenstveno od jednog moda i to onog koji je najbliže atomskoj rezonanciji. Razumijevanje radijativne sile u gustim oblacima hladnih atoma značajno je za eksperimente hlađenja atoma frekventnim češljem, kao i za eksperimente u kojima se frekventni češalj planira koristiti za demonstraciju multi-modnih kvantnih memorija.

U četvrtom poglavlju prikazani su rezultati istraživanja koji su provedeni na sistemu hladnih atoma smještenih unutar visoko-reflektirajućeg rezonatora, a koji su obasjavani laserom konti-nuirane emisije i optičkim frekventnim češljem u longitudinalnoj geometriji (pumpanje kroz zrcalo rezonatora). Cilj istraživanja bio je razumjeti efekte potaknute optičkim rezonatorom kada se atomi obasjavaju izvorom svjetlosti kao što je optički frekventni češalj, koji omogućuje istovremeno sprezanje nekoliko tisuća spektralnih modova s modovima optičkog rezonatora. Pri tome, atomi smješteni unutar rezonatora ne vide klasični sinusni optički potencijal kao u slučaju lasera kontinuiranog zračenja, već optički potencijal unutar rezonatora može poprimiti kompleksnu strukturu što otvara vrata novim eksperimentima u području kvantnih simulatora usmjerenih prema rješavanju problema optimizacije. Ispitivanje se prvo vršilo s laserom konti-nuiranog zračenja kako bi se moglo nedvojbeno zaključiti o efektima koji su posljedica multi-komponentnog optičkog frekventnog češlja. Eksperiment se provodio za različite uvjete veza-nja svjelosti lasera i atoma, različite snage pumpnog lasera te za guste i rijetke oblake atoma s temperaturama ispod i iznad Dopplerove temperature. U slučaju interakcije s laserom kontinu-iranog zračenja, u specifičnim eksperimentalnim uvjetima uočena je bimodalna prostorna ras-podjela atoma koja je ostala postojana i prilikom slobodne ekspanzije atoma mjerene tehnikom vremena proleta (TOF). U svrhu razumijevanja opaženih rezultata, a prvenstveno da se razluče efekti koji dolaze kao posljedica zarobljavanja atoma u potencijal optičke rešetke unutar rezona-tora od onih koji su posljedica utjecaja rezonatora na dinamiku atoma, korišten je već razvijeni numerički kod koji se prilagodio za dane eksperimentalne parametre. Pokazano je da se opaženi efekt bimodalne distribucije u potpunosti može opisati zarobljavanjem atoma u sinusni optički potencijal unutar rezonatora. Koristeći frekventni češalj za longitudinalnu pobudu, opažen je efekt istovremene interakcije hladnih atoma smještenih unutar rezonatora i niza ne-rezonantnih

modova frekventnog češlja u vidu povećanja i smanjenja intenziteta transmitirane svjetlosti zbog disperzivnog utjecaja atoma na modove optičkog rezonatora. Ovi rezultati predstavljaju prvu eksperimentalnu realizaciju multi-modnog pobuđenja atoma unutar visoko-reflektirajućeg rezonatora. Osim u transmisiji, potpis interakcije opaža se i u prostornoj distribuciji atoma mjerenoj TOF tehnikom koja nam daje direktan uvid u brzinsku distribuciju atoma. Opaženi su efekti smanjenja i povećanja širine distribucije brzine atoma kao posljedice njihovog pobuđenja s frekventnim češljem, što može ukazivati na mehanizme rezonatorom potpomognutog hlađenja i grijanja atoma, ali i na mehanizme zarobljavanja u optički potencijal unutar rezonatora. Kako bi se jasno razlučilo između ova dva mehanizma, ispitana je i geometrija transverzalnog pumpanja atoma u rezonatoru upotrebom optičkog frekventnog češlja, u kojoj ne postoji optički potencijal unutar rezonatora koji je odgovoran za zarobljavanje atoma te se dominantan efekt rezonatora očituje na dinamici atoma, tj. smanjenju ili povećanju kinetičke energije atoma unutar rezonatora. Rezultati su prikazani na kraju doktorskog rada te otvaraju niz novih pitanja i mogućnosti za daljnja istraživanja.

U petome poglavlju dan je zaključni pregled rezultata ovog doktorskog rada, kao i perspektive za daljnja istraživanja i rješavanje pitanja koje je moj dosadašnji rad pokrenuo.

Ključne riječi: optički frekventni češalj, hladni atomi, gusti atomski ansambl, optički rezonator, hlađenje atoma u rezonatoru, kolektivna interakcija atoma i svjetlosti

Contents

List of Figures

Chapter 1

Introduction

1.1   Cold atoms and cavity quantum electrodynamics

Mechanical action of continuous wave (cw) laser radiation on atoms presents a central part of research in atomic physics for the last few decades. Radiation pressure force is a foundation of laser cooling and trapping of atoms, which allowed the creation of dense and cold atomic samples [1], opening a way to a whole new and exciting field of research. The pioneers of this field, S. Chu, W. D. Phillips and C. Cohen-Tannoudji won the Nobel prize in 1997 [2]. Cold atomic samples started the development and research of quantum sensors, optical atomic clocks and quantum many-body simulation. Further cooling and trapping techniques allowed the creation of new states of matter, like Bose-Einstein Condensate (BEC), degenerate Fermi and Bose-Fermi gases, which set a foundation of a very prosperous and productive area of modern science. For the realization of a BEC, the Nobel prize was awarded to W. Ketterle, C. Wieman and E. A. Cornell in 2001 [3]. Cold samples with the temperature on the order of $\sim 100~\mu$K prepared in a magneto-optical trap (MOT) became a standard experimental setup in many laboratories. These experiments are of high interest due to their controllability. The cold samples are inside a high-vacuum chamber, so any external perturbations are removed. Likewise, there are no losses due to collisions with surrounding gases. The low temperature means the atoms are very slow and can be manipulated on time scales of dozens on miliseconds. Low temperatures allow even the manipulation of single atoms with laser-generated forces.

The standard cooling technique in a MOT is called Doppler cooling. It is achieved by a preferred absorption of photons from a laser beam counter-propagating to the atomic motion. Momentum transferred from the photon to the atom through absorption is so weak that thousands of cycles of absorption and emission (i.e. cooling cycles) are needed to slow down the atom significantly. For this reason it is important for the excited atom to decay into the ground

energy state, that is, a closed cooling transition is needed. For atoms with a simple energy structure it is possible to meet this condition, which makes alkali metals the main samples for laser cooling. Another important limitation is the availability of laser sources at wavelengths needed for closed transitions. For example, hydrogen atoms have the simplest energy structure, but the transition is in deep VUV region where generation of laser light is demanding. Due to these limitations, only a handful of atomic species have been directly laser cooled, and are shown in Fig. 1.1. Development of alternative cooling techniques that would be independent of the internal structure would be of importance for direct laser cooling of molecules, which would be of great interest to the scientific community.

Figure 1.1: Elements that have been directly laser cooled are marked in blue. Taken from [4].

Cavity-optomechanical systems with one atom and a cold atomic ensemble are used to demonstrate numerous phenomena [5], among which are cooling and self-organization of atoms into regular structures. Cavity cooling of one atom, as well as an atomic ensemble, presents a unique cooling technique which is independent of atomic energy structure. This technique is based on energy conservation during the scattering of a photon on an atom, where the energy of a scattered photon is higher than of an input photon, which is accompanied by a decrease of atomic velocity. The scattering is enhanced if the atom is located in an optical resonator whose mode frequency is higher than input radiation frequency. The cooling mechanism is based on the loss of scattered photons from the optical resonator (as opposed to Doppler cooling where

spontaneous emission from an excited atomic state is the dissipation mechanism), and depends on the resonator mirror reflectivity and on the detuning of input photon frequency from the cavity mode frequency. The cooling process is independent of the detuning of the input light from an atomic resonance (although it affects the cooling speed). This kind of cooling mechanism is then applicable to all scatterers of light regardless of their internal structure, which makes it an invaluable tool in laser cooling, and an area of great research interest for the past twenty years [6]. Experimentally, cavity cooling [7, 8] and self-organization of cold atoms [9] and BEC [10] have been demonstrated, as well as cooling of free silicon nanoparticles in high vacuum [11] and levitating nanospheres [12]. The efficiency of cavity cooling increases with laser power used for cooling, but only up to a certain point. Above a certain threshold power, the scattered photons create potential wells deep enough for the atoms to self-organize into regular structures and get trapped in the standing wave potential, which slows down the cooling and lowers its efficiency [13]. Self-organization of atoms is an unwanted effect if the goal is higher cooling efficiency compared to heating and diffusion effects, which is one of the main limitations in implementing this technique for wider use. The final goal to realize a simple and efficient method of cooling fully independent of the systems optical transition details, which would allow the creation of large samples of ultracold complex molecules [14], still remains unrealized.

1.2　Frequency comb cooling

The limitation of availability of laser sources has been tackled on historically by discussing the use of pulsed lasers instead of continuous wave (cw) lasers. The pulses have high peak electric field strengths, which makes them suitable for nonlinear optics [15]. Pulsed sources can produce higher frequency harmonics [16], which can broaden the pulse spectrum, stretching it into UV and further. For this reason, the use of pulsed lasers for cooling has been explored early on. However, since the pulses are short in the time domain, their frequency spectrum is wide. For Doppler cooling, when the laser interacts with a single atomic resonance, most of the power will be wasted or misplaced, since some frequencies will be below and some above the atomic transition, making the Doppler cooling scheme inefficient or even impossible.

Using stabilized mode-locked lasers, that produce phase-stable train of pico- or femtosecond pulses of high repetition rates, circumvents the mentioned problems. In frequency domain, a mode-locked laser consists of a large number of equidistant narrow lines, hence the name frequency comb. Due to their pulsed nature, mode-locked lasers can be stretched in frequency, while preserving the regular comb structure. Now, each frequency in the spectrum is known with high precision and for suitable configurations Doppler cooling scheme can readily be ap-

plied, since only one comb mode will dominantly interact with the atoms. Using the frequency comb effectively corresponds to using a large number of phase-coherent cw lasers, opening a way to simultaneous multi-line excitation. Application of frequency comb cooling has been demonstrated theoretically and experimentally [17, 18, 19]. Recently, our group has demonstrated simultaneous two-species cooling using an optical frequency comb [20]. Other novel frequency comb applications include multi-mode quantum memories [21, 22] and quantum computing [23, 24]. The use of frequency combs has already revolutionized metrology by allowing high-precision measurements of optical frequencies. For the development of frequency combs, John L. Hall and Theodor W. Hänsch shared the Nobel prize in 2005 [25].

A novel application of frequency combs was recently predicted in a paper [26] in the context of cavity cooling of atoms. Since the frequency comb consists of a large number of equally spaced modes (over 100 000), all of them can be simultaneously coupled into different cavity modes. Owing to the large number of different wavelengths, the standing wave of a pulsed laser, and with it the potential seen by the atoms, becomes far more complex. Because of this complex potential, self-organization threshold intensity moves to higher values, which should allow a more efficient use of higher laser powers, and with it, more efficient cavity cooling. Likewise, trapping of atoms in such potentials could be used to simulate various open systems, manipulation of a BEC in a complex potential, and quantum annealing [27].

For all these applications, detailed understanding of the laser-atom interaction and the laser-induced forces is necessary. In this thesis, we investigate the modification of the frequency-induced free-space force when atomic samples of high density are considered. In the second part of the thesis we investigate the collective dynamics of cold atoms situated inside an optical cavity, while interacting with frequency comb light coupled with the cavity modes.

1.3 Thesis outline

This thesis is organized as follows.

In the Introduction, I present the field of cold atoms and the goals of my research.

In the second chapter, I introduce the theoretical formalism and basic concepts necessary to understand the topics and results of this thesis. The theoretical chapter covers a description of laser-induced forces on atoms, general properties of optical cavities and frequency combs, as well as a fully quantum approach to light-atom-cavity interaction, which gives insight into predictions of cavity-enhanced cooling and trapping of atoms.

In the third chapter I investigate the FC-induced radiation pressure force in dense atomic ensembles in free space. We report on the modification of the FC force compared to single-atom

physics, a signature of collective effects. We analyse contributions of different coherent and incoherent effects and compare them to the experimental data, concluding that the progressive attenuation of beam intensity as it propagates through the cloud, due to Beer-Lambert law, is the dominant mechanism responsible for the modification of the FC-force.

In the fourth chapter, the atoms are in the center of a high-finesse resonator, interacting with cw or FC pump in longitudinal geometry (pumping through the cavity mirrors). The chapter is divided in two parts - cw pump and FC pump. For the case of cw pump, we conclude that the measured bimodal spatial distribution of atoms is a consequence of loading of atoms in the conservative optical lattice potential. For the case of the FC pump, we report on several signatures of interaction of atoms with intra-cavity FC light, which is the first experimental realization of multi-mode excitation of cold atoms inside a high-finesse optical cavity, and points to a possibility of cavity-enhanced FC cooling and trapping of atoms.

In the last chapter, I summarize the results presented in this thesis and give an outlook on the plans and future experiments.

Chapter 2

Theory

In this chapter I cover the theoretical treatment of different topics and phenomena introduced through this thesis. These topics are covered in more detail in several books, from which we borrow and expand upon. The basic quantum mechanic formalism of laser-atom interaction, principles of laser cooling and trapping of atoms, as well as the details of magneto-optical traps (MOTs) can be found in "Laser Cooling and Trapping" by H. J. Metcalf and P. van der Straten [1]. Properties of optical cavities are described in most detail in "Laser Resonators and Beam Propagation" by N. Hodgson and H. Webber [28]. The fully quantum mechanical treatment of laser-atom interaction and the quantization of light can be found in "Quantum Optics" by M. Scully [29]. A good description of pulsed lasers and frequency comb generation is presented in "Quantum Electronics for Atomic Physics and Telecommunication" by W. Nagourney [30]. The last book also contains a good cover of optical cavities and light-atom interaction.

2.1 Light forces acting on atoms

2.1.1 Basic formalism and equations

We first consider a two-level atom interacting with a classical laser field in free space. Since the laser field consists of a large number of photons, it is sufficient to describe it as a classical light field:

$$\mathbf{E}(x,t) = \frac{1}{2}\boldsymbol{\epsilon}E_0(x)e^{-i(\omega_L t - \phi(x))} + c.c, \tag{2.1}$$

where $\phi(x)$ is a space-dependent phase, $E_0(x)$ space-dependent amplitude, $\boldsymbol{\epsilon}$ the polarization of the field, and $c.c.$ denotes the complex conjugate of the written expression. Let us label the energy states of the atom the ground state $|g\rangle$ and the excited state $|e\rangle$, and the transition

frequency between them ω_0. The Hamiltonian of this system can be written as:

$$\hat{H} = \hat{H}_A + \hat{H}_I, \tag{2.2}$$

where the first term,

$$\hat{H}_A = \hbar\omega_0 \left|e\right\rangle \left\langle e\right| \tag{2.3}$$

describes a free atom's internal degrees of freedom, and the ground state energy is set to zero. The interaction Hamiltonian H_I can be described in the electric-dipole approximation:

$$\hat{H}_I = -\mathbf{d} \cdot \mathbf{E}(x, t), \tag{2.4}$$

where $\mathbf{d}$ is the dipole operator of the atom. In the dipole approximation we neglected the spatial variation of the light field across the atom, which is justified since the wavelength is large compared to the atom size, $\lambda \gg x$. The dipole operator has only off-diagonal non-zero elements, $\boldsymbol{\mu} = \left\langle e|\mathbf{d}|g\right\rangle = \left\langle g|\mathbf{d}|e\right\rangle$, so it can be written as

$$\mathbf{d} = \boldsymbol{\mu} \left(\left|e\right\rangle \left\langle g\right| + \left|g\right\rangle \left\langle e\right| \right) = \boldsymbol{\mu} \left(\sigma_+ + \sigma_- \right), \tag{2.5}$$

where we've introduced the raising and lowering operators for the two-level system, $\sigma_+ = \left|e\right\rangle \left\langle g\right|$ and $\sigma_- = \left|g\right\rangle \left\langle e\right|$. For a laser field given by Eqn. (2.1), the interaction Hamiltonian is

$$\hat{H}_I = -\frac{\hbar\Omega(x)}{2} \left[e^{-i(\omega_L t - \phi(x))} \left(\sigma_+ + \sigma_- \right) + c.c \right], \tag{2.6}$$

where we introduced the Rabi frequency $\hbar\Omega(x) = \boldsymbol{\mu} \cdot \boldsymbol{\epsilon} E_0(x)$.

If we choose a reference frame rotating with the frequency ω_0 and switch into the interaction picture, we find in the new $\hat{H}_I$ terms evolving in two different time scales. The terms oscillating at $\Delta_a \equiv \omega_L - \omega_0$ will evolve slower than the ones at $\omega_L + \omega_0$. Here we introduced the detuning Δ_a of the laser frequency form the atomic transition frequency. For detunings smaller than the optical frequencies, $\Delta_a \ll |\omega_L + \omega_0| \approx 2\omega_L$, the rapidly oscillating terms can be neglected as they average to zero. This is called the rotating-wave approximation (RWA) and is valid for near-resonant excitation and optical frequencies. In the case of far-detuned dipole traps, RWA does not hold.

To remove the explicit time dependence in $\hat{H}_I$, we switch into a frame rotating with ω_L by using a unitary transformation $U = \exp(i\omega_L t \left|e\right\rangle \left\langle e\right|)$. The new Hamiltonian becomes

$$\hat{H} = -\Delta_a \sigma_+ \sigma_- - \frac{\hbar\Omega(x)}{2} \left(\sigma_+ e^{-i\phi(x)} + \sigma_- e^{i\phi(x)} \right) \tag{2.7}$$

where the first term corresponds to the free atom Hamiltonian and the second to the interaction Hamiltonian, and we used $|e\rangle \langle e| = \sigma_+ \sigma_-$. The solution of this system satisfies the time dependent Schrödinger equation and can be expanded as a combination of eigenfunctions of the atom Hamiltonian $\hat{H}_0$:

$$|\psi\rangle = c_g |g\rangle + c_e e^{-i\omega_0 t} |e\rangle. \tag{2.8}$$

In the RWA, new coefficients are chosen so that $\widetilde{c}_g = c_g$ and $\widetilde{c}_e = c_e e^{i\omega_L t}$. Next we introduce the density matrix corresponding to this new wavefunction

$$\rho = |\psi\rangle \langle \psi| = \sum_{ij} \rho_{ij} = \sum_{ij} \widetilde{c}_i \widetilde{c}_j^*, \tag{2.9}$$

where diagonal terms correspond to the populations in each atomic state, and the off-diagonal terms to the (slowly-rotating) coherences between the states. The time evolution of the density matrix is given by the von Neumann equation

$$\frac{d\rho}{dt} = \frac{i}{\hbar}[\rho, \hat{H}], \tag{2.10}$$

To fully take into account the relaxation from the excited to ground state, the effect of spontaneous emission has to be included. To describe the process of spontaneous emission, quantization of the EM field is required. This relaxation is a consequence of the coupling of the atom to the vacuum field. The atom can spontaneously emit into different vacuum modes with different probabilities, resulting in a random and isotropic emission spectrum. Spontaneous emission can therefore be seen as a dissipation channel and phenomenologically included in the master equation. If the rate of spontaneous emission is Γ, the master equation for the evolution of the density matrix becomes

$$\frac{d\rho}{dt} = \frac{i}{\hbar}[\rho, \hat{H}] + \mathcal{L}_a\rho, \tag{2.11}$$

where $\mathcal{L}_a\rho = \Gamma\left(2\sigma_-\rho\sigma_+ - \{\sigma_+\sigma_-, \rho\}\right)$ is a Liouvillian operator describing the losses. From the master equation, time evolution of atomic populations and coherences can be calculated:

$$\dot{\rho}_{ee} = -\Gamma\rho_{ee} + \frac{i\Omega}{2}\left(\rho_{eg}e^{i\phi(x)} - \rho_{ge}e^{-i\phi(x)}\right) \tag{2.12}$$

$$\dot{\rho}_{ge} = -\left(\frac{\Gamma}{2} + i\Delta_a\right)\rho_{ge}e^{-i\phi(x)} - \frac{i\Omega}{2}\left(\rho_{ee} - \rho_{gg}\right), \tag{2.13}$$

where we've taken into account that $\rho_{ge} = \rho_{eg}^*$ and $\rho_{gg} + \rho_{ee} = 1$. These equations are called

optical Bloch equations (OBE).

It is convenient to introduce three new variables u, v and w (which are the components of the Bloch vector (u, v, w)):

$$u(t) = \mathfrak{Re}\left[\rho_{ge}(t)e^{-i\phi}\right] \tag{2.14a}$$

$$v(t) = \mathfrak{Im}\left[\rho_{ge}(t)e^{-i\phi}\right] \tag{2.14b}$$

$$w(t) = \rho_{ee} - \frac{1}{2}, \tag{2.14c}$$

so the stationary solution to OBEs (2.12-2.13) yields:

$$u_{st} = \frac{2\Omega\Delta_a}{2\Omega^2 + 4\Delta_a^2 + \Gamma^2} \tag{2.15a}$$

$$v_{st} = \frac{2\Omega\Gamma}{2\Omega^2 + 4\Delta_a^2 + \Gamma^2} \tag{2.15b}$$

$$\rho_{ee} = \frac{\Omega^2}{2\Omega^2 + 4\Delta_a^2 + \Gamma^2}. \tag{2.15c}$$

These solutions can be written in terms of the saturation parameter:

$$s = \frac{2\Omega^2/\Gamma^2}{1 + 4\Delta_a^2/\Gamma^2} = \frac{s_0}{1 + 4\Delta_a^2/\Gamma^2}, \tag{2.16}$$

with s_0 being the on-resonance saturation parameter:

$$s_0 = \frac{2\Omega^2}{\Gamma^2} = \frac{I}{I_{sat}}, \tag{2.17}$$

where I is the optical intensity of the laser beam and I_{sat} is the saturation intensity of the atomic transition. From here follows:

$$u_{st} = \frac{\Delta_a}{\Omega}\frac{s}{1+s} \tag{2.18a}$$

$$v_{st} = \frac{\Gamma}{\Omega}\frac{s}{1+s} \tag{2.18b}$$

$$\rho_{ee} = \frac{1}{2}\frac{s}{1+s}. \tag{2.18c}$$

It is instructive to note that u has a dispersive shape and is, by definition, the real part of the atomic susceptibility, while v has the absorptive Lorentzian shape and is the imaginary part of the susceptibility, as is shown in Fig. 2.1. This can be seen by looking at the induced polarization in the electric field $\mathbf{P} = \varepsilon_0\chi\mathbf{E}$, where χ is linear susceptibility of the medium. On

the other hand, polarization can be written as the expected value of the dipole moment operator $\mathbf{P} = N\langle\mathbf{d}\rangle$, with N being the concentration of atoms. Since the expected value of the operator is given by $\langle A \rangle = Tr(\rho A)$, we get $\mathbf{P} = N\boldsymbol{\mu}(\rho_{eg} + \rho_{ge})$. We can see a direct connection between susceptibility of a transition χ_{ij} and the corresponding quantum-mechanical coherence ρ_{ij}. The index of refraction n and the absorption coefficient α are connected to the real and imaginary part of the susceptibility, respectively. Hence, they can be connected to the coherence as well: $n \propto \mathfrak{Re}(\rho_{ij})$ and $\alpha \propto \mathfrak{Im}(\rho_{ij})$.
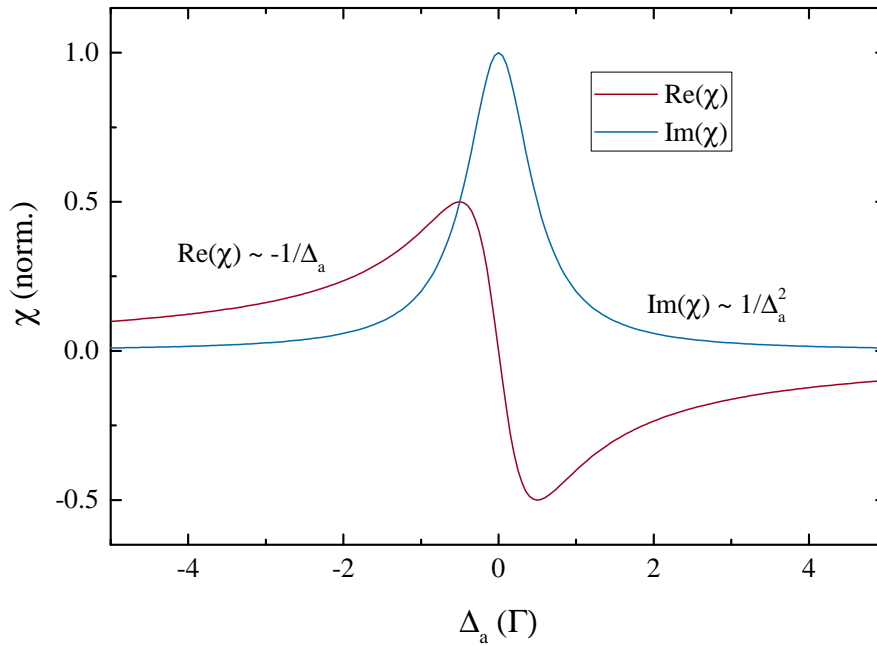
Figure 2.1: Real and imaginary values of atomic susceptibility and atomic quantum coherence near the atomic resonance. The real part corresponds to the index of refraction, has a dispersive shape and is responsible for lightshifts of atomic energy levels and for the dipole force. The imaginary part has a Lorentzian shape that corresponds to absorption and resonant scattering, and is responsible for dissipative forces that can lead to cooling or heating of atoms. Far from resonance, the dissipative term falls off faster $(1/\Delta_a^2)$ than the dispersive one $(1/\Delta_a)$, which is why far detuned lasers are used to minimize dissipative scattering and to trap the atoms in conservative potentials.

To determine the light-induced force, we use the Ehrenfest theorem and define the force as the expectation value of its operator:

$$\mathbf{F} = \langle\hat{\mathbf{F}}\rangle = \frac{i}{\hbar}\langle[\hat{H}, \hat{\mathbf{p}}]\rangle = -\langle\boldsymbol{\nabla}\hat{H}\rangle = Tr[\rho\boldsymbol{\nabla}\hat{H}] \tag{2.19}$$

Using the Hamiltonian (2.7) and Eqn. (2.18a) - (2.18c), we get

$$\mathbf{F}(x) = -\hbar \left(\boldsymbol{\nabla}\Omega(x)u_{st} + \Omega\boldsymbol{\nabla}\phi(x)v_{st} \right) \tag{2.20}$$

The first term is proportional to the gradient of the Rabi frequency, i.e. to the spatial change of the light intensity. It has a dispersive shape (due to u_{st}) and is called the dipole force. The second term is proportional to the gradient of the phase, has a Lorentzian shape (due to v_{st}) and is called the radiation pressure force.

2.1.2 Radiation pressure force

Let us first investigate the case of a plane wave, for which the phase is $\phi(x) = -kx$, where k is the wave vector. Thus,

$$\boldsymbol{\nabla}\Omega(x) = 0$$
$$\boldsymbol{\nabla}\phi(x) = -k$$

The dipole force is zero for the plane wave illumination, and for the radiation pressure force we get:

$$\mathbf{F}_{pr} = \frac{\Gamma}{2}\frac{s}{s+1}\hbar\mathbf{k}. \tag{2.21}$$

As shown in Eqn. (2.18c) the excited state population $\rho_{ee} = \frac{1}{2}\frac{s}{s+1}$ also has a Lorentzian shape on atomic detuning. The radiation pressure force can be written as $\mathbf{F}_{pr} = \Gamma_{sp}\hbar\mathbf{k}$ which can be easily understood due to momentum transfer of one recoil $\hbar k$ when a photon is absorbed, which occurs at a rate $\Gamma_{sp} = \rho_{ee}\Gamma$. The force due to absorption is in direction of the propagating beam. The force due to spontaneous emission is in random direction, so it does not contribute to the mean force, averaged over many cycles. The expression for the force can also be written as:

$$\mathbf{F}_{pr} = \frac{\hbar\mathbf{k}\Gamma}{2}\frac{s_0/2}{1+s_0+4\Delta_a^2/\Gamma^2} \tag{2.22}$$

It can be seen from this expression that for high saturation parameter, the amplitude of the force saturates to the maximum value of $F_{max} = \hbar k\Gamma/2$, as shown in Fig. 2.2(b). The wings of the Lorentzian curve saturate slower than the peak (see 2.2(a)), leading to the well known effect of power broadening, where the linewidth increases as $\Gamma' = \Gamma\sqrt{1+s_0}$.

Laser cooling and the Doppler temperature. The transfer of momentum due to radiation pressure force is the mechanism of laser cooling of atoms. For atoms in motion, Doppler effect has to be included since the atoms will see the laser frequency red- or blue-shifted depending
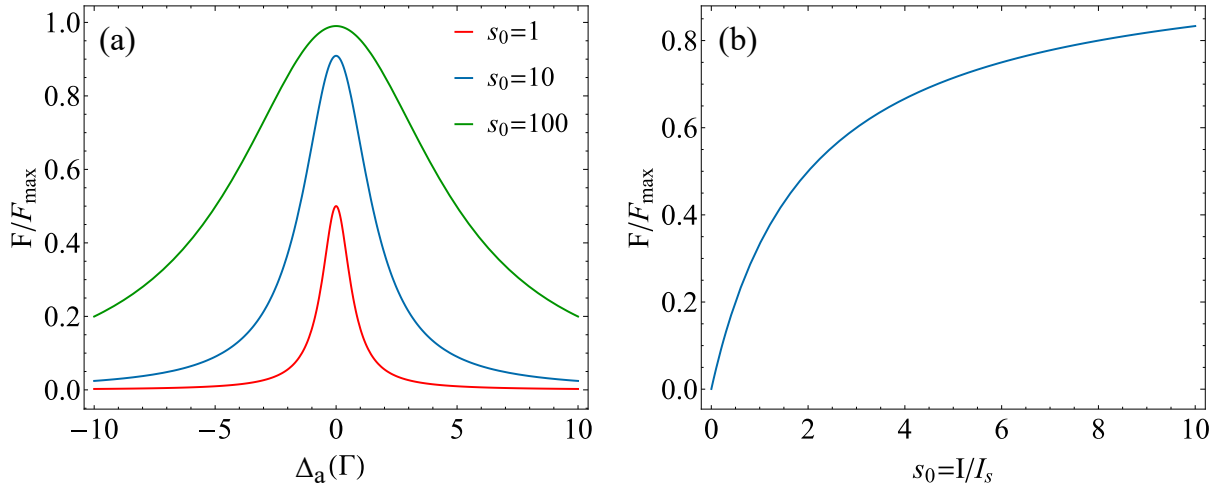
Figure 2.2: Radiation pressure force given in units of $F_{max} = \hbar k \Gamma / 2$, which is the value to which the force saturates for large intensities, $s_0 \geq 1$. (a) Dependence on detuning for three different saturation parameters. (b) Dependence on saturation parameter (i.e. intensity) for $\Delta_a = -\Gamma/2$.

on their velocity. If we tune the laser frequency slightly below the atomic transition, $\Delta_a < 0$, the atoms moving towards the beam will preferentially absorb the photons since they will be Doppler-shifted closer to the resonance. In many such cycles of preferred absorption and randomly oriented spontaneous emission, it can be shown that atoms can be slowed down, i.e. cooled. This technique is therefore called Doppler cooling.

To determine the cooling temperature limit, we need to include the heating force due to diffusion, which limits the effect of the cooling force. This limit is called the Doppler temperature and depends on the linewidth of the atomic transition:

$$k_B T_D = \frac{\hbar \Gamma}{2}, \tag{2.23}$$

It was shown however, first experimentally, then theoretically, that even sub-Doppler temperatures can be achieved if polarization gradient of light is included, combined with atomic magnetic states [31]. In these configurations, the atoms on average move up the potential more than down the potential, effectively losing energy and temperature. This kind of cooling is called Sisyphus cooling. In standard MOTs sub-Doppler temperatures are readily achieved, since circularly polarized laser beams are used to cool and trap the atoms. The interference of these counter-propagating beams creates a spatially dependent polarization, i.e. a spatially dependent optical potential.

2.1.3 Dipole force

Let us now investigate the case of a standing wave, for which the amplitude of the field and hence the Rabi frequency vary as $\Omega(x) = \Omega_0 \cos(kx)$, and the phase is constant. Thus,

$$\boldsymbol{\nabla}\Omega(x) = -k\Omega_0 \sin(kx)$$
$$\boldsymbol{\nabla}\phi(x) = 0,$$

the radiation pressure force vanishes and only the dipole force remains. Using the expression (2.18a) it can be written as:

$$\mathbf{F}_{dip} = -\hbar\Delta_a \frac{\boldsymbol{\nabla}\Omega}{\Omega} \frac{s}{1+s} = -\frac{\hbar\Delta_a}{2} \frac{\boldsymbol{\nabla}s}{1+s}. \tag{2.24}$$

It can be seen that the dipole force can be derived from the following dipole potential:

$$U_{dip}(\mathbf{r}) = \frac{\hbar\Delta_a}{2} \ln(1 + s(\mathbf{r})). \tag{2.25}$$

The dipole force is a conservative force. In the far off-resonance case, $|\Delta_a| \gg \Gamma, \Omega$, the saturation parameter is small and the logarithm can be expanded. The potential becomes:

$$U_{dip}(\mathbf{r}) = \frac{\hbar\Delta_a}{2} s(\mathbf{r}) = \frac{\hbar\Gamma^2}{8\Delta_a} \frac{I(\mathbf{r})}{I_{sat}}, \tag{2.26}$$

and is proportional to the local intensity. As mentioned, the dependence of the dipole force on detuning has a dispersive shape and is related to the real part of the atomic polarizability.

The important note is that the dipole force changes sign for positive and negative detunings. For a red detuned trap, $\Delta_a < 0$, the potential minima occur at the points of maximum intensity, while for blue traps, $\Delta_a > 0$, the potential minima occur at intensity minima. Because of this, atoms in red traps are high-field seekers and are attracted to intensity maxima, while in blue traps they are low-field seekers, attracted to the field minima.

A great review of the dipole force, dipole traps and their application can be found in [32]. Conservative optical potentials can be realized by tightly focusing a laser beam or creating a standing wave in one or more dimensions. A tightly focused Gaussan beam is usually called a dipole trap and the atoms are pulled into the center of the beam waist. The trap created by a standing wave is usually called an optical lattice. Optical lattices can be realized using both red and blue detuned light, while the single-beam traps need to be red detuned unless some higher order modes of the laser beam are used. As can be seen from Eqn. (2.26) and in Fig.

2.3, red optical lattices create wells with negative potential energy, while blue lattices create hills with positive energy. Some atoms can actually gain energy moving down the potential, since the energy of the trap is added to the whole system and can be measured as an increase in temperature of the atoms. Most experimental realizations use red-detuned traps, since they are attractive and the atoms are pulled into the laser beam from the transverse directions, so longer trapping times can be achieved.
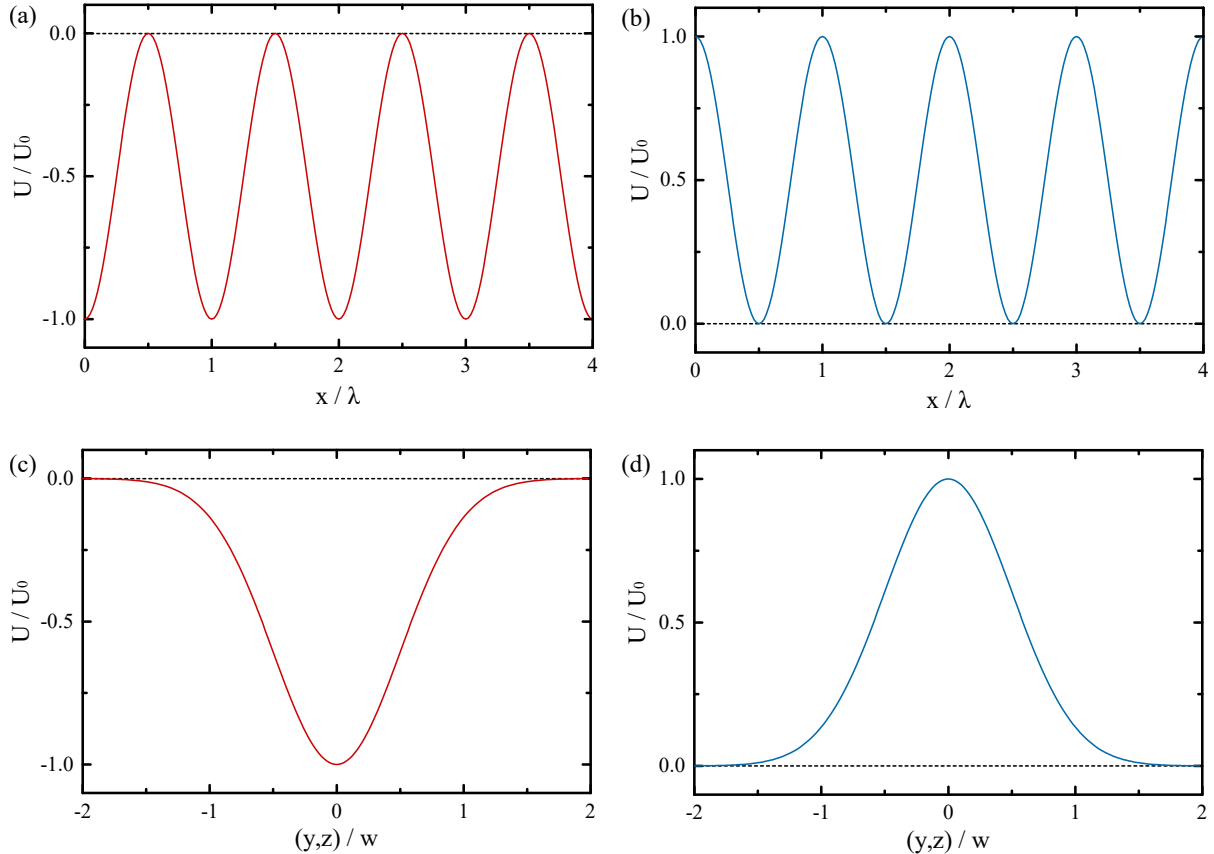
Figure 2.3: Spatial dependence of the optical lattice potential for (a) red and (b) blue detunings, and the transversal Gaussian-shaped potential due to beam waist w for (c) red and (d) blue detunings. Red-detuned potentials create wells with negative energy, while blue-detuned potentials create hills.

It should be noted that for large value of detuning, the radiation pressure force falls as $1/\Delta_a^2$, while the dipole force falls as $1/\Delta_a$. For large detunings, the conservative dipole force dominates the dynamics and resonant scattering can be neglected. In these far detuned conservative traps, the saturation parameter is very low and atoms are mostly in the ground state, as there is no resonant absorption and transfer of population. The atom can be seen as a polarizable particle with a changing index of refraction (the real part of the polarizability) due to interaction with the light field.

2.1.4 Interaction with quantized light - Jaynes-Cummings model

The discussion so far assumed the interaction of atoms with classical light, which gives accurate results for free space excitation and high photon numbers of the pump laser. However, this approach does not hold for light inside optical resonators made of high-reflectivity mirrors. In this case, photons circulate a large number of times between the mirrors before they leak out of the cavity, so back-action of intracavity atoms on cavity photons can't be neglected. Optical cavities can also operate in low photon number regime, where each individual photon matters. This field of research is called cavity quantum electrodynamics (cQED) and usually investigates single atoms interacting with single cavity photons.

The electric field of quantized light can be written similar to Eqn. (2.1)

$$\mathbf{E}(x, t) = \boldsymbol{\epsilon} E_0(x) \left(a^\dagger e^{i\omega_c t} + a e^{-i\omega_c t} \right), \tag{2.27}$$

where ω_c is the cavity photon frequency, $E_0 = \sqrt{\frac{\hbar \omega_0}{2\epsilon_0 V}}$ is the electric field corresponding to a single photon in a cavity of mode volume V, and a^+, a are photon creation and annihilation operators, respectively. For simplicity we wrote the electric field at a specific point in space, setting the additional term $\exp(i\phi(x)) = 1$. Taking into account that $a^\dagger a$ corresponds to the photon number operator, Hamiltonian for the cavity field is

$$\hat{H}_c = \hbar \omega_c a^\dagger a. \tag{2.28}$$

Using the dipole and RWA approximations, the interaction Hamiltonian with the quantized field has a similar form as Eqn. (2.7):

$$\hat{H}_i = \hbar g(x) \left[\sigma_+ a + \sigma_- a^\dagger \right], \tag{2.29}$$

where

$$g = \boldsymbol{\mu} \cdot \boldsymbol{\epsilon} \sqrt{\frac{\hbar \omega_c}{2\varepsilon_0 V}}, \tag{2.30}$$

is the single photon Rabi frequency, analogous to the Rabi frequency Ω introduced for classical light. This interaction Hamiltonian can be easily understood through processes of absorption and emission. The first term corresponds to the excitation of atom into the excited state by absorption (annihilation) of a photon, while the second term corresponds to the relaxation of atom into the ground state by emitting (creating) a photon. The RWA approximation also becomes more intuitive in this picture, because we've discarded the energy non-conserving terms $\sigma_+ a^\dagger$

and $\sigma_- a$. Switching into the interaction picture rotating with the pump laser frequency ω_L, we arrive at the Hamiltonian:

$$\hat{H}_{JC}/\hbar = -\Delta_a \sigma_+ \sigma_- - \Delta_c a^\dagger a + g(\sigma_+ a + \sigma_- a^\dagger), \qquad (2.31)$$

where we introduce the detuning of the pump laser from the cavity resonance $\Delta_c = \omega_L - \omega_c$. The expression (2.31) is called the Jaynes-Cummings Hamiltonian.

We've shown how we phenomenologically introduce the atomic relaxation rate Γ into the equations. Similarly, photons can leak through the cavity mirrors, and we denote this loss rate as κ. This incoherent photon loss can be treated the same way as photon loss due to atoms. The master equation then becomes:

$$\dot{\rho} = \frac{i}{\hbar}[\rho, \hat{H}_{JC}] + (\mathcal{L}_a + \mathcal{L}_c)\,\rho, \qquad (2.32)$$

with included cavity loss term $\mathcal{L}_c = \kappa \left(2a\rho a^\dagger - \{a^\dagger a, \rho\} \right)$.

Before going into more detail about this coupled dynamics, we first introduce some general concepts about optical cavities to better understand the advantages of optical cavity and the interaction of atoms with resonator light. We also introduce the optical frequency comb as a source of multimode phase-coherent light used to simultaneously excite a multitude of cavity modes, creating a complex intra-cavity potential.

2.2 Optical cavity

2.2.1 Spectral properties of the cavity fields

We start with the analysis of a Fabry-Perot interferometer, which consists of two parallel mirrors of high reflectivity and flat surfaces. Let us consider first the case of perfectly reflecting mirrors. Viewing the light inside the cavity as a standing wave, it is clear that only discreet wavelength values are supported in the cavity, such that the nodes (zero light intensity) of the fields are always at the mirror position. In a cavity of length L, for a standing wave of the shape $f(x) = \sin(kx)$ this condition gives $kL = q\pi$, with $q = 0, 1, 2....$ From this condition we find the frequency difference between two cavity modes, called the free spectral range (FSR):

$$\nu_{q+1} - \nu_q \equiv FSR = \frac{c}{2nL}, \qquad (2.33)$$

where n is the index of refraction of the medium inside the cavity. We could arrive to the same conclusion by treating the cavity light as a travelling photon bouncing back and forth between the mirrors. In this picture, there can be a build-up of light in the cavity only if the phase change during one round-trip, $\phi = 2kL$, equals a multiple of 2π.

If the mirrors are not perfectly reflective, the cavity modes are not perfectly sharp delta functions in frequency space, but have a finite linewidth. To describe this, we look at a Fabry-Perot cavity made of mirrors with amplitudes of reflection r_j, transmission t_j, and losses l_j. For a mirror surface j the following relation holds

$$|r_j|^2 + |t_j|^2 + |l_j|^2 = R_j + T_j + L_j = 1. \tag{2.34}$$

Let us look at the light transmitted from the cavity when we pump the input mirror with a field $E_i(t) = E_0 \exp(i2\pi\nu t)$, where E_0 is the amplitude and ν the frequency of the field, as shown in Fig. 2.4(a). The field transmitted through the first mirror, $t_1 E_i$, travels an optical path of nL inside the cavity, gets reflected from the second mirror, $r_2 t_1 E_i$, again travels nL and gets reflected from the first mirror, $r_1 r_2 t_1 E_i$. From that point the cycle continues, so during each round trip the field is multiplied by a factor $r_1 r_2 \exp(ik2nL) = r_1 r_2 \exp(i2\pi\nu/FSR)$, where we used the same definition of the free spectral range, $FSR = c/2nL$. For each cycle, a fraction t_2 of the field is transmitted out of the cavity on the second mirror. Here we assume that no light is lost in the intra-cavity medium. The transmitted field can be written as a geometric series:

$$E_t(t) = t_1 t_2 E_i \sum_m r_1^m r_2^m \exp(i2\pi m\nu/FSR) = \frac{t_1 t_2}{1 - r_1 r_2 \exp(i2\pi\nu/FSR)} E_i \tag{2.35}$$

Experimentally we measure the light intensity, and not the field, so it is more useful to look at the transmitted intensity $I_t \propto |E_t|^2$. Here we will assume a symmetric cavity with identical mirrors $(r_1, t_1, l_1) = (r_2, t_2, l_2)$ and, for simplicity, set all amplitudes to have real values. If, for example, the reflection coefficient were a complex number, $r_j = |r_j| \exp(i\phi_j)$, the phase would have to be included in Eqn (2.35), but it wouldn't bring any new understanding of the concepts. For the transmitted intensity we get

$$I_t = \frac{T^2}{(1 - R)^2 + 4R \sin^2\left(\frac{\pi\nu}{FSR}\right)} I_i \tag{2.36}$$

To determine the linewidth of the cavity mode, we look at FWHM width of I_t. The maximum intensity occurs for $\sin^2(\pi\nu/FSR) = 0$, and at FWHM points $I_t = I_{max}/2$, for which

$4R\sin^2(\pi\nu/FSR) = (1 - R)^2$. This gives:

$$\sin^2\left(\frac{\pi\nu_{FWHM}}{FSR}\right) = \left(\frac{\pi}{2\mathcal{F}}\right)^2, \tag{2.37}$$

where we introduced the cavity finesse:

$$\mathcal{F} \equiv \frac{\pi\sqrt{R}}{1 - R} = \frac{\pi\sqrt{r_1 r_2}}{1 - r_1 r_2}. \tag{2.38}$$

The FWHM frequencies are then

$$\nu_{FWHM} = \pm\frac{FSR}{\pi}\arcsin\left(\frac{\pi}{2\mathcal{F}}\right). \tag{2.39}$$

High-finesse resonators are of most importance, and are used in most ($\mathcal{F} \geq 1000$) experiments, so we can use the small angle approximation to get $f_{FWHM} \approx \pm FSR/(2\mathcal{F})$, from which follows:

$$\Delta\nu = \frac{FSR}{\mathcal{F}} \tag{2.40}$$

We emphasize here that only two quantities are needed to characterize the cavity parameters. Cavity length determines the FSR and the mirror reflectivity determines the finesse, from which the mode linewidth is calculated.

Is it useful to point out that the transmitted intensity is the part of the circulating intensity that's been coupled out through the second mirror. For a general cavity, this gives

$$I_c = I_t/t_2^2. \tag{2.41}$$

For the case of identical mirrors and real amplitudes, we get

$$I_c = \frac{T}{(1 - R)^2 + 4R\sin^2\left(\frac{\pi\nu}{FSR}\right)}I_i \tag{2.42}$$

With a similar derivation, we find the reflected intensity:

$$I_r = \frac{4R\sin^2\left(\frac{\pi\nu}{FSR}\right)}{(1 - R)^2 + 4R\sin^2\left(\frac{\pi\nu}{FSR}\right)}I_i \tag{2.43}$$

With the use of equations (2.36), (2.42) and (2.43), we can analyse the energy relations for different cavity mirror parameters, shown in Fig. 2.4 (b), (c) and (d). For a high finesse, cavity modes have a Lorentzian shape of linewidth $\Delta\nu$. We see that the buildup of the circulating intensity is strongly dependent on the finesse, which determines the number of round trips for
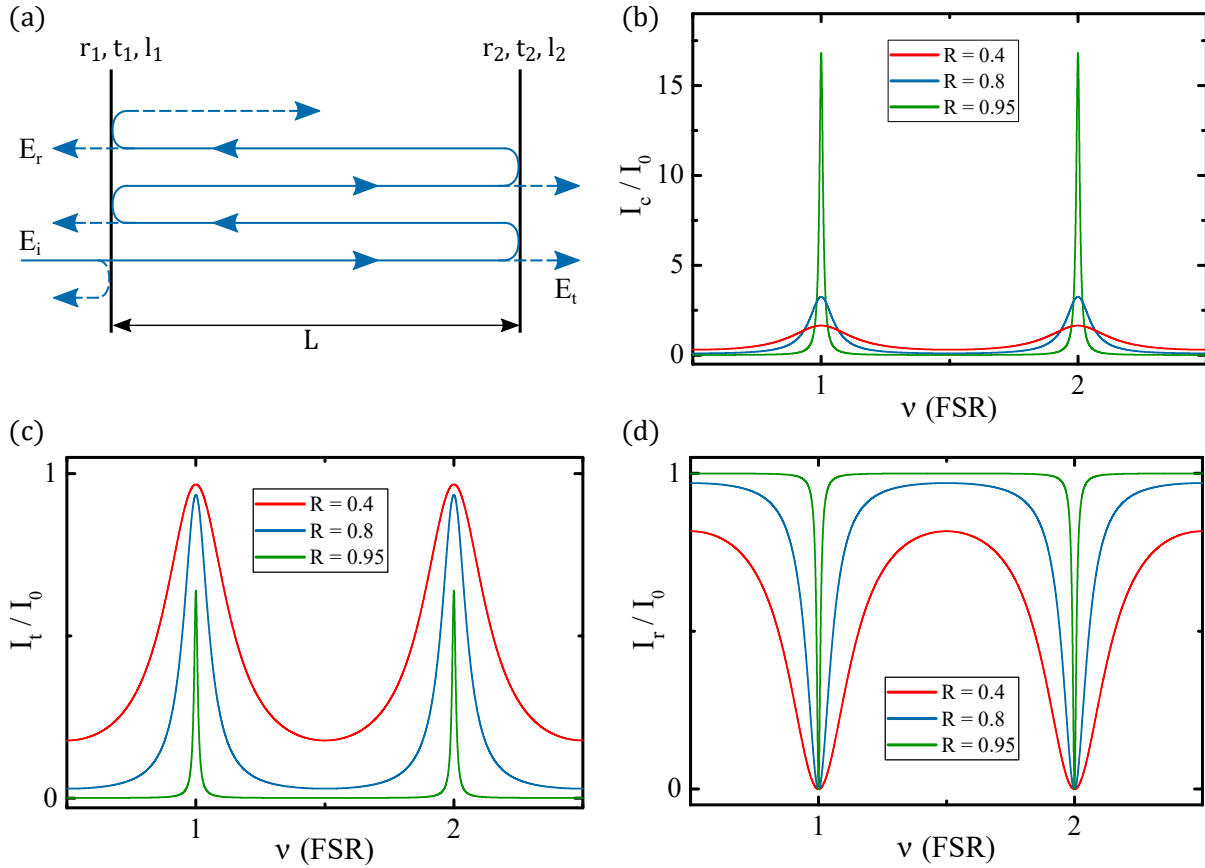
Figure 2.4: (a) A Fabry-Perot interferometer with two flat mirror surfaces. An incident electric field E_i is party coupled into the cavity, followed by many roundtrips between the mirrors. At each mirror, some light is coupled out and contributes to either transmitted field E_t or reflected field E_r due to constructive or destructive interference. (b) Circulating intensity I_c inside the cavity. Different curves show frequency dependent spectra for different mirror reflectivities and identical mirrors, calculated from Eqn. (2.42). The spectra show Lorentzian-like peaks separated by cavity FSR. The reflectivities used are $R = |r_{1,2}|^2 = (0.4, 0.8, 0.95)$ with fixed loss coefficient $L = 1\%$. The highest reflectivity gives the highest enhancement. (c) Transmitted intensity I_t calculated using Eqn. (2.36) for the listed mirror reflectivities. For high finesse, losses are comparable to transmission and the transmitted intensity is reduced. (d) Reflected intensity I_r calculated using Eqn. (2.43). It is not influenced by the losses since they occur inside the cavity when the light is coupled in. Adapted from [33].

a photon before it leaks out of the cavity. If there were no mirror losses L, transmitted intensity would equal the input intensity since the energy has to be conserved. However, for imperfect mirrors, part of the circulating intensity is lost. This becomes significant for high-finesse mirrors where the transmission coefficient becomes comparable to the loss coefficient. The photons then circulate a large number of times before being transmitted so there's a higher probability of losses due to absorption on mirrors. In Fig. 2.4(d) we see that losses do not influence the

reflected intensity, since they mostly occur inside the cavity.

Cavity ring-down time

If we abruptly turn off the input field, the transmitted intensity cannot fall instantly, but decays at the time determined by the leakage rate κ of photons out of the cavity. If we look at the change of circulating intensity in one round-trip $\Delta I_c(t) = (1 - R^2)I_c(t)$ that occurs for the round-trip time $\Delta t = 2L/c = 1/FSR$, we get a differential equation:

$$\dot{I}_c(t) = -\frac{\Delta I_c}{\Delta t} = -\left[(1 - R^2)FSR\right]I_c(t) = -\kappa I_c(t), \tag{2.44}$$

with the solution

$$I_{leak}(t) = I_0 e^{-\kappa t} = I_0 e^{-t/\tau}, \tag{2.45}$$

where we define the leakage time τ as the inverse of leakage rate, $\tau = 1/\kappa$. Using Eqn. (2.33) and (2.38), for high-finesse cavities $R \approx 1$ we get

$$\kappa = 2\pi\Delta\nu, \tag{2.46}$$

which shows that the photon decay rate from the cavity is a direct measure of the cavity mode linewidth. We note that this decay rate directly corresponds to the cavity photon loss κ introduced in the Liouvillian losses of Jaynes-Cummings Hamiltonian.

2.2.2   Cavity stability and transverse modes

The discussion so far assumed an optical cavity formed with two plane mirrors. However, these plane-parallel cavities are not practical since any relative tilt between the mirrors leads to a walk-off of the light beam. A cavity of such geometry is called unstable. To make the cavity more practical, we use spherical mirrors which provide spatial confinement to the photons as they circulate. To describe the modes of a spherical resonator, we need to include not just the longitudinal (standing wave) modes, but the transverse modes as well. An accurate description of these modes can be acquired by solving the Helmholtz equation for the electric field in the paraxial approximation. In this approximation, we assume the beam is propagating near to the optical axis of the cavity, in the z direction, so the paraxial wave equation becomes

$$\left(\mathbf{\nabla}_T^2 + 2ik\frac{\partial}{\partial z}\right)E = 0 \tag{2.47}$$

The solution of this equation are usually written in two different orthogonal sets depending on the assumed symmetry of the solution. For the case of a rectangular symmetry, the general solution can be decomposed using Hermite-Gaussian modes, while for the cylindrical symmetry Laguerre-Gaussian modes are used. These transverse modes are labelled TEM_{mn} for the case of Hermite-Gaussian modes, and TEM_{pl} for the case of Laguerre-Gaussian modes. The spatial intensity profile for different modes can be seen in Fig. 2.5. The fundamental mode TEM_{00} is called a Gaussian mode (or a Gaussian beam), and has the same shape for both Hermite- and Laguerre-Gaussian solutions. The modes for which (m, n) or $(p, l) > 0$ are called higher-order transverse modes.

Let us now focus on the stability of spherical resonators. The condition for stability can be evaluated using $ABCD$ matrices, whose treatment can be found in textbooks [30]. For a resonator of length L with mirrors of radius of curvature R_j, we define the parameter

$$g_{1,2} \equiv 1 - \frac{L}{R_{1,2}} \tag{2.48}$$

The condition of stability then becomes:

$$0 \leq g_1 g_2 \leq 1. \tag{2.49}$$

This can graphically be seen in Fig. 2.6, where the stable configurations are shaded in blue, and some typical resonator realizations are shown. Resonance frequencies for spherical resonators of different stable geometries are given by

$$\nu_{mnq} = \frac{c}{2nL} \left(q + \frac{m+n+1}{\pi} \arccos \sqrt{g_1 g_2} \right), \tag{2.50}$$

for Hermite-Gaussian modes. For the case of Laguerre-Gaussian modes, we replace $m+n$ with $2p + l$ in equation (2.50). The first term, with index q, corresponds to longitudinal modes, and the second term to higher-order modes. It can be seen that for a general cavity geometry, these modes have different frequencies. For the special case of parallel plane mirrors ($g_1 = g_2 = 1$), there are no higher-order terms and we retrieve the longitudinal modes only.

For the Gaussian beam, which is a mode of most importance, the expression for the beam waist w_0 (the smallest size of the beam, see Fig. 2.7(b)) is given by (see [28]):

$$w_0^2 = \frac{\lambda L}{\pi} \frac{\sqrt{g_1 g_2 (1 - g_1 g_2)}}{|g_1 + g_2 - 2g_1 g_2|} \tag{2.51}$$
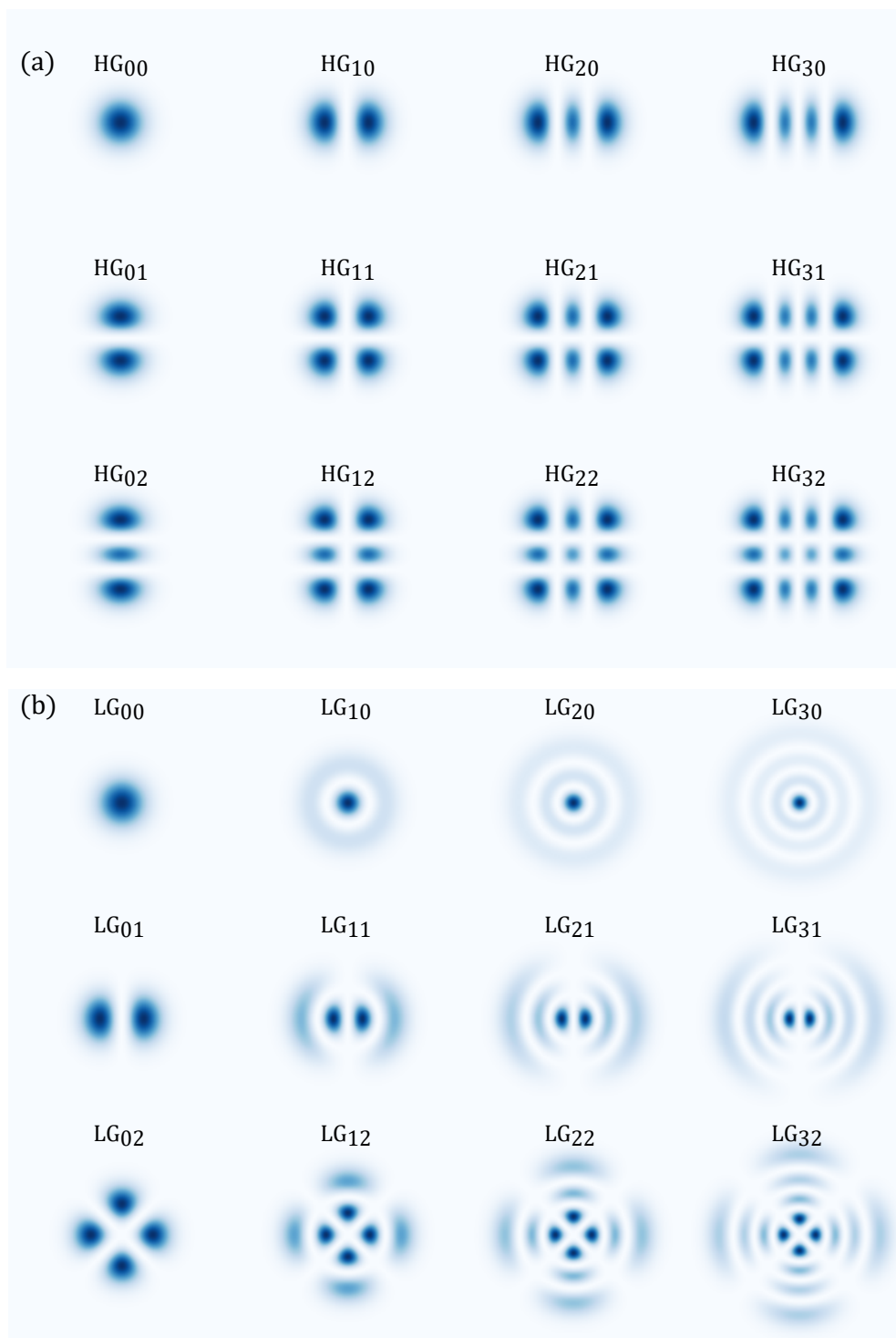
Figure 2.5: Solutions of the paraxial Helmholtz equation decomposed into two possible sets.(a) Hermite-Gaussian modes of order mn. Higher-order modes exibit rectangular symmetry. (b) Laguerre-Gaussian modes of order pl. Higher-order modes exibit cylindrical symmetry.
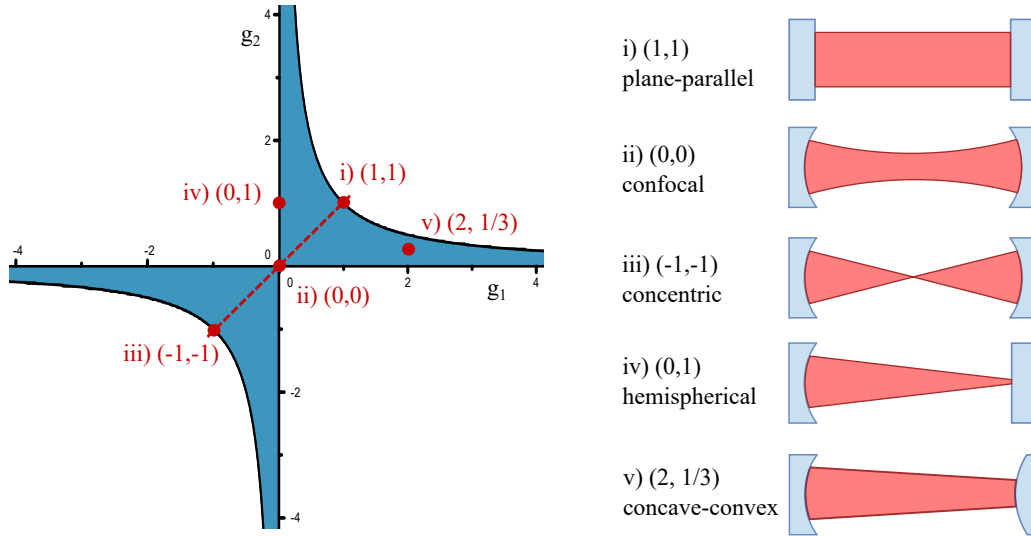
Figure 2.6: Stability diagram of optical resonators. Stable configurations are shaded in blue, according to the stability condition Eqn. (2.49). Some typical stable (g_1, g_2) configurations are also presented. Symmetric resonator geometries are located on the diagonal dashed line.

For a beam radius $w(z)$ at different positions z along the cavity axis, we have

$$w(z) = w_0\sqrt{1 + (z/z_0)^2}, \tag{2.52}$$

where we introduced the Rayleigh length $z_0 = \pi w_0^2/\lambda$. For the radius of curvature of the beam wavefront we have:

$$R(z) = z + \frac{z_0^2}{z}. \tag{2.53}$$

We note here that the curvature of the beam on the position of mirrors is equal to the radius of curvature of the mirrors.

Geometry of most importance is the confocal resonator ($g_1 = g_2 = 0$) because of its stability. This can be seen in Fig. 2.7(a) where the input rays are shown to retrace itself after two round trips regardless of tilt and displacement. As is shown in Fig. 2.7(b), the area of the beam on the mirrors is just twice the area of the waist. This is a slowly diverging beam compared to other cavity geometries, which is useful for mode-matching of the input laser beam to the Gaussian mode of the cavity. Applying equation (2.50) to confocal geometry, we see that higher-order modes are degenerate. As shown in Fig. 2.7(c), these frequencies are grouped around the TEM_{00} modes or halfway between them (called half-axial modes), depending if $m + n$ is even or odd.

Because of this mode spacing of the confocal geometry, examples in literature can be found stating that the FSR of a confocal resonator is $c/4L$, which is in line with Fig. 2.7(a) where
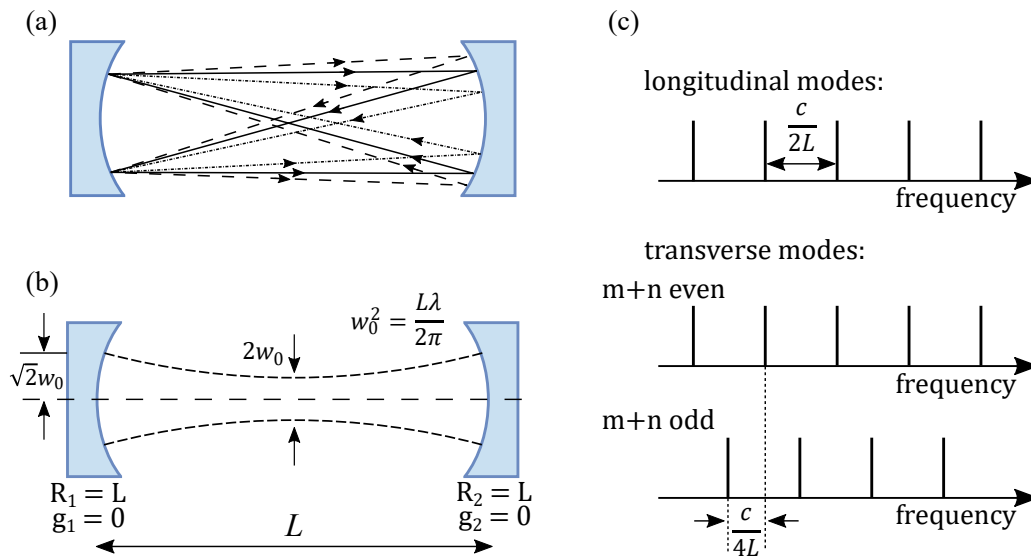
Figure 2.7: Geometry of confocal cavity. (a) Regardless of input position and tilt, rays retrace themselves after two round trips. (b) The Gaussian mode of a confocal cavity is slowly diverging, so the beam area on the mirrors is just twice the area at the mode waist w_0. (c) Frequency spectrum of a confocal cavity. Longitudinal modes are spaced by FSR, and higher modes are degenerate and fall within longitudinal modes or halfway between them, depending on the sum of higher order modes $m + n$.

the beam travels twice the cavity length to retrace itself. However, as will be shown in the following paragraph, these half-axial modes are due to mismatches in displacement or tilt of the input beam compared to the cavity axis, which couples the input light into different higher-order cavity modes, effectively doubling the cavity length. To couple only the fundamental mode, input light along the cavity axis is required. In this case, the beam only does one round-trip, and the fundamental FSR of $c/2L$ is restored.

2.2.3   Alignment of the optical cavities

The aforementioned discussion is treated with more detail in a paper by D. Anderson [34]. Here we present the important result, shown in Fig. 2.8. There are four possible ways to mismatch the input light compared to the cavity mode - displacement and tilt compared to the cavity axis (Fig. 2.8(a) and (b)), and mismatch of the input beam waist size and position compared to the cavity mode waist (Fig. 2.8(c) and (d)). It can be shown that even if the input light has a pure Gaussian mode, the beam will couple into higher-order modes due to these mismatches. Mismatch in axis displacement or tilt leads to coupling into Hermite-Gaussian modes, while mismatch in waist size and position leads to coupling into Laguerre-Gaussian modes. This can be easily understood - we break the cylindrical symmetry of the system by coupling the beam
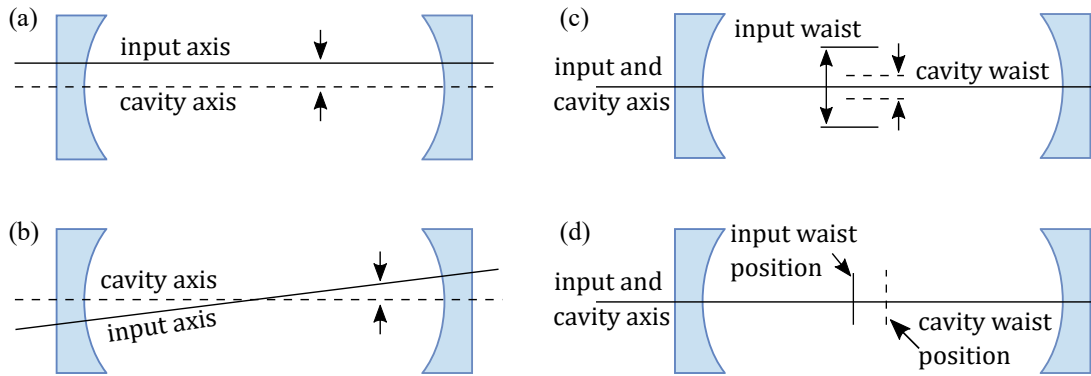
Figure 2.8: Mismatches in aligning the input beam to the cavity mode. (a) Displacement of the input beam from the optical axis. (b) Tilt of the input beam propagation compared to the optical axis. (c) Mismatch of the input beam waist size compared to the cavity mode waist. (d) Mismatch in position of input beam and cavity mode waists. Adapted from [34]

off-axis, so the coupled modes can only have a rectangular shape. If the beam is aligned with the cavity axis, the cylindrical symmetry is preserved and the higher-order modes are induced due to waist mismatch. This is experimentally and practically a very useful result. If during the alignment process we monitor the cavity transmission on a camera, we can see what higher-order modes we're coupling into. If we see rectangular modes, we can improve the alignment by walking the input beam to better match the cavity axis. If only cylindrical modes remain, we need to better match the beam waist to the cavity waist. This is done by using a lens or a set of lenses on the input beam to shape it like the supported Gaussian mode of the cavity as much as possible. For that, the use of equations (2.51)-(2.53) is needed to calculate the cavity waist and radius of curvature. This is another advantage of the confocal geometry - since the beam is slowly diverging and the waist isn't focused too tightly, the mode matching can be simply done using just a single lens.

2.3 Optical frequency combs and coupling with the cavity

2.3.1 Mode-locking

In contrast to the cw lasers that contain only a single frequency in their spectrum, pulsed femtosecond lasers consist of a large number of phase-coherent modes. Like a standard optical resonator, the resonator of the femtosecond laser supports a large number of modes. Generation of ultrashort pulses in a femtosecond range in a laser resonator is based on mode-locking, which assumes a constant phase difference between neighbouring resonator modes, $\phi_m = \phi_0 + m\alpha$,

where the index m denotes the m-th longitudinal cavity mode. The number of cavity modes that can be excited simultaneously depends on the spectral width of a gain medium in the laser, as seen in Fig. 2.9. Frequency of the m-th mode can be written as $\omega_m = \omega_c + 2\pi m f_{rep}$, where ω_c is the central frequency of the laser gain spectrum, and f_{rep} is the distance between the modes. It is the same as FSR introduced in the last chapter, but in the case of pulsed lasers, this quantity is called the repetition frequency. If M cavity modes can be excited within the gain spectrum,
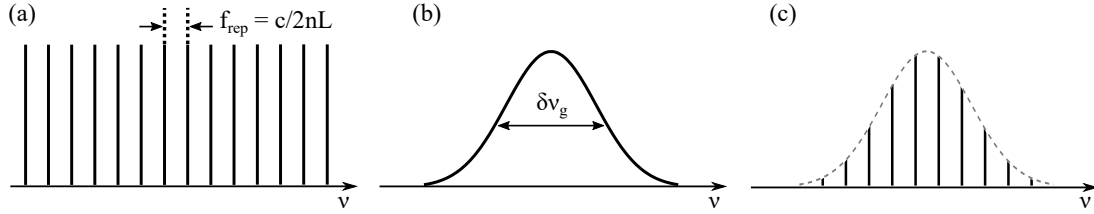
Figure 2.9: a) Longitudinal modes of a laser cavity. b) Emission spectrum of a laser gain medium. c) The number of cavity modes that can be simultaneously excited is determined by the spectral width of the gain medium and the repetition rate.

we can write the total electric field at a specific point in space as:

$$E(t) = \sum_m E_0 e^{i(\omega_m t + \phi_m)} = E_0 e^{i(\omega_c t + \phi_0)} \sum_{-(M-1)/2}^{(M-1)/2} e^{i(2m\pi f_{rep}t + m\alpha)}, \qquad (2.54)$$

where we assumed the same amplitude for each mode. For simplicity, we set $\alpha = 0$ since it is only an additional constant phase. Using the geometric series relation for this sum, we get:

$$E(t) = E_0 \frac{\sin(M\pi f_{rep}t)}{\sin(\pi f_{rep}t)} e^{i(\omega_c t)} \qquad (2.55)$$

For a large number of oscillating modes, this equation gives a train of short pulses separated in time by $T_{rep} = 1/f_{rep}$, called the repetition time. The duration of each pulse τ_p is given with the number of excited modes $\tau_p = 1/(Mf_{rep})$. This is in line with the Heisenberg principle that a short pulse in time domain has a wide spectrum in the frequency domain. The number of excited modes is approximately equal to the ratio of gain profile width $\delta\nu_g$ and the mode distance, $M \approx \delta\nu_g/f_{rep}$. The pulse duration can then be written as $\tau_p \approx 1/\delta\nu_g$. Laser mediums of a wide gain profile are therefore required for the realization of ultrashort pulses.

    The basis of mode-locking is assuming a constant phase difference between neighbouring modes, which creates a train of phase-coherent ultrashort pulses in the time domain. In practice, mode-locking can be achieved using active or passive techniques. While active techniques use some externally controlled active element, like an AOM, passive techniques rely on mechanisms

such as saturable absorption, Kerr lensing or polarization rotation [30, 35].
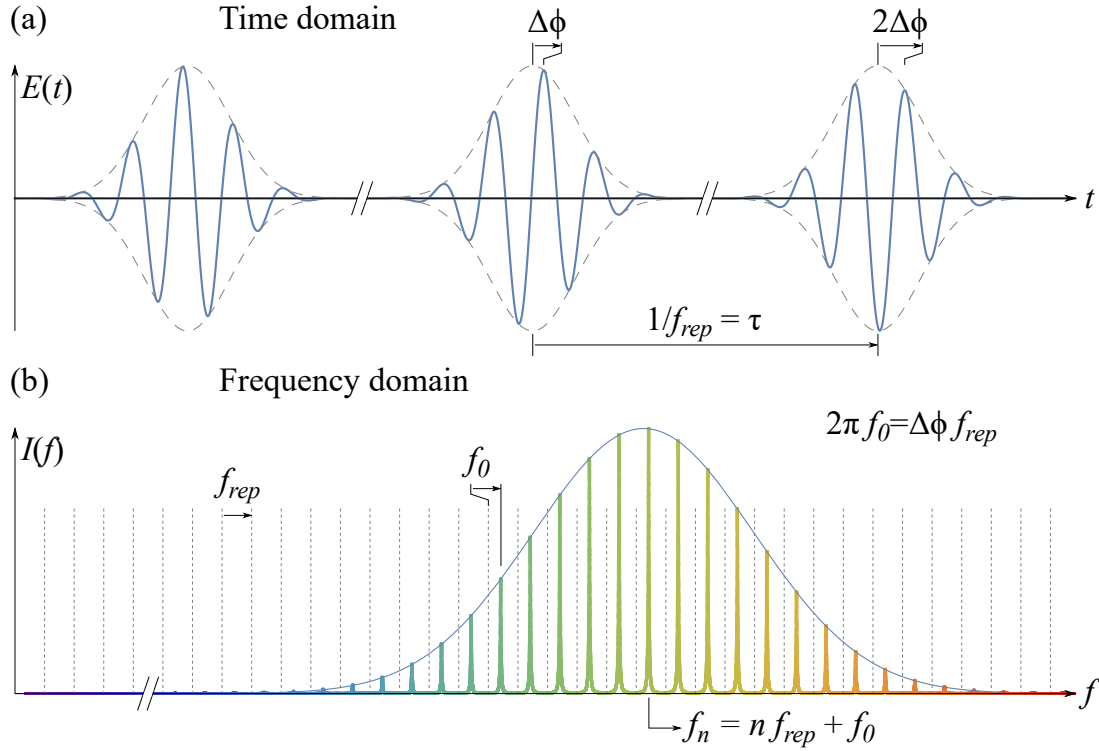
Figure 2.10: a) Time domain of a mode-locked laser consists of a train of ultrashort phase-coherent pulses separated by τ. The phase between the carrier (solid blue line) and the envelope (dashed gray line) changes from pulse to pulse by a fixed quantity, $\Delta\phi$. b) In the frequency domain a mode-locked laser generates a frequency comb of equidistant narrow modes separated by $f_{rep} = 1/\tau$. The relationship of the phase term $\Delta\phi$ and frequency f_0 is indicated. Taken with permission from [4].

The connection between time and frequency domain of a femtosecond laser is shown in Fig. 2.10. The spectrum of a femtosecond laser consists of a large number of sharp spectal lines, which is why it's called a frequency comb (FC). The n-th mode of the FC can be written as:

$$f_n = nf_{rep} + f_0, \tag{2.56}$$

where f_0 is the offset frequency. The important feature of the FC is that f_n are in optical frequency range, while f_{rep} and f_0 in radio (rf) range, connected with a large mode number $n \sim 10^6$. This feature enabled a great progress in metrology and measurements of optical frequencies, since most electronic counters can measure these rf frequencies with high precision and the stability can be transferred into the optical domain.

2.3.2 Comb-cavity coupling

Frequency combs have the same spectral structure as optical cavities, so it is natural to look at the coupling of FCs light to external cavities. The former discussion about mode-matching and beam shaping still holds for the FC beam as well, however to couple more than a few FC modes into the cavity, it is necessary to tune f_{rep} and f_0 so that FC modes match with the cavity modes. This is shown in Fig. 2.11, where the matching condition is presented both in frequency (2.11(a)) and time (2.11(b)) domain. If every comb mode is matched to the cavity, this situation
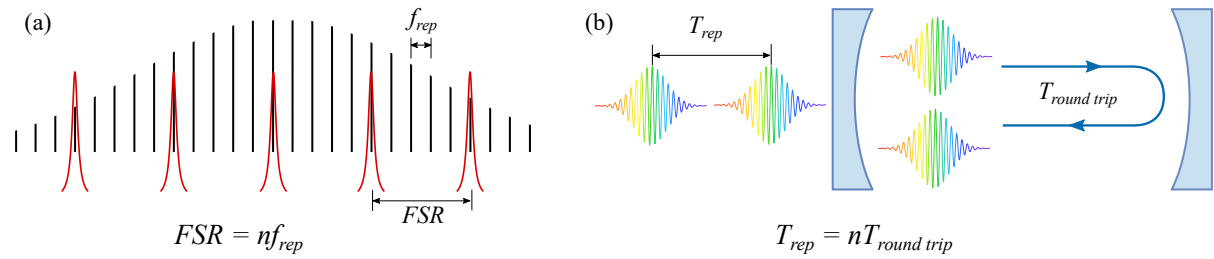
Figure 2.11: Matching the FC modes to the cavity modes. (a) In frequency domain, every n-th comb mode is matched with a cavity mode, so that frequency is coupled into the cavity. Other FC modes are reflected. (b) In time domain, a pulse circulating inside the cavity makes n round-trips before a new FC pulse enters the cavity.

is known as comb-cavity coupling. If every n-th comb mode is matched, it is known as comb filtering, which effectively decreases the coupled power, but increases the repetition frequency of the coupled light to match the cavity FSR. The FC-cavity coupling efficiency can be seen in Fig. 2.12 as we scan the FSR (this corresponds to experimentally scanning the cavity length). The coupling occurs when cavity modes in the optical domain shift by a value of f_{rep}, since then the m-th cavity mode matches the next FC mode. There is an optimal cavity mode spacing, labelled FSR_0 for which there is a perfect coupling with the FC modes - for each cavity mode there is a resonant FC mode, i.e. the FC and cavity modes have the same central frequency. As we increase (or decrease) FSR, coupling occurs with f_{rep} spacing, but it becomes less and less efficient. This can be seen on the right picture in Fig. 2.12, where cavity transmission (i.e. coupling efficiency) is shown as we scan the FSR. For even larger mismatch, the transmission amplitude falls and broadens, since more and more FC modes sit in the wings of cavity modes as we scan over them. The influence of f_0 can easily be seen from the same figure, since it would shift the whole FC spectrum, increasing or decreasing the coupling as the FC modes are shifted across the cavity modes.

To use as much available FC power as possible, it is necessary to match the FC to the cavity modes over the whole spectral range, for which the cavity dispersion has to be taken into
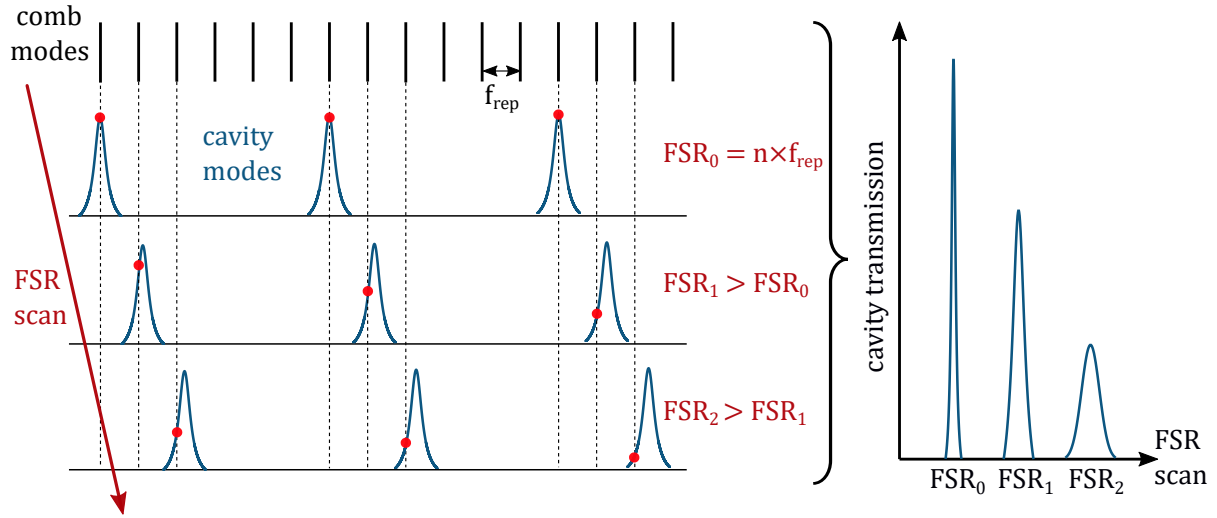
Figure 2.12: Efficient matching of FC modes with the cavity modes. For FSR_0 the matching is optimal and the cavity transmission is the highest. For other FSR values, coupling efficiency falls and the transmission signal is broadened since more FC modes sit in the wings of the cavity modes as we scan over them. Coupling occurs every time the cavity modes in the optical domain shift by f_{rep}, since then the m-th cavity mode matches the next FC mode.

account. The intracavity dispersion leads to a frequency-dependent phase shift $\phi(\omega)$, which makes the FSR frequency-dependent[36] :

$$FSR(\omega) = \frac{c}{2L + c\frac{\partial\phi}{\partial\omega}|_{\omega_0}}. \tag{2.57}$$

The dispersion term $\partial\phi/\partial\omega$ causes the cavity modes to walk-off from the FC modes as we move away from the center frequency ω_0. Dispersion thus limits the spectral bandwidth that can simultaneously be coupled into the cavity. For practical applications where coupling of a wide bandwidth is needed, low-dispersion mirrors are necessary.

The technique of coupling an FC into a cavity is the standard technique of a research field called cavity-enhanced frequency comb spectroscopy (CE-FCS) [36]. For these experiments, comb-cavity coupling is used to probe the molecular transitions of different samples inside the cavity. Due to high number of cavity round-trips, the light-matter interaction length effectively increases, and absorption of molecular samples is strongly enhanced. This method is used for detection of weak traces in various hot and room-temperature samples. On the other hand, coupling the FC with the cavity to probe cold atomic samples has not yet been reported in literature, and is the focus of our experiment, opening a way towards cavity QED experiments with multimode phase-coherent excitation.

2.4 Cavity-enhanced cooling and trapping

2.4.1 Single atoms in cavities

We now turn to the exciting features predicted in systems where atoms are inside an optical resonator and coupled to the intracavity light, while simultaneously excited with an external laser pump. We note here that the pump can be used to excite the cavity modes directly through the cavity mirrors, or by transversally interacting with the atoms, which then scatter light into the cavity modes. Hamiltonian of the external pump can therefore be written as:

$$H_{pump}/\hbar = i\eta(a^\dagger - a) + i\Omega h(\mathbf{r})\left(\sigma_+ - \sigma_-\right), \tag{2.58}$$

where the first term corresponds to longitudinal driving of the cavity modes, and the second to transversal excitation of atomic operators. Here, η is the amplitude of driving light, Ω is the Rabi frequency, and $h(\mathbf{r})$ is a spatial mode function of the transverse pump. In most cases we pump the atoms in a standing wave, thus $h(\mathbf{r}) = \cos(\mathbf{k} \cdot \mathbf{r}_\perp)$.

The theoretical results presented here were developed by the group of professor Helmut Ritsch [6] and we summarize the important results in this chapter. In the limit when atomic saturation effects are negligible, the atoms can be considered as linearly polarizable particles. This is true for large pump detunings Δ_a from the atomic resonance. A semiclassical approach can be taken in the dispersive limit, resulting in stochastic differential equations corresponding to atomic motion and cavity field. For a single atom moving in x direction along the axis of a driven cavity with a mode function $f(x) = \cos(kx)$, we get:

$$\dot{x} = \frac{p}{m} \tag{2.59a}$$

$$\dot{p} = -\hbar U_0 |\alpha|^2 \frac{\partial}{\partial x} f^2(x) \tag{2.59b}$$

$$\dot{\alpha} = \eta - i\left[U_0 f^2(x) - \Delta_c\right]\alpha - \left[\kappa + \Gamma_0 f^2(x)\right]\alpha, \tag{2.59c}$$

where we have introduced the dispersive, U_0, and dissipative, Γ_0, effects due to atom-cavity

interaction:

$$U_0 = \frac{g^2 \Delta_a}{\Delta_a^2 + \Gamma^2} \tag{2.60a}$$

$$\Gamma_0 = \frac{g^2 \Gamma}{\Delta_a^2 + \Gamma^2}, \tag{2.60b}$$

where g is the single photon Rabi frequency introduced in the first chapter, and Γ is the decay rate of the atomic excited state population. It is instructive to analyse this coupled atom-light interaction more closely. The cavity field gives rise to an optical potential U_0 felt by the atom, inducing a Stark shift in atomic energy levels. Due to $f(x)$, this potential is space-dependent as the atom travels through the cavity and is responsible for the force acting on the atoms, Eqn. (2.59b). This force is also proportional to the number of photons in the cavity, $|\alpha|^2$. On the other hand, the presence of an atom (a dispersive medium) induces a lightshift of the cavity mode frequency, shifting it by U_0. This lightshift can be seen in the first parenthesis of Eqn. (2.59c), and is also space dependent due to $f(x)$. The second parenthesis in this equation corresponds to losses of photons due to leakage through the mirrors with rate κ and due to free-space scattering with rate Γ_0 which effectively broadens the cavity resonance. The first term in Eqn. (2.59c) corresponds to the cavity mode pumping strength. In the dispersive regime of large atomic detunings, the free-space scattering can be neglected. Nevertheless, it is important to note that the presence of dispersive media in the cavity both shifts and broadens the cavity resonance.

Cavity cooling in the time picture   Let us look at the mechanism of cavity cooling in an example where the laser pump is tuned below the atomic resonance, $\Delta_a < 0$. From Eqn. (2.60a) it follows that the lightshift is also negative $U_0 < 0$, i.e. the cavity resonance is redshifted due to interaction. Let us assume the pump laser is also below a bare cavity resonance, $\Delta_c < 0$, so that only a few photons can couple into the empty cavity. When the atom is at the antinode of the cavity field, the cavity mode will be redshifted toward the pump frequency due to atom-light interaction, and more light will couple into the cavity. This positive feedback will cause a matching of cavity and pump frequencies and induce a buildup of intracavity intensity. For $\Delta_a < 0$ the miminum of the optical potential corresponds to the maximum light intensity, i.e. the atoms are high-field seekers. Lightshift and cavity buildup begin when the atom is at the intensity maxima, which is the potential miminum. However, since almost no light was coupled into the cavity at that point, the potential was very shallow. The atom now starts moving up the potential slope while the cavity builds up light. It is important to note that cavity cannot

fill instantaneously, but does it with the rate κ. This means that the light keeps building up and the potential becomes deeper *while* the atom is climbing up that potential, so the atom is losing energy. At the potential hill (intensity minimum), there is no atom-light coupling and the cavity resonance shifts back to its bare value. This causes the leakage of light out of the cavity, again at rate κ. During this time, the atom moves down the potential hill, however the potential is getting shallower. This means that the atom is on average losing more energy moving up the higher potential than going down the shallow potential. If the intracavity intensity could adjust instantaneously to atomic motion, no cooling would occur. However, due to finite cavity response time κ, the cavity loss is a dissipation channel responsible for cooling of the atom. Turning the pump frequency to the blue of the cavity, $\Delta_c > 0$, would lead to atom heating. However, for positive atomic detuning and lightshift, $\Delta_a, U_0 > 0$ and positive cavity detuning $\Delta_c \geq 0$ cooling can again be obtained with the similar explanation.

It should be noted that this example assumed a significant lightshift due to single atom in the cavity. If a lightshift is less than the cavity linewidth, no significant modification occurs, and this coupled dynamics can be investigated as a perturbation. To quantify the strength of the coupling, we introduce a dimensionless cooperativity parameter describing the ratio between atom-cavity coupling and losses:

$$\mathcal{C} = \frac{4g^2}{\kappa\Gamma}. \tag{2.61}$$

We call $\mathcal{C} \geq 1$ a strong coupling regime, and $\mathcal{C} < 1$ a weak coupling regime. For the case of strong coupling, even a single atom significantly modifies the cavity landscape. The single atom physics becomes important, so the strong coupling regime is of most interest for cavity QED. However, practical realization of strong coupling is not easy, since it requires cavities of micrometer length to achieve small mode volume and large single photon Rabi frequency, as well as high-finesse mirrors to decrease the losses as much as possible. As we will show, strong coupling can be achieved by coupling an ensemble of atoms to the same cavity mode, leading to a collective coupling strength scaling with the number of atoms.

Cavity cooling in the frequency picture   Let us now look at the cavity cooling from a different perspective. For this, it is instructive to look at the second geometry we mentioned - the transversal pumping of the atoms. Similar stochastic equations as (2.59) also hold for this case. However, a different mode pumping amplitude has to be included, since the cavity mode isn't being pumped directly, but indirectly through scattering of atoms into the cavity mode. It can be shown that the effective driving amplitude is $\eta_{eff} = g\Omega\Delta_a/(\Delta_a^2 + \Gamma^2)$, where Ω is the Rabi frequency.

Instead of looking at the atoms moving up and down potential, we focus on the frequency of

the scattered photons. This approach was developed in [37, 38] and works well in the regime of weak atom-photon coupling, as pointed out in [6]. The idea is based on the Purcell effect, where atoms inside the cavity have an enhanced (suppressed) spontaneous emission rate depending on whether the cavity mode frequency was near (far from) the atomic transition frequency. Spontaneous emission is a consequence of atom coupling to the multitude of vacuum modes; however inside the cavity these modes are not continuous, but have discrete frequencies. Therefore, if the cavity frequency doesn't match the transition frequency, spontaneous emission is suppressed. Similarly, if we transversally pump the atoms with a laser red-detuned from the cavity resonance, the atoms can scatter lower and higher frequency photons due to their motion and the Doppler effect. However, the cavity will enhance the scattering of higher frequency photons since they are closer to the cavity resonance. The up-shift of photon energy comes at the cost of atomic velocity, hence the atoms are cooled.

As presented in [6], a contour plot of cooling and heating regimes can be calculated from Eqn. 2.59, and is presented in Fig. 2.13(a) for the case of weak coupling, and in Fig. 2.13(b) for strong coupling.
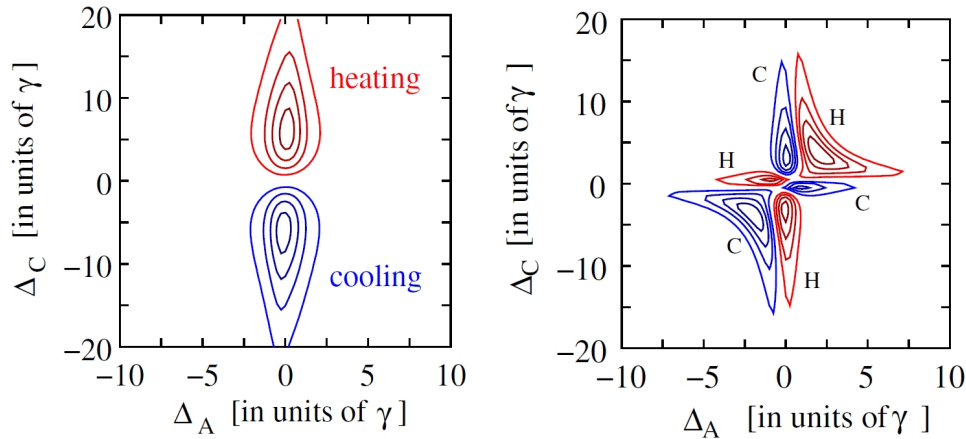
Figure 2.13: Cooling and heating regions as a function of detunings from the atomic and cavity resonances for (a) weak coupling and (b) strong coupling regime. Taken from [6].

Temperature limit   It is important to know the efficiency of cavity cooling and the lowest achievable temperature with this technique. Following the analysis presented in [6] which takes into account heating due to diffusion, we arrive at the value for the temperature limit:

$$k_B T \approx \hbar \kappa, \tag{2.62}$$

which does not depend on the atomic properties, but only the cavity linewidth. For high finesse cavities, this temperature can be much lower than the free-space Doppler limit. However, it should be noted that for atoms to be cooled in the cavity potential, they have to be slow enough to be influenced by it. It can be shown that for the atoms to be cooled in the cavity potential, their velocity needs to be less than $kv < \kappa$. Hence, there is a trade-off when choosing the cavity finesse. High-finesse cavities will be able to cool the atoms to lower temperature, but at the cost of the number of atoms in a thermal cloud that can be cooled. This means that pre-cooling of atoms in a standard MOT is needed for them to be influenced by the cavity. Even though the cavity cooling technique is insensitive to the internal structure of the particles, its practical use is still limited to the samples that can be pre-cooled by other techniques.

2.4.2 Atomic ensembles in cavities

The analysis so far assumed a single atom inside the cavity. Interestingly, adding more atoms does not just scale the same physical principles on a bigger scale, but also introduces new phenomena. The effects observed in atom-cavity interaction are therefore collective effects as they depend on the number of atoms. Formally, the Jaynes-Cummings Hamiltonian can easily be extended to N atoms at different positions:

$$H/\hbar = -\sum_j \Delta_a \sigma_{j+}\sigma_{j-} - \Delta_c a^\dagger a + \sum_j g f(\mathbf{r}_j)(\sigma_{j+}a + \sigma_{j-}a^\dagger). \tag{2.63}$$

In the case of cavity pumping, it can be shown that the atoms collectively couple to the cavity mode with an effective strength $g_{eff} = g\sqrt{\sum_j f^2(\mathbf{r}_j)} \leq g\sqrt{N}$. This means that the collective cooperativity $\mathcal{C} = 4g_{eff}^2/(\kappa\Gamma)$ is N times stronger than for a single atom.

It was shown in [39] that cavity cooling scales unfavourably with the number of atoms for longitudinal pumping. Since the collectively induced lightshift can be large, it is necessary to detune the pump further away from the cavity resonance to cool the ensemble. However, the theory shows that the cooling time increases linearly with the number of atoms, making it impractical for realization with large ensembles. Due to this theoretical prediction, only a few experiments tested the longitudinal pumping scheme [40, 41]. In [40] optomechanical cooling of a deeply trapped atoms in Lamb-Dicke regime was shown, where the center-of-mass optomechanical cooling was demonstrated by monitoring the cavity transmission. In [41] only the cavity-induced trapping of a MOT cloud was demonstrated by monitoring the cavity transmission. To the best of our knowledge, no investigation of spatial distribution of atoms in a MOT in a longitudinal pumping geometry has been reported so far. In this thesis, we investigate the

influence of the longitudinally pumped cw cavity potential on the spatial and momentum distribution of atoms by imaging the MOT cloud during a time of flight. The theoretical predictions were made for up to 100s of atoms which is far below usual atom numbers in standard MOTs, which means that some collective effects could not be taken into account. The cooling possibilities of the longitudinal geometry are therefore still not fully understood and different techniques could be used to analyse the cloud-cavity interaction.

A surprising new phenomenon occurs when we pump the atoms transversally instead of longitudinally. Now, the atoms primarily interact with the pump standing wave and scatter photons into free space and cavity modes. It is shown [42] that above a critical pump intensity, a phase transition occurs. At first, the atoms are distributed isotropically and scatter into random direction. Above threshold, the intracavity intensity induces back action onto the atomic motion, pushing them towards lattice positions in which scattering into the cavity increases. This positive feedback forces the atoms to spontaneously organize into regular spatial patterns in which scattering into the cavity is maximized compared to the free space scattering. This phase transition is presented in Fig. 2.14 and it can be seen that the atoms occupy every second lattice site. To quantify this self-organization, we introduce the order parameter:

$$\Theta = \frac{1}{N} \sum_j \sin(kx_j). \tag{2.64}$$

For an isotropic phase, $\Theta \approx 0$, and for a fully self-organized phase $\Theta = \pm 1$. The sign of the order parameter determines if the atoms localized into odd or even lattice sites. Which of the sites the atoms occupy is determined by the fluctuations around the phase transition, i.e. the sign of the order parameter is randomly determined. Self-organization has experimentally been demonstrated for a MOT cloud [9] and a BEC [10].

Scattering into the cavity modes therefore cools the atoms, and the subsequent self-organization traps them in checkerboard potential minima. Another important result is that cooling efficiency increases with the transversal pump intensity, but only below the self-organization threshold intensity. Above the threshold, the atoms become localized in the trap and the cooling efficiency drops, making it impractical on a larger scale. For optimal cooling, it would therefore be useful to increase the value of the threshold intensity, for which we introduce the frequency comb into the atom-cavity dynamics.
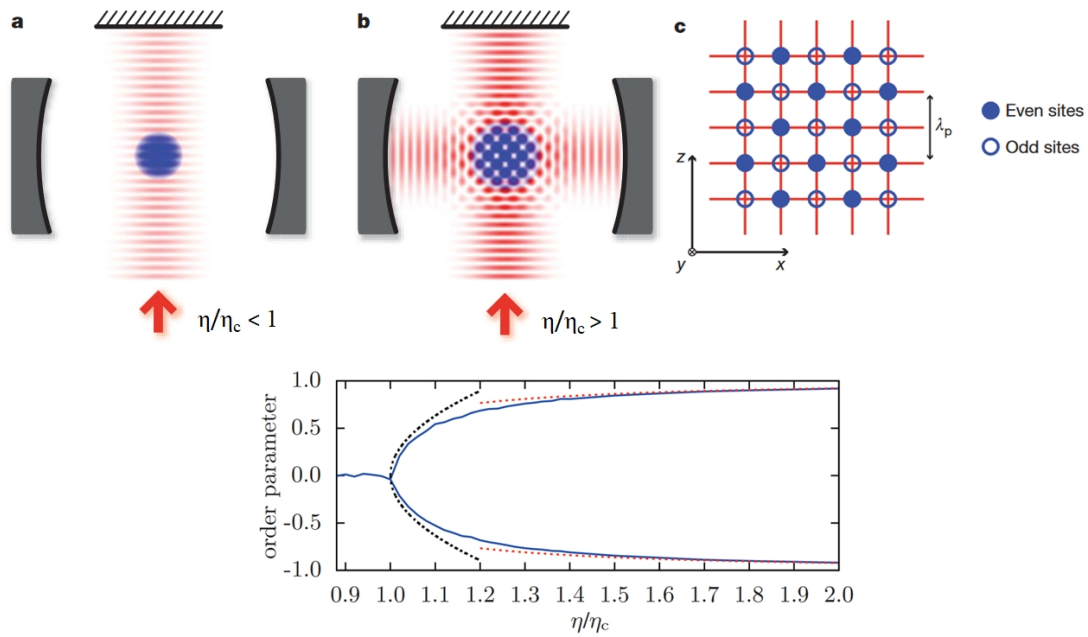
Figure 2.14: Phase transition from the isotropic phase(a) to the self-organized phase (b) when an atomic cloud is transversally pumped above the threshold intensity, $\eta > \eta_c$. Back action of intracavity intensity pushes the atoms into a checkerboard pattern (c) which maximized scattering into the cavity mode. In the isotropic phase, the order parameter $\Theta \approx 0$, while in the organized phase $\Theta \to \pm 1$. Taken from [43].

2.4.3 Cavity cooling with a frequency comb

We have already mentioned that by using an FC we can couple a multitude of phase-coherent modes simultaneously into the cavity. This creates an optical potential that is more complex than a single standing wave. In fact, a pulse is created and is circling inside the cavity, with the repetition rate of the pulses equal to the cavity FSR.

The dynamics of atoms in a cavity transversally pumped by an FC was theoretically analysed and published in collaboration with the group of prof. Ritch [26]. It was shown in this paper that the multimode threshold intensity is larger than for a single mode, since the atoms have to be trapped and localized in a complex potential. Therefore, the total pump power can be increased and the cooling time (and efficiency) improved. However, this comes at a cost of self-organization efficiency, which optimally occurs for a single standing wave. Nevertheless, this new multimode regime is still interesting from the trapping point of view since it can be used to demonstrate the less predictable interaction of atoms with complex potentials, and applied for the simulation of quantum annealing [27].

So far, no experiment has investigated the interaction of cold atoms with a frequency comb coupled to the optical cavity, neither in longitudinal nor transversal geometry. Therefore, the

results presented in this thesis offer a new and original insight into laser-atom interaction and the collective effects due to multimode excitation and complex light potentials.

Chapter 3

Collective effects in free space

The interaction of cold atoms with the frequency comb is the central idea of this thesis. Before looking into the complex interaction inside the optical cavity, we first investigate the collective effects that appear in free-space when the cold cloud interacts with the FC. Effects of high atom numbers or densities that modify the atom-light interaction or influence the radiation pressure force are of high importance for the applications of FC cooling or realization of multimode quantum memories. It is therefore instructive to look into the modification of the FC-induced radiation pressure force due to collective effects in cold samples of high density.

3.1 Radiation pressure force in dense clouds

3.1.1 Consideration of cw and FC excitation

It was shown in the theoretical section that the radiation pressure force and the subsequent spontaneous scattering are responsible for the cooling and trapping of atoms in a MOT. This approach is valid for single atoms, but does not hold for large ensembles. For samples of high density a modification of light scattering occurs, compared to dilute and single-atom physics. Cooperative scattering by an ensemble of resonant systems has been studied in detail by [44], which led to understanding of super-radiance and collective level shifts. The atoms can behave as coherently excited dipoles, enhancing the scattering in the forward direction compared to transverse directions. Since the scattered intensity is directly mapped to the radiation pressure force, a modification of cooling and trapping forces is well expected. Several experiments studied the cw-induced radiation pressure force, showing that the observed effects may not always be a signature of cooperativity, but a result of different mechanisms such as attenuation of the probe light, multiple scattering, diffraction and refraction, etc. [45, 46].

In contrast with the extensive studies using cw lasers, the investigations of light scattered from en ensemble of cold atoms illuminated by a frequency comb are scarce in the literature. We mentioned the potential of FC cooling, so it is necessary to understand the effects that could modify the FC-induced force. When the excitation of atoms in considered, a single FC mode will act as a cw laser. On the other hand, FC-atom interaction will generally be much more complex, as many comb modes that are present in the comb spectrum can simultaneously interact with the atoms [19]. In general, when atoms are excited by a train of phase-locked ultrashort pulses, coherent accumulation of population and coherence will occur only in the condition when the atomic relaxation rate (Γ) is slower than the pulse repetition rate (f_{rep}). The coherent effects depend on the comb spectrum and the atomic energy levels, so it is not trivial to make conclusions on the nature of the FC-atom interaction in specific applications. The FC-induced force on single atoms can be calculated using the optical Bloch equations and the Ehrenfest theorem, as described in [18] and outlined in the theoretical section. However, this approach becomes increasingly complex in dense ensembles, where the radiation pressure force starts to differ from the single-atom force.

3.1.2   Optical thickness and the Beer-Lambert law

We introduce the optical thickness of the sample as the main parameter describing the modification of the radiation pressure force. The laser beam intensity is attenuated due to absorption as it propagates through a medium along the x axis (the axis is chosen for consistency with the experimental setup):

$$\mathrm{d}I = -I\widetilde{n}(x,y,z)\sigma_{sc}(\omega_L)\mathrm{d}x, \tag{3.1}$$

where I is the laser intensity, $\widetilde{n}(x,y,z)$ spatially-dependent concentration (number density) of the medium, and $\sigma_{sc}(\omega_L)$ the frequency-dependent scattering cross-section. This gives the Beer-Lambert law:

$$I = I_0 e^{-b}, \tag{3.2}$$

where we introduced the optical thickness

$$b(y,z;\omega_L) = \int_{-\infty}^{\infty} \widetilde{n}(x,y,z)\mathrm{d}x = n(y,z)\sigma_{sc}(\omega_L). \tag{3.3}$$

Here, $n(y,z)$ is the column density of the medium, $n(x,y) = \int_{-\infty}^{\infty} \widetilde{n}(x,y,z)\mathrm{d}z$. For cold atoms, Doppler broadening can be neglected and the scattering cross-section is dominated by a single resonance closest to the laser frequency, with the detuning $\Delta_a = \omega_L - \omega_0$. The scattering

cross-section takes a simple form of a Lorentzian

$$\sigma_{sc}(\Delta_a) = \frac{\sigma_0}{1 + 4\Delta_a^2/\Gamma^2 + I/I_{sat}}. \tag{3.4}$$

Here, σ_0 in the on-resonance scattering cross-section [47]

$$\sigma_0 = \frac{\hbar\omega_0\Gamma}{2I_{sat}} \tag{3.5}$$

The optical thickness therefore depends on the spatial distribution of atomic density and the detuning of the probe beam from the atomic resonance. Atomic clouds in a MOT have a Gaussian density distribution, so the optical thickness will also have a Gaussian shape. We will show that the on-resonance optical thickness in the centre of the MOT cloud is the main parameter describing the modification of the FC-induced radiation pressure force. It is also instructive to note that the optical thickness of a sample can be determined by measuring the two light intensities I and I_0, with and without the absorbing sample, respectively. This is the idea behind absorption imaging, a technique that allows the imaging of a MOT cloud and its properties. The details of this technique will be given in the experimental section.

3.2 Experimental setup

In this section we give an overview of the experimental setup used for the preparation of a cold [87]Rb cloud and its characterization using absorption imaging, as well as the setup for the FC force measurements using fluorescence imaging. The experiment is controlled through a GUI, written by my lab colleagues Danijel Buhin and Ivor Krešić. The control panel is shown in Fig. 3.1.

3.2.1 Preparation and imaging of a cold [87]Rb cloud in a MOT

A cold [87]Rb cloud is loaded from a background vapour in a stainless-steel vacuum chamber using external cavity diode lasers (ECDL). The pressure level in the chamber is around 10^{-8} mbar. We cool and trap the Rb atoms using 780 nm light, which targets the D2 line ($\left|5S_{1/2}\right\rangle \to \left|5P_{3/2}\right\rangle$) of rubidium. The MOT is realized with the standard six-beam configuration, using a cooling beam red-detuned from the $\left|5S_{1/2}; F = 2\right\rangle \to \left|5P_{3/2}; F' = 3\right\rangle$ and a repumping beam near resonance with the $\left|5S_{1/2}; F = 1\right\rangle \to \left|5P_{3/2}; F' = 2\right\rangle$ transitions. Stabilization techniques for the ECDL lasers can be found in the thesis of dr. Neven Šantić [4], who implemented most of these techniques in our lab. Cooling laser is frequency stabilized to the cooling transition using
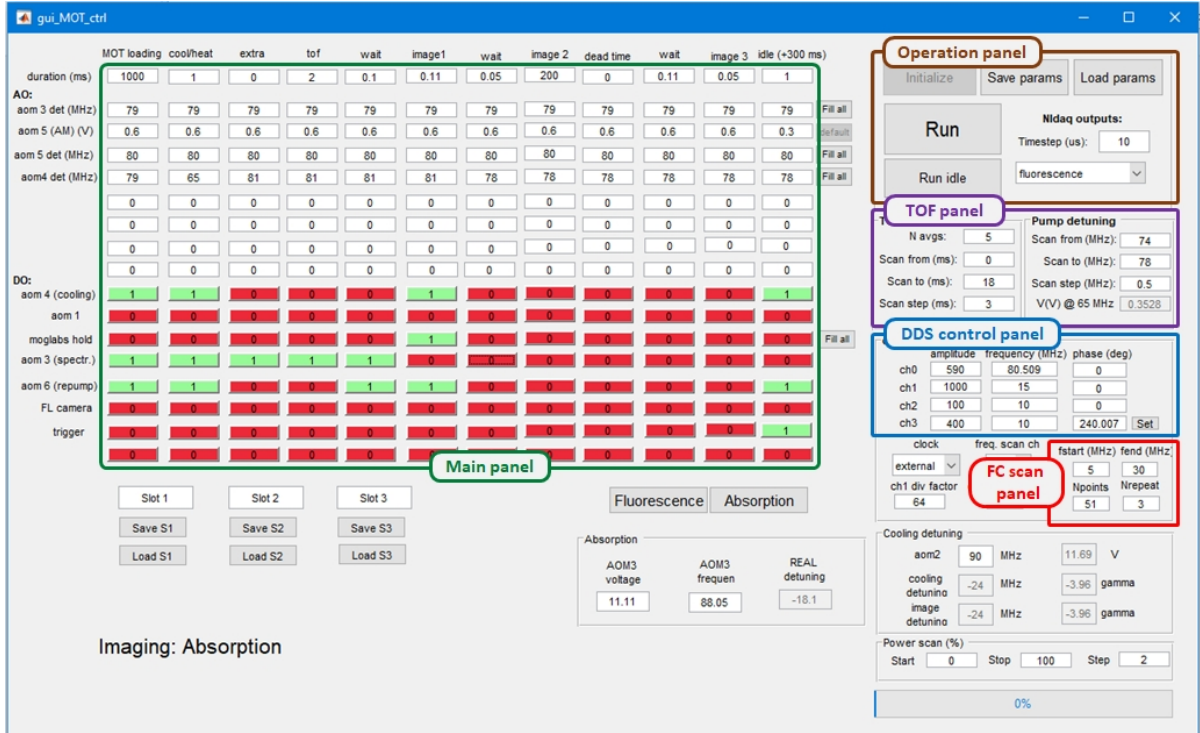
Figure 3.1: A GUI used to run the experiment. Several panels are shown, which allow us a full control of experimental parameters.

polarization spectroscopy, and detuned from the resonance using two acusto-optic modulators (AOMs) in double-pass configuration. Repumper laser is stabilized using saturation absorption spectroscopy (SAS) by modulating the laser current.

To achieve high densities needed in the experiment, the preparation of a cold cloud of a given optical thickness is achieved in three consecutive stages: MOT loading, temporal dark MOT, and repumping stage.

MOT loading stage This is the standard loading stage in which we load the MOT for 6 s, with the cooling laser detuned -3.5 Γ from the $F = 2 \rightarrow F' = 3$ transition, and the repumper laser in resonance with the $F = 1 \rightarrow F' = 2$. This generates a cloud of $\approx 4 \cdot 10^7$ atoms at a temperature of around 50 μK and a 1/e^2 radius of ≈ 0.8 mm. Here, $\Gamma = 2\pi \cdot 6.07$ MHz is the natural linewidth of the $\left| 5S_{1/2} \right\rangle \rightarrow \left| 5P_{3/2} \right\rangle$ transition [47]. Here it is important to note that for a large number of loaded atoms, multiple scattering of cooling/trapping light cannot be neglected and results in an effective repulsive force between the atoms, thus limiting the achievable high densities. This can even be seen during the MOT loading process. In the beginning of the loading cycle, the size of the cloud is mostly fixed and determined by the cloud temperature, and the number of atoms increases by increasing the cloud density. After a while, multiple scattering dominates

the process and the density in the centre of the cloud cannot increase further. In this regime, the number of atoms increases by increasing the size of the cloud, with the central density fixed [48]. To further increase the density of the cloud, reduction of the repulsive force is needed. For this, we introduce an additional stage in our preparation process, explained in more detail in [49].

Temporal dark MOT   In this stage we apply a 15 ms long temporal dark MOT where we reduce the power of the repumper laser to 10 μW (1% of initial power) and the detuning of the cooling laser to -2Γ, leaving other parameters unchanged. As a result, the atoms are optically pumped into the $F = 1$ ground state. The atoms in this state do not interact with the cooling/trapping light, hence the name dark state. This causes an increase of the cloud density and, consequently, of the optical thickness. Since the atoms in the dark state are not trapped, the dark MOT stage cannot last too long since the atoms will diffuse out of the cloud. Intuitively, it would seem as a better approach to detune the cooling laser further away from the $F' = 3$ and towards $F' = 2$ level to enhance the pumping into the $F = 1$ dark state. However, we change the detuning of the cooling beam with an AOM and its efficiency drops for larger detuning. With the available optical power, we find the transfer into the dark state for our experiment to be more efficient by tuning the laser closer to the $F' = 3$ level and increasing the total pumping probability.

Repumping stage   After increasing the density in the dark MOT stage, it is necessary to re-pump the atoms from the dark into the bright ground state $F = 2$ by increasing the power of the repumper laser to 1.5 mW. We also tune the cooling laser to -7Γ in order to re-cool and compress the cloud into a spherical shape while pumping all the atoms back into the bright state. The repumping stage lasts for 1 ms. It is important for the repumping stage to be as short as possible since longer interaction times would again lead to repulsion due to multiple scattering. The combination of these three stages allows us to prepare samples of optical thickness up to 21 in our experiment.

Absorption imaging   To determine the optical thickness of the experimentally prepared cloud, we use the Beer-Lambert law of beam attenuation. We illuminate the ^{87}Rb cloud with a large and weak imaging beam and record the beam spatial profile on a CMOS camera. The difference in the beam intensity with and without the atomic cloud is due to optical thickness of the cloud. For a probe propagating in the x direction, we label the beam intensity with no cloud present as $I_0(y, z)$ and the intensity after passing through the cloud as $I(y, z)$. The camera also picks

some background intensity I_{bg} that has to be subtracted, and we calculate the optical thickness as:

$$b(y, z) = -\ln\left[\frac{I(y, z) - I_{bg}(y, z)}{I_0(y, z) - I_{bg}(y, z)}\right] \tag{3.6}$$

For an atomic cloud of Gaussian density distribution, $b(y, z)$ will also have a Gaussian shape, as shown in Fig. 3.2(a). By fitting a 2D Gaussian to the measured $b(y, z)$, we extract the size of the ^{87}Rb cloud, as well as the optical thickness at the center of the cloud $b_{peak} = \sigma_{sc}(\Delta_{img})\int_{-\infty}^{\infty}\widetilde{n}(x; y = z = 0)\mathrm{d}x = \sigma_{sc}(\Delta_{img})n(y = z = 0)$, where Δ_{img} is the detuning of the probe laser frequency used for absorption imaging. For a large and weak imaging probe the effects of saturation can be neglected, $I_0/I_{sat} \ll 1$, so the on-resonance optical thickness b_0 is calculated using

$$b_0 = b_{peak} \cdot \left(1 + 4\Delta_{img}^2/\Gamma^2\right). \tag{3.7}$$

The on-resonance optical thickness is therefore defined as $b_0 = \sigma_0\int_{-\infty}^{\infty}\widetilde{n}(x; y = z = 0)\mathrm{d}x = \sigma_0 n(y = z = 0)$. In most cases it is necessary to use a detuned imaging beam, $\Delta_{img} \neq 0$, i.e. to measure the off-resonance optical thickness. The reason for this is that for high optical densities, the spatial profile of $b(y, z)$ will no longer be a Gaussian, as seen in Fig. 3.2(b). The flattening of the curve occurs at around $b_0 \approx 3$, so the optical densities above this value need to be measured off-resonantly and subsequently calculated by knowing the detuning of the imaging beam from the transition.
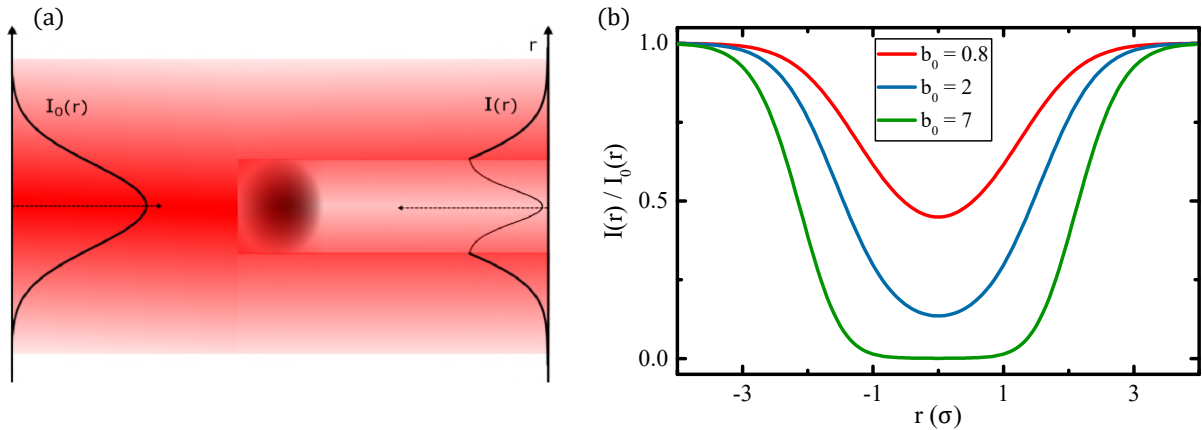
Figure 3.2: Principle of absorption imaging of a MOT cloud. (a) After passing through a Gaussian shaped atomic cloud, the absorbed fraction of a large laser beam will also have a Gaussian shape. Imaging the shape of the beam without the cloud, $I_0(r)$ and after passing through the cloud $I(r)$ allows us to determine the optical thickness of the cloud. (b) Shape of the beam intensity $I(r)$ after passing through a cloud of high optical thickness. For large b_0, the beam is fully absorbed even in the wings and flattening of the curve occurs. To decrease b_0, off-resonant imaging is used and the Gaussian shape is recovered.

Along with the cloud size and optical thickness, we can determine the number of atoms in the cloud N using absorption imaging:

$$N = \int \int \int \widetilde{n}(x,y,z)\mathrm{d}x\mathrm{d}y\mathrm{d}z = \int \int n(y,z)\mathrm{d}y\mathrm{d}z = \frac{1}{\sigma_{sc}(\Delta_{img})} \int \int b(y,z)\mathrm{d}y\mathrm{d}z. \quad (3.8)$$

An example of a signal acquired by absorption imaging is shown in Fig. 3.3. In Fig. 3.3(a) a profile of the imaging probe beam is shown and several diffraction pattern are visible, due to specks of dust and impurities on optical elements. In 3.3(b) a part of the beam is absorbed as it passes through the rubidium cloud. From these two signals, 3.3(c) is acquired, giving the optical thickness of the prepared sample. We note here that most of the diffraction patterns are divided out, so the beam does not have to be perfectly smooth for the technique to be successful. It is also useful to have a large probe beam, as similar to the plane wave as possible since it allows a better distinction between the beam profile and the cloud profile.

For a spherical cloud of radius R and a Gaussian density distribution, $\widetilde{n} = n_0 e^{-r^2/(2R^2)}$, with $r^2 = x^2 + y^2 + z^2$, integrating over the whole volume gives the number of atoms $N = n_0(2\pi R)^3$. Optical thickness in the center of a spherical cloud is $b = \sigma_{sc} n_0 \sqrt{2\pi} R$. Combining these two equations, we can write:

$$b = \frac{\sigma_{sc}}{2\pi} \frac{N}{R^2}. \quad (3.9)$$

This expression intuitively shows that the optical thickness is effectively determined by the number of atoms filling up the area of the cloud perpendicular to the beam propagation. For a non-symmetric cloud, we need to use different radii (R_x, R_y, R_z).

(a)   (b)   (c)
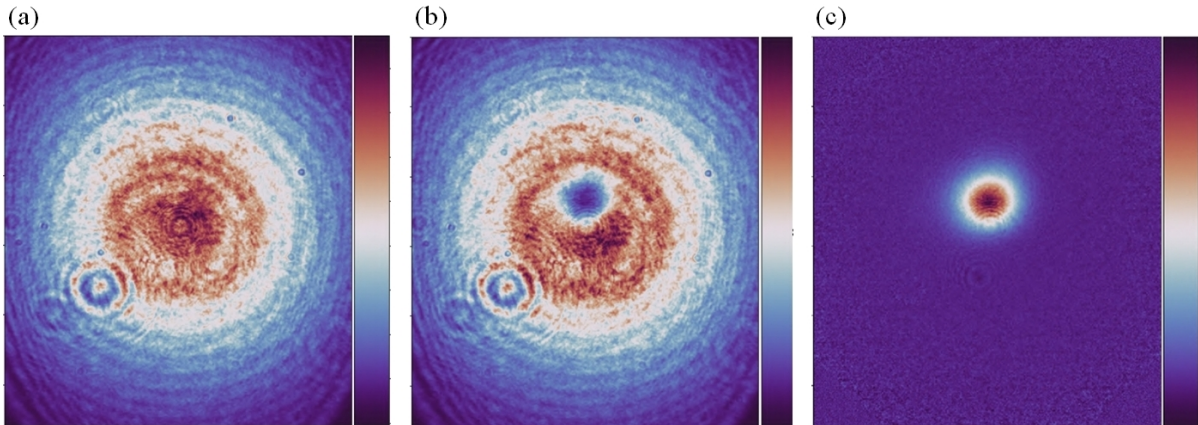
Figure 3.3: Absorption imaging of a cold cloud on a camera. Intensity distribution of the large imaging beam is shown (a) without the cold cloud and (b) after passing through the cloud. Several diffraction patterns due to specks and impurities are seen. In (c) the image of the cloud is extracted from (a) and (b), giving the spatial distribution of optical thickness of the cloud.

3.2.2   Measurement procedure

A simplified scheme of the experimental setup for the preparation of a cold ^{87}Rb cloud and its characterization using absorption imaging as well as the setup for FC force measurement using fluorescence imaging is shown in Fig. 3.4(a). The FC and the absorption imaging beam are overlapped and both propagating in the x direction, so that the optical thickness measured by the probe beam is the same as seen by the FC beam during force measurements. This means that only one of the beams can be turned on simultaneously, since the FC beam would strongly saturate or damage the absorption imaging camera. Thus, during the imaging (force measurement) period, the FC beam (imaging beam) is blocked.
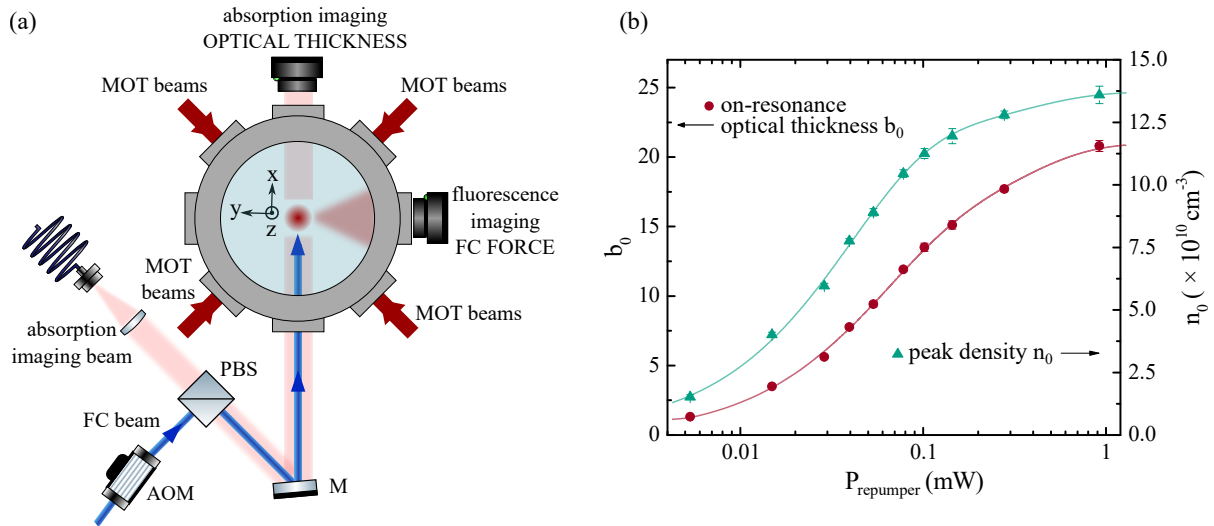
Figure 3.4: (a) Simplified experimental scheme. Two pairs of MOT beams are shown, while the third pair is propagating along the z axis. The absorption imaging beam and the FC beam are co-propagated in the x axis. The optical thickness is measured using the absorption imaging camera, while the FC force is measured using the fluorescence imaging camera. During the measurement of optical thickness, the FC beam is blocked. M is a mirror; PBS is a polarizing beam splitter. (b) On-resonance optical thickness (red circles) and cloud peak density (green triangles) as a function of the repumper laser power during the MOT loading stage. Solid lines represent a guide for the eye.

Control of the optical thickness   In order to vary the optical thickness of the cloud, we change the power of the repumper laser in the MOT loading state, leaving the dark MOT and the repumping state parameters unchanged. This change in the loading stage also affects other cloud parameters, such as size, number of atoms, and temperature. This does not affect the accuracy of optical thickness determination since it is measured directly by absorption imaging; nevertheless, we made a detailed characterization of all cloud parameters. In Fig. 3.4(b), the

peak density, $n_0 = n(x = y = z = 0)$, and on-resonance optical thickness, b_0, are shown as a function of the repumper laser power in the MOT loading stage. For the given range of powers, the cloud temperature varies from 35 μK to 75 μK, measured using a standard (TOF) technique [50].

FC force measurement   The FC is generated by frequency doubling an Er:fiber mode-locked femtosecond laser (TOPTICA FFS) operating at 1560 nm with a repetition rate of $f_{rep} = 80.495$ MHz. The frequency-doubled spectrum is centered around 780 nm with an FWHM of about 5 nm and a total output power of 76 mW. The optical frequency of the n-th comb mode is given by Eqn. (2.56). The scheme of FC locking is shown in Fig. 3.5 and is presented in more detail in Neven's thesis [4]; here I briefly outline the procedure. To lock the FC, two degrees of freedom need to be stabilized, and we lock f_{rep} and f_n. The repetition frequency is measured on a photodiode and referenced to a DDS with the stability of a Rb standard. The error signal generated on a phase detector is fed to the PZT of the FC, which changes the cavity length and stabilizes f_{rep}. The optical frequency is locked by first beating the FC with the Rb cooling laser, which gives an rf frequency difference f_{beat} between the cooling laser and the closest FC mode. We then reference the beat frequency with a DDS signal on a phase detector and feed the error signal to the FC pump diode current, thus locking f_n and, indirectly f_0. The frequency of the n-th comb mode is varied by scanning f_{beat} (and f_0) while keeping f_{rep} fixed.
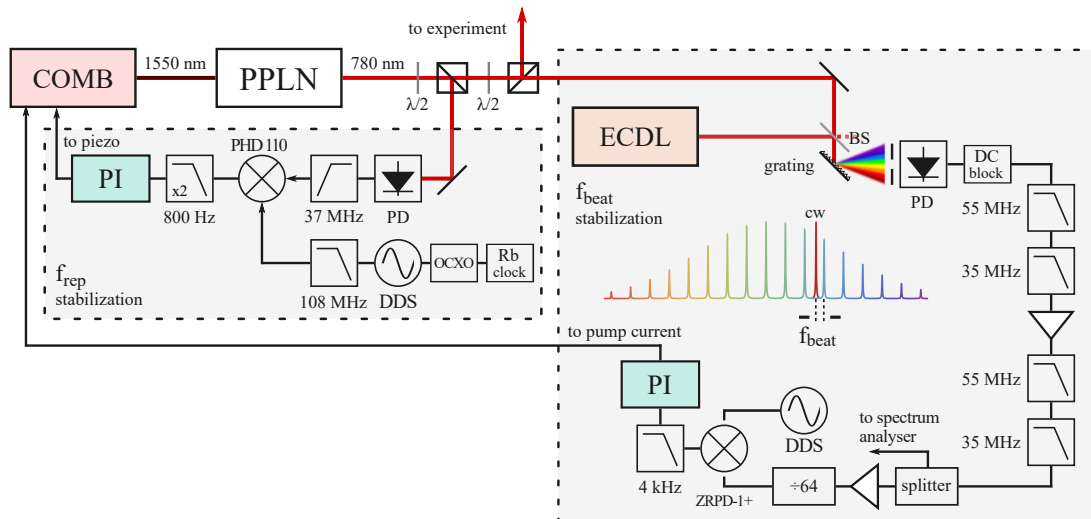
Figure 3.5: Scheme of the optical and electronic setup for fully stabilizing the FC using an ECDL reference. The left and right sections of the image show the scheme for stabilizing and f_{beat}, respectively. PPLN: periodically poled lithium niobate crystal, PD - photodiode, $\lambda/2$ - half-wave plate, DDS - direct digital synthesizer, OCXO - oven controlled crystal oscillator, ECDL - external cavity diode laser, BS - beam splitter. Taken from [4].

The complete experimental procedure is presented in Fig. 3.6, showing the cloud preparation stage, followed by either absorption imaging of the cloud to measure its optical thickness or by the FC force measurement, since one of the beams has to be blocked, as already mentioned.
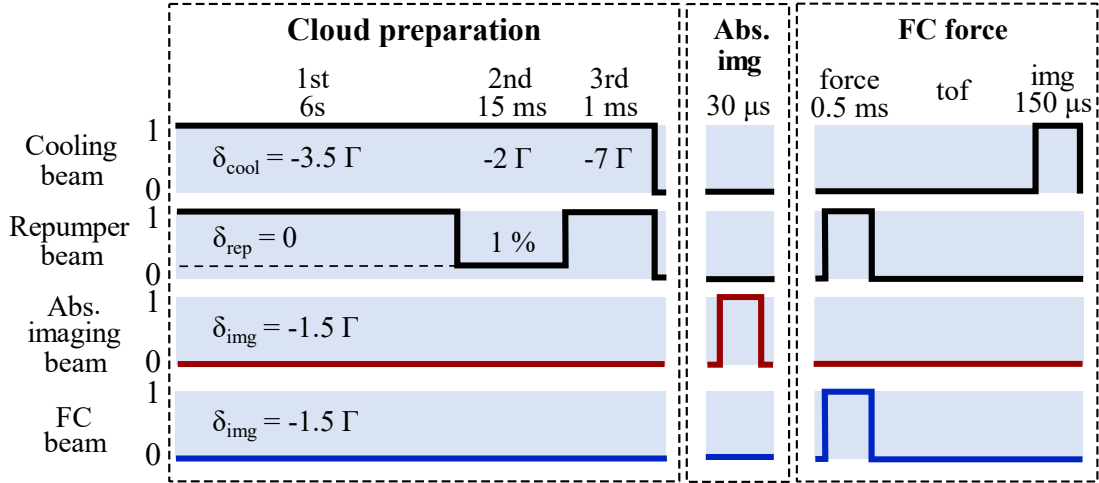
Figure 3.6: Experimental sequence showing the cloud preparation, followed by either absorption imaging or FC force measurement.

The FC force measurement sequence starts after the preparation of a cloud of a given optical thickness and is similar to the one described in our papers and thesis [18, 20, 4]. At $t = 0$ we turn off the MOT cooling beams and switch on the linearly polarized FC beam. The total power of the FC beam on the atoms is 25 mW and the beam size ($1/e^2$) is 4.5 mm, resulting in the power and intensity per comb mode of about 75 μW and 9 μW/cm^2, respectively. The MOT repumper laser is left on to continuously pump the atoms out of the $\left|5S_{1/2}; F = 1\right\rangle$ ground level and has no measurable mechanical effect. The quadrupole magnetic field is also left on. We let the comb interact with the cold cloud for 0.5 ms. During this time, the center of mass (CM) of the cloud accelerates in the FC beam direction ($+x$ direction) due to the FC force. The FC and repumper beams are then switched off, and the cloud expands freely for a variable time, after which we switch on the MOT cooling beams for 0.15 ms and image the cloud's fluorescence with a camera to determine its CM displacement.

It is worth noting here that the approaches to change the optical thickness of the cloud by changing the repumper laser power immediately after the dark MOT stage used in experiment [51], and by changing the cloud's expansion time before interaction as used in experiment [52], are not applicable in our case of the FC excitation. In the first approach, only a fraction of atoms are transferred from $\left|5S_{1/2}; F = 1\right\rangle$ to $\left|5S_{1/2}; F = 2\right\rangle$ ground level after the dark MOT stage, depending on the repumper laser power. Atoms remaining in the $\left|F = 1\right\rangle$ level and atoms in $\left|F = 2\right\rangle$ could be simultaneously excited by different comb modes, which would result in a

complex lineshape of the measured FC force. In the second approach, the size of the FC beam should be bigger than the size of the expanding cloud to make sure the force is acting on the whole cloud. This cannot be achieved in our setup due to the low available power per comb mode, so no measurable mechanical effect could be detected.

3.3 Results and discussion

3.3.1 FC force as a function of cloud density

Hyperfine energy levels of ^{87}Rb and the relevant optical transitions for the FC excitation are shown in Fig.3.7(a). In Fig. 3.7(b), we show the measured FC force, F_{FC}^N, as a function of the FC detuning δ, which we define as the detuning of the n-th comb mode from the $\left|5S_{1/2}; F = 2\right\rangle \to \left|5P_{3/2}; F' = 3\right\rangle$ transition, for different peak cloud densities, n_0. Due to the nature of the comb spectrum, the FC radiation pressure force is periodic with respect to the comb detuning with a period equal to f_{rep}. Two distinct peaks appear in one f_{rep} scan, reflecting the interaction with three comb modes, as explained in detail in our paper [18]. The peak at $\delta = 0$ is due to the n-th comb mode being in resonance with the $\left|5S_{1/2}; F = 2\right\rangle \to \left|5P_{3/2}; F' = 3\right\rangle$ transition, whereas the peak at $\delta \approx$ -25.5 MHz is due to the $(n - 3)$-rd mode being in resonance with the $\left|5S_{1/2}; F = 2\right\rangle \to \left|5P_{3/2}; F = 2\right\rangle$ transition and the $(n - 5)$-th mode with the $\left|5S_{1/2}; F = 2\right\rangle \to \left|5P_{3/2}; F = 1\right\rangle$ transition. For completeness, Fig. 3.7(c) shows the calculated FC force, F_{FC}^1, obtained by summing the contributions from three hyperfine transitions. The FC force is calculated for a single atom using the optical Bloch equations and the Ehrenfest theorem. The details of single-atom FC force calculation can be found in [18].

As the cloud density increases, broadening and reduction of both FC force peaks are observed. However, these effects are not equally pronounced for both peaks, as can be seen from the peak ratio of the peaks at $\delta = 0$ and $\delta \approx$ -25.5 MHz. The peak ratio decreases with increasing density, as can be seen from the inset in Fig. 3.7(b). For applications of multi-line excitation it is thus important to consider that, for a sample of fixed density, as is usually prepared in most experiments, broadening and reduction of the FC radiation pressure force will vary for different transitions. The peak ratio of 2.8 is expected when n_0 approaches zero, as it reflects the ratio of the $|F = 2\rangle \to |F' = 3\rangle$ and $|F = 2\rangle \to |F' = 2\rangle$ transition dipole moments [47]. This can be easily understood given the well-known result that the force broadening and reduction due to collective effects in many-atom ensembles depend on the optical thickness rather than the density [53]. Since the optical thickness is defined through the scattering cross-section, with the saturation intensity that depends on the dipole moment of the relevant transition [47], the
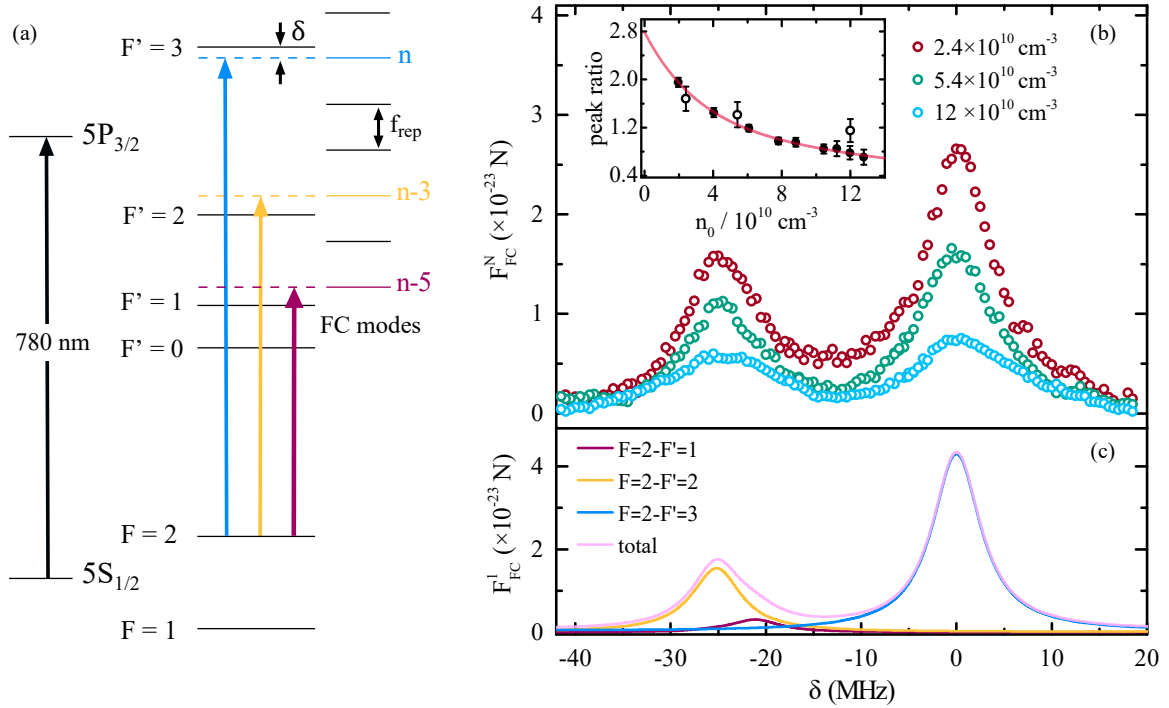
Figure 3.7: (a) Hyperfine energy levels of ^{87}Rb D2 line (780 nm) and the relevant optical transitions for the FC excitation. (b) Measured FC force, F_{FC}^N, as a function of the FC detuning δ, for different peak densities n_0. Inset shows the ratio of the FC peak forces at $\delta = 0$ and $\delta \approx$ -25.5 MHz, where the symbols are experimental data and the line represents a guide for the eye. Full circles correspond to averaged multiple scans, as described in the experimental section. Empty circles correspond to peak ratios of the scans shown in (b), which were taken without averaging and thus have larger errors. (c) Calculated FC force, F_{FC}^1, as a function of the FC detuning δ. The total FC force (violet line) is obtained by summing the force contributions from three $\left|5S_{1/2}; F = 2\right\rangle \to \left|5P_{3/2}; F' = 1, 2, 3\right\rangle$ hyperfine transitions.

two peaks have different optical densities for a given atomic density and therefore different factors of force reduction, which directly affects the peak ratio. In the following sections, we will therefore present and analyze the dependence of the FC force on the optical thickness for each force peak separately.

3.3.2   FC force as a function of cloud optical thickness

Fig. 3.8 shows the measured FC force F_{FC}^N as a function of the FC detuning δ for different on-resonance optical densities b_0. In the case of $|F = 2\rangle \to |F' = 3\rangle$, b_0 is measured directly as described in the experimental section. Since the transition dipole moment for the $|F = 2\rangle \to |F' = 2\rangle$ is 2.8 times smaller, we divide the measured b_0 with this factor to obtain the relevant

b_0 for the $|F = 2\rangle \rightarrow |F' = 2\rangle$ transition. The largest optical thickness for our experiment is $b_0 \approx 21$ measured on the $|F = 2\rangle \rightarrow |F' = 3\rangle$ transition, which corresponds to the maximum of $b_0 \approx 7.5$ in the case of $|F = 2\rangle \rightarrow |F' = 2\rangle$ transition.
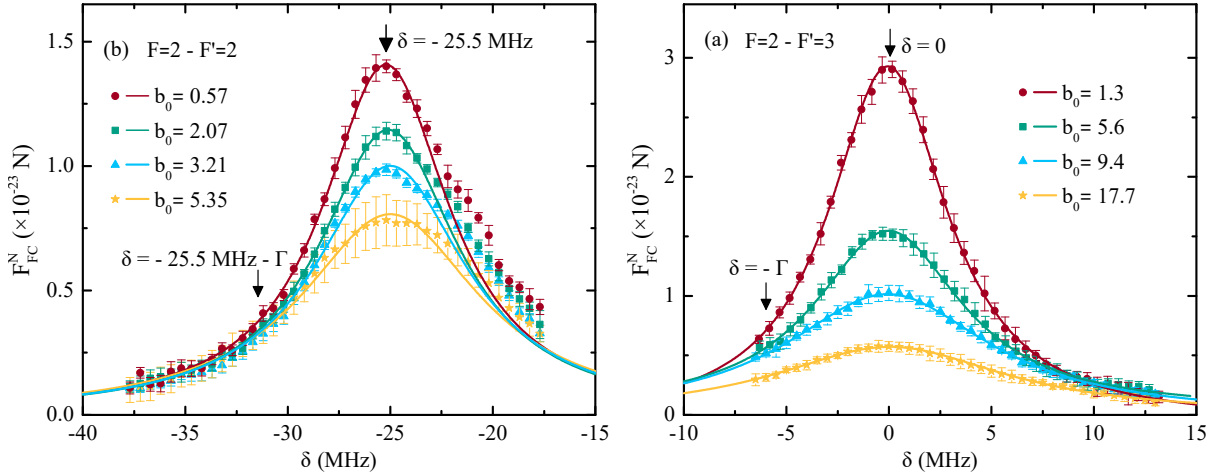
Figure 3.8: Measured FC force (symbols) as a function of detuning δ for different optical densities b_0. (a) FC force is due to the n-th comb mode being in resonance with the $|F = 2\rangle \rightarrow |F' = 3\rangle$ transition. (b) FC force is due to the $(n-3)$-rd being in resonance with the $|F = 2\rangle \rightarrow |F' = 2\rangle$ transition and the $(n-5)$-th mode with the $|F = 2\rangle \rightarrow |F' = 1\rangle$ transition. For the $|F = 2\rangle \rightarrow |F' = 2\rangle$ transition, we fit only to the data on the red side of the curve, where the influence of the $|F = 2\rangle \rightarrow |F' = 1\rangle$ transition is negligible. A solid line shows a Lorentzian fit to the experimental data. The arrows show detunings that were chosen to show dependences on b_0 in Fig. 3.9.

The measured FC forces arising from the $|F = 2\rangle \rightarrow |F' = 3\rangle$ transition show a Lorentzian lineshape in the whole range of measured b_0, see Fig. 3.8(b). In the case of the $|F = 2\rangle \rightarrow |F' = 2\rangle$ transition, the FC forces deviate from the Lorentzian shape, see Fig.3.8(a), due to the $|F = 2\rangle \rightarrow |F' = 1\rangle$ force contribution positioned in the blue wing of the peak, as indicated in Fig. 3.7(c).

For a given b_0, a Lorentzian function is fitted to the experimental data. For the $|F = 2\rangle \rightarrow |F' = 2\rangle$ transition, we fit only to the data on the red side of the curve, where the influence of the $|F = 2\rangle \rightarrow |F' = 1\rangle$ transition is negligible. While the FC force offset should be zero, experimentally we see a small offset due to inaccuracies in determination of the initial and final position of the cloud's CM, from which the force is determined. The value of this offset depends on the optical thickness since the imaging signal-to noise depends on the cloud parameters. However, the relative offset is around 10% of the peak force value (at $\delta = 0$) for all optical densities in the case of $|F = 2\rangle \rightarrow |F' = 3\rangle$ transition, and around 15% of the peak force value (at $\delta \approx$ -25.5 MHz) in the case of $|F = 2\rangle \rightarrow |F' = 2\rangle$ transition. The small FC force offset is subtracted from all experimental data shown in Figs. 3.8 and 3.9. The FC force broadening and

reduction are clearly observed for both peaks shown in Fig. 3.8 (a) and (b). These effects are investigated in the following paragraph and presented in more detail in Fig. 3.9.

3.3.3 FC force broadening and reduction

Fig. 3.9(a) shows the measured (symbols) FC force linewidths, Γ_{FC}^N, as a function of b_0. For a given b_0, Γ_{FC}^N is obtained from the fit of a Lorentzian function to the measured FC force spectra as shown in Fig. 3.8. We observe an increase of the FC force linewidth with increasing b_0. For small b_0 the increase is linear, while the curve starts to flatten as b_0 increases. In the limit $b_0 \to 0$, the FC linewidth $\Gamma = 2\pi\cdot 6.07$ MHz is expected, as it reflects the natural linewidth of the ^{87}Rb $\left|5S_{1/2}\right\rangle \to \left|5P_{3/2}\right\rangle$ transition. For the largest $b_0 = 20.8$ achieved in the experiment, the FC force linewidth of 2.5 Γ is measured.
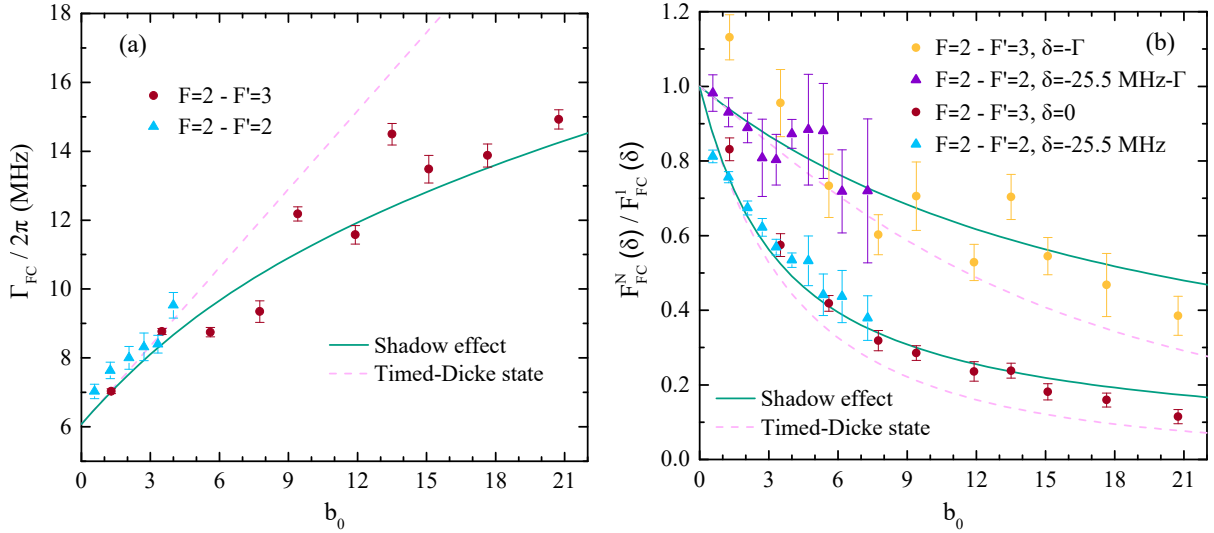
Figure 3.9: (a) Measured (symbols) and calculated FC force linewidth in the presence of shadow (solid line) and cooperative (dashed line) effects, Eqn. (3.15) and (3.16) respectively, as a function of b_0. (b) Measured (symbols) and calculated (lines) FC force reduction as a function of b_0 at $\delta = 0$ and $\delta = -\Gamma$ in the case of $|F = 2\rangle \to |F' = 3\rangle$ transition, and $\delta = -25.5$ MHz and $\delta = -25.5$ MHz $-\Gamma$ in the case of $|F = 2\rangle \to |F' = 2\rangle$ transition.

Fig. 3.9(b) shows the measured (symbols) reduction of the FC force, $F_{FC}^N(\delta)/F_{FC}^1(\delta)$, as a function of b_0. Same as the linewidths, $F_{FC}^N(\delta)$ are obtained from the measured FC force spectra as shown in Fig. 3.8(a) (for $\delta = 0$ and $\delta = -\Gamma$) in the case of $|F = 2\rangle \to |F' = 3\rangle$ transition, and in Fig. 3.8(b) (for $\delta = -25.5$ MHz and $\delta = -25.5 - \Gamma$) in the case of $|F = 2\rangle \to |F' = 2\rangle$ transition. The single-atom force $F_{FC}^1(\delta)$ is obtained by fitting Eqn. (3.15) derived from the Beer-Lambert law (see the following paragraph for details). A reduction of the FC force with

increasing optical thickness of observed. The force reduction is larger when the relevant comb mode is resonant with a given transition, i.e. when the n-th comb mode is in resonance with the $|F = 2\rangle \rightarrow |F' = 3\rangle$ transition ($\delta = 0$), and when the $(n - 3)$-rd mode is in resonance with the $|F = 2\rangle \rightarrow |F' = 2\rangle$ transition ($\delta \approx$ -25.5 MHz). These data also show that both transitions follow the same dependences on the optical thickness (both on- and off-resonance). For the largest $b_0 = 20.8$ achieved in the experiment, the FC force reduction of almost 90% is measured. We will now turn to the theoretical models used to describe and fit the measured data.

3.3.4 Theoretical analysis

In addition to the measured data, the calculated FC force linewidths and FC force reduction are also shown in Fig. 3.9 by solid and dashed lines. The calculations are performed for our experimental parameters using the theoretical models developed for the cw-induced radiation pressure force [45]. By doing so, we considered a single-comb mode participating in the interaction as a cw laser. This consideration is reasonable given that the FC pulse repetition rate, f_{rep}, is much larger than the natural linewidth of the relevant transition, Γ; thus, the scattering rate of the neighboring comb modes is strongly reduced due to the $(f_{rep}/\Gamma)^2$ dependence [18, 20, 17].

A detailed derivation of the average cw radiation pressure force resulting from the excitation of N atoms by a resonant laser can be found in [54] and is given by

$$F = \frac{hk_0\Gamma}{4\pi N} \int_0^{2\pi} \mathrm{d}\phi \int_0^{\pi} \mathrm{d}\theta \sin\theta (1 - \cos\theta) I_s(\theta, \phi). \tag{3.10}$$

Here, $I_s(\theta, \phi)$ is the far-field scattered intensity, and the angles determine the direction of the scattered photons, with the zenith given by the wavevector of the incident beam. Eqn.(3.10) shows that the angular pattern of the scattered intensity uniquely determines the radiation pressure force. To understand the force, it is necessary to discuss different scattering mechanisms relevant to our experimental conditions. Light scattering by an atomic cloud illuminated by a resonant laser can be decomposed into several contributions [45]: (a) the background radiation composed of diffuse scattering by all atoms, which is incoherent (in the sense that the phase of the scattered wave is random from one to another realization of atomic positions); (b) a forward lobe arising from diffraction of the incident beam from the cloud, i.e. Mie scattering in the single scattering order. This contribution is coherent in the sense that the scattered wave has a well-defined phase. (c) The coherent backscattering cone that arises from constructive interference during multiple scattering.

A full microscopic model built on a set of equations of N coherently coupled dipoles (CD)

can be used to calculate the scattering intensity [52, 53, 55]. This quantum model captures incoherent and coherent contributions, including all scattering orders, and can be extended to include atomic motion. However, due to computational complexity, the CD model is limited to small samples and, as such, is not investigated here. Likewise, it is difficult to distinguish the dominant effect, since all of them are taken into account in the computed result.

Another approach is to use semiclassical models to understand the different scattering contributions and their influence on the radiation pressure force. To investigate these contributions, we will follow the analysis developed in [45] for the cw-induced force. We will also extend this analysis to our range of optical densities ($b \approx 20$), since it has only been applied in the limit of $b < 1$. Diffuse scattering has two contributions to the force. The first one is called the "shadow effect" and comes as a result of progressive attenuation of light intensity through the cloud due to diffuse scattering. It can be explained by the Beer–Lambert law, i.e., the exponential decrease of the intensity results in broadening and reduction of the overall radiation pressure force. The force reduction arising from the shadow effect can be calculated combining the Gaussian density distribution of the cloud with exponential intensity attenuation. For a beam propagating in the x direction and passing through a spherically symmetrical Gaussian cloud, the transmitted intensity is

$$T = \frac{I_T}{I_0} = \exp\left(-\sigma_{sc}(\delta)n_0 \int e^{-r^2/(2R^2)} \mathrm{d}z\right) = \exp\left(-b(\delta)e^{-r_\perp^2/(2R^2)}\right), \tag{3.11}$$

with $r_\perp^2 = y^2 + z^2$ and $b(\delta) = \sigma_{sc}(\delta)n_0$. The scattered intensity is the one not transmitted, and integrating over the transverse profile of the cloud gives the total scattering cross-section:

$$\sigma_{BL} = \int \left(1 - T(r_\perp)\right) \mathrm{d}^2\mathbf{r}_\perp = 2\pi R^2 \mathrm{Ein}(b), \tag{3.12}$$

where we used a change of variable $u = be^{-r_\perp^2/(2R^2)}$ and $\mathrm{d}^2\mathbf{r}_\perp = 2\pi r_\perp \mathrm{d}r_\perp$, with the Ein function given by

$$\mathrm{Ein}(b) = \int_0^b \frac{1 - e^{-u}}{u} \mathrm{d}u = b\left[1 + \sum_{n=1}^\infty \frac{(-b)^n}{(n+1)(n+1)!}\right] \tag{3.13}$$

Using Eqn. (3.13) we can write the cross-section as

$$\sigma_{BL} = N\sigma_{sc} \cdot \frac{\mathrm{Ein}(b)}{b}. \tag{3.14}$$

For $b \ll 1$, we recover the single-atom physics where the total cross-section is just the sum of

individual atoms, $\sigma_N = N\sigma$. However, the total cross-section is reduced due to attenuation of the beam as it passes through the cloud.

Combining this cross-section with Eqn. (3.10) to determine the correction to the radiation pressure force due to shadow effect, we get

$$\frac{F_{shadow}}{F_1} = \frac{\text{Ein}(b)}{b},\tag{3.15}$$

where we assumed isotropic radiation, F_1 is the single-atom radiation pressure force, and $b = b_0/(1 + 4\delta^2/\Gamma^2)$.

We calculate F_{shadow} spectra as a function of b_0 for our experimental parameters, from which we extract the $F_{shadow}(\delta)$ and linewidths. In order to obtain $F_{FC}^1(\delta)$ we fit Eqn. (3.15) to the measured FC force data as a function of b_0 for a given detuning F_{FC}^N, with $F_{FC}^1(\delta)$ as a free fitting parameter. Then the determined $F_{FC}^1(\delta)$ is used as a scaling factor for normalization of all $F_{FC}^N(\delta)$ forces shown in Fig. 3.9(b). The calculated force linewidth and reduction as a function of b_0 resulting from the shadow effect are shown in 3.9(a) and 3.9(b) with solid green lines. We emphasize here that the normalizing amplitude is the only adjustable fitting factor. The dependence on b_0 is calculated as predicted by Eqn. (3.15). The calculated values show good agreement with the measured data for both on- and off-resonant excitation.

The second contribution to the force due to diffuse scattering is a consequence of the first one, i.e., since the light intensity is larger at the entrance of the cloud than at the exit, more light is scattered in the backward than in the forward direction. This causes an anisotropy of the emission pattern, which slightly increases the radiation pressure force. This anisotropy can numerically be simulated using a random walk approach as done in [45] and becomes significant only at large optical densities. Based on [56] we estimate that, for the largest $b_0 = 20.8$ achieved in the experiment, the force including corrections due to anisotropy is around 10% larger than the F_{shadow}, i.e. $F_{diffuse} = F_{shadow} + F_{anis} \approx 1.1 F_{shadow}$. This correction is within the uncertainty of the experimental data. For lower b_0, this effect is even less pronounced.

The contribution to the force due to diffraction of the incident beam can be calculated for clouds of small optical thickness [57] employing the Mie scattering approach. As stated in [58, 59], this contribution is significant for very small atomic clouds ($kR \approx 10$) and for probe lasers tuned far-off resonance; it is therefore negligible for condition used in our experiment with a large cloud ($kR > 1000$) and on-resonant excitation. Here, k is the wave vector and R is the radius of a cloud of a Gaussian density distribution.

The coherent backscattering contribution cannot be calculated using semiclassical models but requires the full microscopic CD model [45, 53, 60, 61]. However, its contribution is also

negligible for large clouds ($kR > 1000$) and on-resonant excitation such as in our experiment.

Because of its importance in the earlier experimental and theoretical papers [51, 62, 60, 45], we also mention an alternative approach used to investigate the radiation pressure force. It describes the force reduction as a consequence of coherent collective (i.e. cooperative) scattering of atomic dipoles. This cooperative contribution to the force can be calculated using a mean-field approach inspired by the timed-Dicke state (TDS). This model assumes that all atoms are driven by the unperturbed laser beam, i.e. the atoms acquire the phase of the laser, and all have the same excitation probabilities. It neglects reabsorption of photons by other atoms and works in conditions of small probe laser intensity or large detunings. The TDS approach has become widely used in recent years, as it provides an explanation of experimental results on superradiance [44, 63], a hallmark of cooperative effects. Cooperative radiation pressure force, F_{TDS} was studied in detail in [51, 62] and can be calculated from

$$\frac{F_{TDS}}{F_1} = \frac{4\delta^2 + \Gamma^2}{4\delta^2 + (1 + b_0/8)^2\Gamma^2}\left[1 + \frac{b_0}{16(kR)^2}\right]. \tag{3.16}$$

We calculate F_{TDS} spectra as a function of b_0 for our experimental parameters, from which we extract the $F_{TDS}(\delta)$ and linewidths. The calculated force linewidth and reduction are shown in 3.9(a) and 3.9(b) with dashed violet lines.

The TDS force linewidth agrees with measured data for small b_0 and coincides with the shadow effect curve up to $b_0 \approx 3$. However, at larger optical densities, the TDS model predicts a linear increase of the force linewidth, which is not supported by our experimental results, as it does not include multiple scattering effects that can induce the flattening of the force linewidth curve at large b_0 [62].

On the other hand, the good agreement of the force reduction calculated from the shadow and TDS models (see Fig. 3.9(b)) even for intermediate b_0 explains why, in earlier studies [51], the reduction of the force was attributed to atomic cooperativity. However, the results of the force broadening given in Fig. 3.9(a) clearly indicate that this agreement can be misleading, and point to the shadow effect as the dominant contribution to the force in dense atomic clouds.

In the conditions when the atoms are resonantly excited by the frequency comb, the beam attenuation due to diffuse scattering is the dominant physical mechanism defining the radiation pressure force, and the atomic cooperativity effects are negligible. This conclusion is in good agreement with measurements of super-radiance, where super-radiant enhancement was observed only for mid- to large detunings, while tuning the probe close to resonance results in suppression of super-radiant (cooperative) behavior [63].

Conclusion We have measured the frequency-comb-induced radiation pressure force acting on a cold ^{87}Rb cloud as a function of the optical thickness of the cloud and observed reduction and broadening of the frequency comb force as the optical thickness increases. We discussed different scattering mechanisms and their contributions to the force and showed that for our experimental conditions a single scattering mechanism dominates the radiation pressure force. It comes as a result of progressive attenuation of light intensity in the cloud due to diffuse scattering of light, i.e., the shadow effect.

We also review the cooperative timed-Dicke state approach used in earlier experiments to discuss and clarify the possible points of confusion due to historical reasons and previous research. We used the theoretical models originally developed for cw radiation pressure force to describe the measured frequency comb force. The measured and the calculated force broadening and reduction arising as results of the shadow effect are in good agreement. The cooperative force agrees with measured data for small b_0; however the behavior of force linewidth and force reduction at larger optical densities is not supported by the experiment. These results confirm the analogy between the cw and a single comb-mode interaction.The influence of the off-resonance comb modes on the comb–atom interaction is minor and can be neglected even in the case of increased cloud optical thickness, and models developed for cw excitation can be readily applied.

For the applications of FC cooling in free-space, near-resonant excitation is needed, so our results show that a semi-classical approach is sufficient to describe the FC-induced force up to $b_0 \approx 20$ and no measurable cooperative effects occur. In order to observe the signature of the cooperativity in the radiation pressure force, it would be necessary to work in the parametric regime where the beam attenuation due to diffuse scattering is negligible, such as in large detunings from the atomic resonance.

The results presented in this thesis contribute to the understanding of scattering of the frequency comb light by an ensemble of cold atoms in free space, thus paving the way toward novel frequency comb applications in the field of cooling, quantum communication, and light–atom interfaces based on structured and disordered atomic systems.

Chapter 4

Collective effects inside an optical cavity

In the last chapter we investigated collective effects that occur when a cold and dense atomic cloud is interacting with a probe laser beam. The light intensity is constant and steady state is quickly achieved, where scattering of light into free-space modes dominates the losses.

On the other hand, dynamics inside an optical cavity becomes more complex and coupled. The interaction of atoms with the intracavity light shifts the cavity resonance, thus changing the intracavity intensity and, therefore, the interaction strength. Photon leakage through the cavity mirrors appears as an additional dissipative mechanism, which can even be stronger than the free space scattering. Here, detunings of the laser frequency from both the atomic and cavity resonance, Δ_a and Δ_c, play a significant role in the coupled dynamics.

For an ensemble of atoms inside the cavity, each atom is coupled to the cavity mode. For a large number of atoms, the collective coupling can become stronger than the losses (cooperativity $\mathcal{C} \geq 1$), bringing the dynamics from the weak- to the strong-coupling regime. The collective dynamics shows new exciting effects, such as self-organization of atoms, not predicted by the single-atom physics.

4.1 Design of the optical cavity

4.1.1 Initial design considerations

To increase the atom-cavity interaction as much as possible, a careful consideration of cavity parameters is needed. High-finesse cavities are needed to minimize the losses through the mirrors, κ. To maximize the single-photon Rabi frequency, g, cavities of short length are needed to minimize the mode volume. In experiments working with single (or a few) atoms, special micro-cavities can be built, and the system exhibits strong-coupling behavior even for a single

atom [64].

In our experiment we use a ^{87}Rb cloud loaded in a MOT, so enough space is needed for the whole cloud to be loaded or transferred into the cavity. For this reason, micro-cavities are not a practical option when working with large ensembles in a MOT.

The main goal of the experiment is interaction of atoms with a frequency comb coupled into the cavity, so it is crucial to match the cavity length with the FC repetition frequency and to couple as many FC modes into the cavity as possible. The repetition frequency of our FC is $f_{rep} = 80.5$ MHz, so to couple every comb mode into the cavity, the cavity would have to be almost 2 m long. The cavity needs to be mounted in the MOT vacuum chamber, so a cavity of this length is not possible. Therefore, we can couple every m-th comb into the cavity, i.e. we're filtering the comb frequencies with our cavity. For a longer cavity, we can couple more FC modes, but the cavity mode volume increases, and the single-photon Rabi frequency decreases.

Another consideration is the cavity geometry. We chose a confocal geometry due to it's stability and robustness. A concentric cavity of the same length would have a smaller mode volume than a confocal one and a larger interaction strength; however the mode waist would be smaller which limits the number of atoms coupled to the cavity mode. The confocal geometry allows a better spatial overlap of the MOT cloud and the cavity mode.

From the available mirrors, we chose a pair broadband mirrors of radius of $R = 7.5$ cm (Layertec 103953) and for the confocal geometry $L = R$ is required. However, it is crucial to match the length of the cavity to the multiple of FC repetition frequency, $FSR = mf_{rep}$. For a length $L = 7.757$ cm every 24-th comb mode is coupled into the cavity, $FSR = 24f_{rep}$, and gives $FSR = 1.932$ GHz. This means that our cavity is near-confocal and the higher-order cavity modes will not be degenerate. The deviation from confocality is large enough for the modes to be fully resolved, with around 40 MHz separation between the modes. The Gaussian mode waist is calculated to be $w_0 \approx 100$ μm and, with the effective Gaussian mode volume $V = w_0^2 \pi L/2$, the single-photon Rabi frequency is $g \approx 2\pi \cdot 138$ kHz.

Mechanical design. The cavity assembly used in our experiment is shown in Fig. 4.1. The cavity mirrors are glued onto the holders, which are tightened with screws to the main bridge. While untightened, the holders can slide along the bridge, which allows adjusting the cavity length to match it to the frequency comb. All the parts are made from stainless steel, and we used a vacuum compatible glue (Loctite 9492) so it is safe during vacuum baking, after we mounted the assembly into the MOT chamber. A piezo transducer ring (PZT) was glued to one of the mirrors, which allows scanning the cavity length. The hole in the middle of the bridge allows unobstructed propagation of the MOT beams.

The maximum stroke of the PZT is 3 μm, which gives $\Delta FSR \approx 75$ kHz. For our laser system, $\Delta f_{rep} \approx 30$ kHz, but since we couple every 24-th comb mode into the cavity, it gives a tuning range of 720 kHz. Combined, this allows a mismatch of less than 1 MHz (relative to 1.9 GHz FSR) that we can compensate after assembling the cavity. This means that we had to fix the mirror holders and the whole assembly to the precision of a dozen microns in length (relative to $L = 7.757$ cm). Outside that compensation range, no efficient FC-cavity coupling can be achieved. The cavity was therefore assembled by continuously coupling the FC into it and monitoring the transmission, while making sure that tightening and fixing the parts does not change the cavity length. The cavity was assembled in air, outside the vacuum chamber, and the index of refraction of air had to be taken into account for the FC coupling. Due to index of refraction, FSR in the air is around 500 kHz different than in vacuum. This falls within the tolerance of the mismatch that can be compensated, but is still important to keep in mind for comb-cavity coupling.
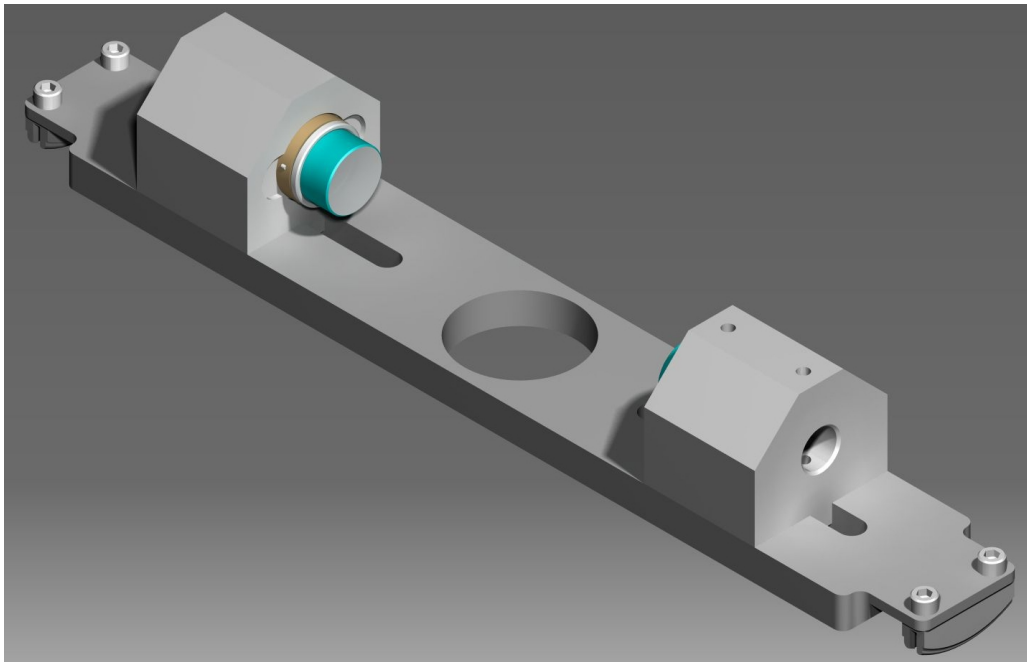
Figure 4.1: Design of the cavity assembly. Mirrors are glued to the holders using vacuum-compatible epoxy. One of the mirrors is mounted on a piezoelectric transducer ring, which allows scanning the cavity length. The mirror holders can slide along the main bridge and can be clamped to fix the cavity length. The central hole in the bridge allows unobstructed propagation of the MOT beams. The bridge is clamped to the grooves of the vacuum chamber at the viewports. The center of the cavity corresponds to the center of the vacuum chamber.

Probing the cavity mode structure. Before coupling the FC into the cavity, we first optimize the mode matching and alignment using a cw laser. As we scan the cavity length, we monitor the cavity transmission on a photodiode and on camera simultaneously. This is presented in Fig. 4.2 where we show the mode structure of our cavity, and identify the various modes we can excite in our geometry. We can clearly see the two highest peaks corresponding to the Gaussian modes, with FSR being the frequency distance between them. We used a photodiode with a slow response time, so the modes are broadened and wider than the natural linewidth, which allows us to visually identify them more easily. We can also see several higher-order modes, especially on camera (for the Gaussian mode the camera is highly saturated; the exposure was increased to make all the other modes visible). We see several Laguerre-Gaussian modes, which means our system exhibits a cylindrical symmetry. If we recall the discussion about alignment of optical cavities, this means that we've optimally aligned the laser beam axis to the cavity axis, but there's a mismatch in waist size or position. We also note two groups of modes, around the fundamental modes and halfway between them, which corresponds to the structure of a confocal cavity as shown in 2.7(c). Since our cavity is not perfectly confocal, there is some separation between the modes. The modes for which $(2p + l)$ is even are centered around the Gaussian modes, and $(2p + l)$ odd halfway between them. By choosing a better mode-matching lens, we eliminated the higher-order modes, leaving only the Gaussian mode in the following experiment.

4.1.2 Cavity stabilization and characterization

Pound-Drever-Hall technique. The most popular method of cavity stabilization is the Pound-Drever-Hall (PDH) technique [65]. The idea is modulate the frequency of the input laser light to create sidebands around the central frequency, and look at the light reflected off the cavity. The reflected light is collected on a photodiode and this signal is demodulated with the same frequency, but different phase compared to the modulation signal. This allows us to extract the dispersive signal around the cavity resonance, which serves as an error signal for locking electronics. Sidebands can be created by using an electro-optic modulator (EOM) to phase modulate the beam, or by applying the modulation directly to the laser diode current. The error obtained with the PDH technique is shown in Fig. 4.4(a) as an oscilloscope trace, together with the cavity transmission. Sidebands at the modulation frequency are also visible.

Cavity ring-down time. To measure the decay time of the cavity, τ, i.e. the linewidth the cavity mode, $\kappa = 1/\tau$, we stabilize the cavity and abruptly switch off the laser beam with an AOM, and monitor the exponential decay of the transmitted intensity on a photodiode. This is
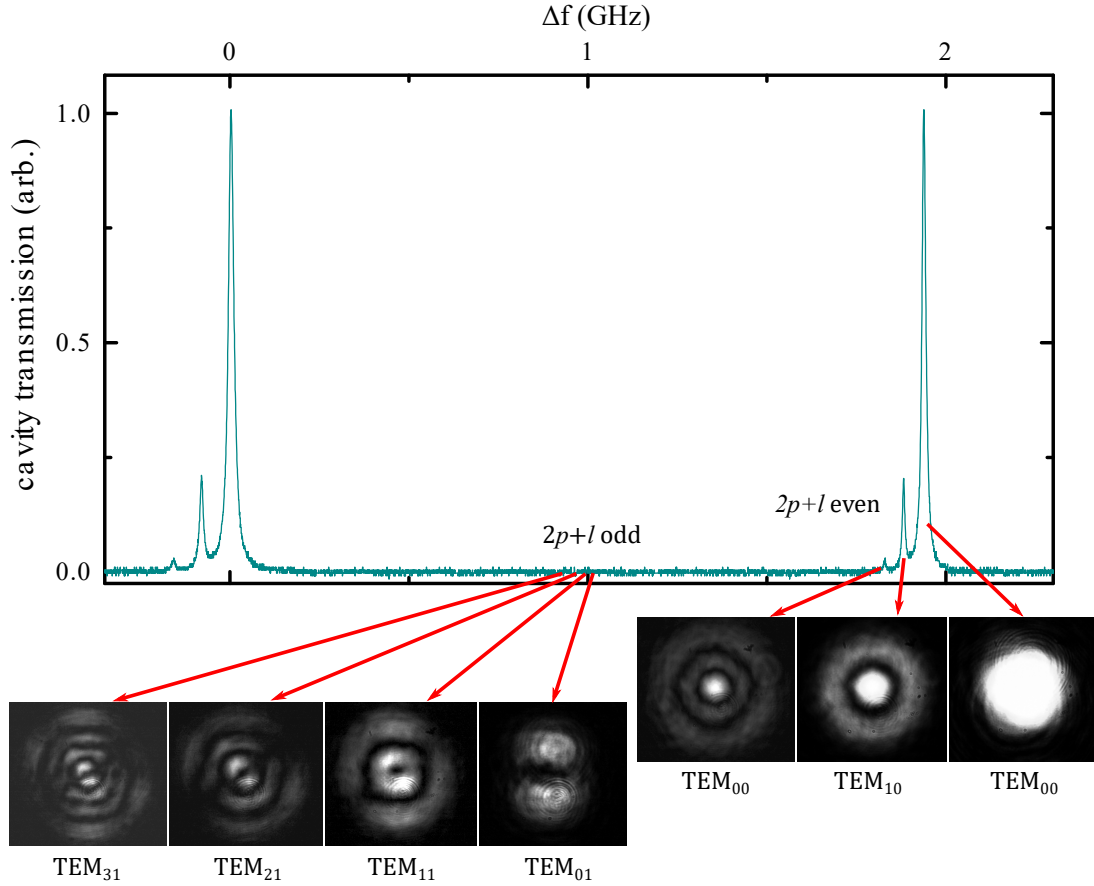
Figure 4.2: Cavity mode structure probed with a cw laser as we scan the cavity length. Light transmitted from the cavity is collected simultaneously on a photodiode and a camera. Higher order Laguerre-Gaussian modes are visible due to mismatch of waist size or position. The half-axial modes are visible on camera due to high exposure time of the camera. The relative power between different modes is seen on the photodiode signal. The modes are broadened compared to the 150 kHz linewidth due to slow response time of the used photodetector, which makes it easier to visually identify the peaks.

shown in Fig. 4.3, with an exponential decay function, $\exp(-t/\tau)$ fit to the data. We also show that the intensity drop due to AOM switching and the photodiode response is a lot faster than the cavity ring-down time, and does not influence the decay time measurement. This gives the linewidth of the cavity mode $\kappa = 2\pi\Delta\nu = 2\pi\cdot$ 150 kHz. Using Eqn. (2.40) we calculate the cavity finesse $\mathcal{F} \approx 12000$.

Stability. The width of the linear slope of the PDH error corresponds to κ, the linewidth of the cavity mode. Noise and fluctuations that fall within this frequency range can be fully covered by the error signal, while the cavity response to higher frequencies falls off. This means that the cavity behaves like a low-pass filter, with the cut-off frequency corresponding to the cavity
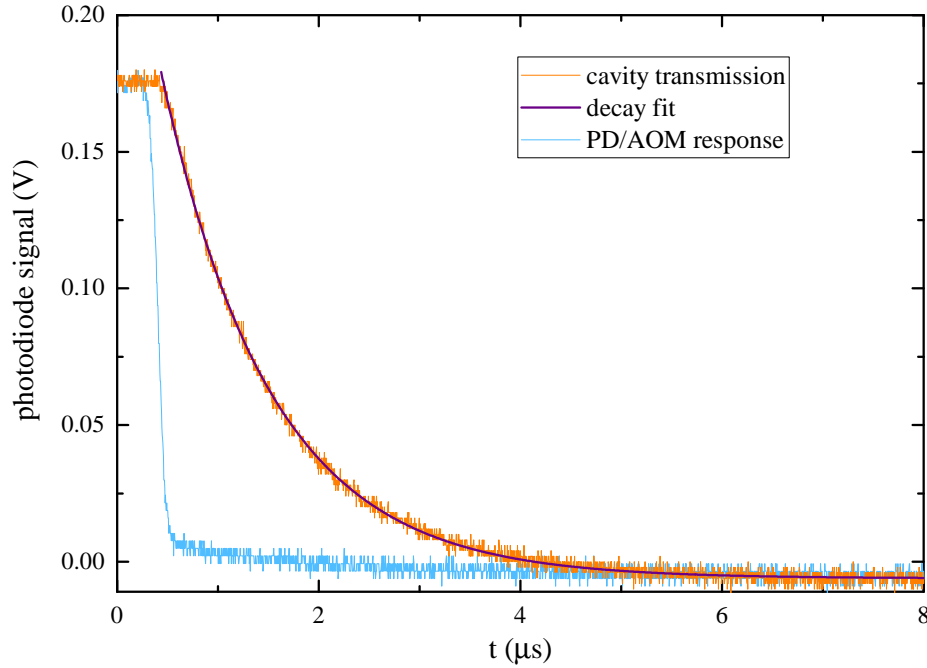
Figure 4.3: Cavity ring-down signal. Transmitted light decays exponentially (orange trace) when the input laser beam is abruptly switched off. The response of the AOM used to switch off the laser beam and the photodetector is also shown (blue trace) and is considerably faster than the cavity decay, so it does not influence the ring-down time measurement.

linewidth. For our cavity, the cut-off frequency is around 150 kHz and most acoustic and mechanical vibrations that need to be compensated are well within this range.

Fluctuations and noise change the cavity length, and with it the frequency of the modes. These include long-term temperature drifts as well as short term vibrations and noise. For high-finesse cavities with narrow modes, most of the time no light will be coupled into the cavity due to these fluctuations. It is therefore necessary to stabilize the cavity length and the frequency of the coupled laser in the experiment. To stabilize the cavity length, feedback can be applied to the piezo on one of the mirrors. It is necessary to know the transfer function (the response for different frequencies) of the piezo. As mentioned, the transfer function of the cavity with PDH error is a low-pass filter, and piezos behave like RLC circuits, meaning they have a resonance. This can be seen in 4.4(b), where we show the piezo response to the driving signal as a fuction of driving signal frequency. The piezo response can be measured by monitoring the cavity transmission. We apply a sine signal to the piezo, which scans the cavity length. We then measure the voltage needed for the scan to cover the main frequency and the sideband. Since we know the modulation frequency at which the sidebands occus, we can measure the response,

i.e. how much voltage is needed for a given frequency range. We then change the frequency of the driving sine signal and repeat the procedure. We see in 4.4(b) that the PZT response is flat until around 2 kHz, after which it falls off. A sharp peak occurs at 30 kHz, corresponding to the PZT resonance. To stabilize the PZT length, bandwidth of the locking electronics should not cover the resonance because a phase shift occurs on that frequency, so that noise is actually amplified instead of suppressed, making the locking loop unstable. We note here that the PZT ring itself has a resonance at higher frequencies, and the measured frequency is a consequence of our specific designed assembly and the weight of the mirror that pulls on the ring.
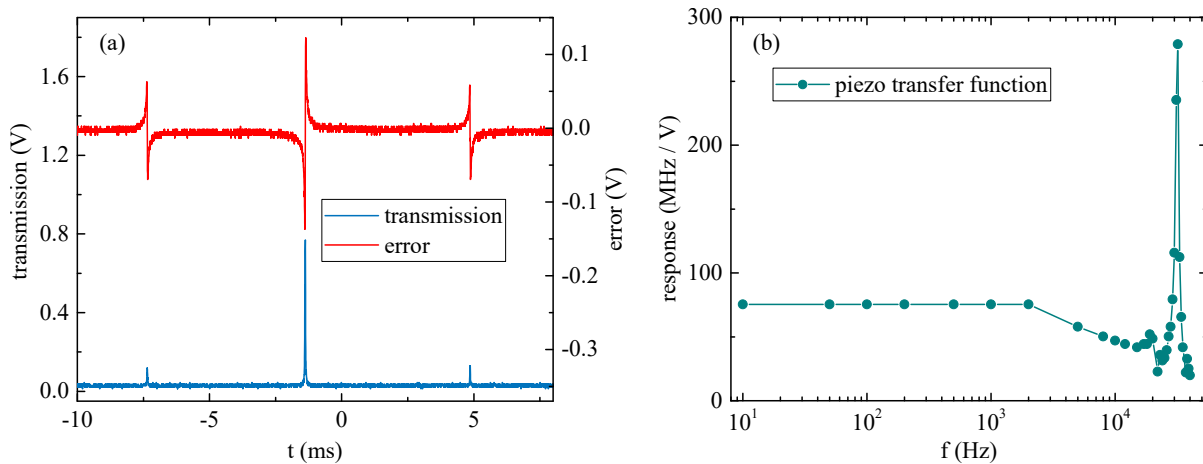
Figure 4.4: (a) Oscilloscope trace of light transmitted through the cavity (blue) and the PDH error signal (red) as we scan the frequency over the cavity resonance. The main peak corresponds to the Gaussian mode of the cavity, and sidebands are due to modulation of the laser frequency. (b) Transfer function of the PZT in the cavity assembly. The response starts falling off at 2 kHz, and a 30 kHz strong resonance is visible.

Feedback loop considerations.   The PDH error signal can be used either to stabilize the laser to the cavity, or the other way around. To lock the cavity length, the feedback signal is fed to the cavity piezo which, as we've shown, has a low bandwidth, up to a few kHz. Diode laser electronics usually has two feedback loops - a slow one for the laser resonator and the fast one for the diode current, covering a larger bandwidth. In our experiment, cavity length fluctuations due to vibrations were too large to tightly lock the cavity length to the diode laser by sending the correction to the PZT on the mirrors. This is more pronounced for a high-finesse cavity of a narrow mode linewidth, since even low amplitude vibrations can kick the cavity length more than the linewidth away. For this reason, we instead lock the laser to the cavity, using both feedback loops of the laser controller. The laser frequency is then stable compared to the cavity mode frequency, but together they can drift and fluctuate compared to some atomic frequency.

It is therefore necessary to also stabilize the cavity length, preferably using a wider (broader) error signal. With broader error signal, frequency kicks due to noise and vibrations will still keep the cavity frequency inside the linear slope of the error signal, allowing a more stable lock of cavity length. For this, we use saturation absorption spectroscopy (SAS) signal generated in a rubidium cell through which the probe laser propagates. SAS error signals are on the order of the Rb transition linewidth, ≈ 6 MHz, which is significantly wider than the cavity mode of 150 kHz. Using the SAS signals also allows us to precisely lock the cavity resonance compared to the rubidium transition. Different locking schemes will be presented in more detail for each experimental setup in the following sections.

4.2 Continuous wave laser pump

Even though the theoretical proposals for cavity cooling have been developed 20 years ago, the experimental realizations with ensembles of atoms are still scarce. Most of those experiments work in the transversal pumping geometry [8], and in the regime that's optimal for self-organization of a Bose-Einstein condensate (BEC) [10]. Only a few experiments investigated the collective coupling of a MOT cloud in a longitudinally pumped cavity. In [40] atoms were loaded in a deep far off-resonant trap in a Lamb-Dicke regime. Optomechanical cooling of the trapped ensemble was investigated by looking at the cavity transmission. Very recently, an experimental group demonstrated a trapping effect on a free MOT cloud as it interacts with the cavity light, also by looking at the cavity transmission [41].

To the best of our knowledge, no investigation of spatial distribution of atoms in a MOT in a longitudinal pumping geometry has been analysed and reported so far. In our experiment, we image the spatial and momentum distribution of atoms as they fall through the cavity. We recall the effects of a dipole force and the loading of atoms into the optical lattice, analysing the percentage and temperature of trapped atoms by looking at the time-of-flight images of the atomic cloud, i.e. by investigating the cloud dynamics instead of the cavity light dynamics.

A photograph of a ^{87}Rb MOT cloud loaded inside our optical cavity can be seen in Fig. 4.5. The two cavity mirrors are also visible.

4.2.1 Experimental setup

Preparation of a MOT cloud   Setup for the preparation of a cold ^{87}Rb cloud in a standard magneto-optical trap is similar to the one in the previously described experiment. Optical thickness is not a crucial parameter for collective cavity-enhanced effects, so absorption imaging is
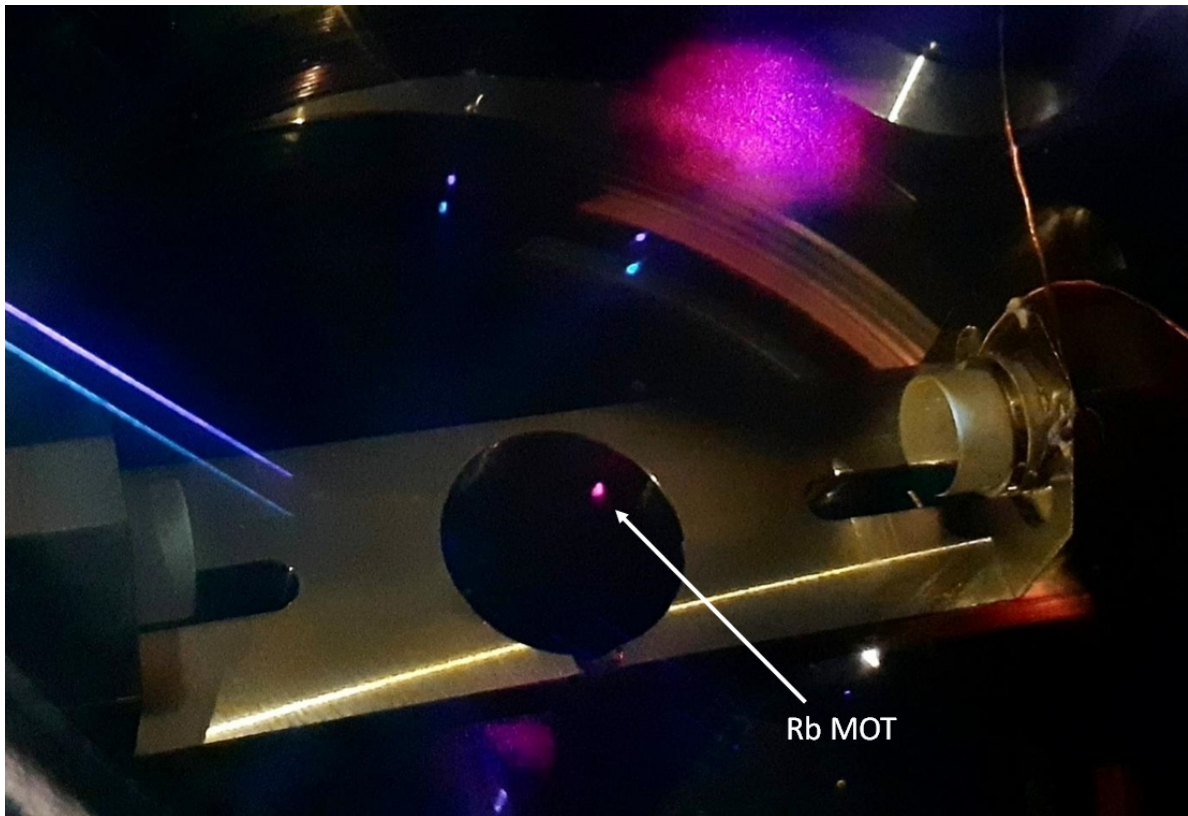
Figure 4.5: Photograph of the MOT chamber with a loaded ^{87}Rb cloud inside the optical cavity.

not needed and only fluorescence imaging is used to probe the cloud's time-of-flight dynamics. The cloud is prepared in a single loading stage (lasting up to a few seconds) and no dark MOT stages are used. However, a short cooling stage of 3-5 ms can be used after the loading stage to additionally cool or heat the loaded cloud. For this, we simply detune the cooling laser further away (closer to) from the atomic resonance, cooling (heating) the loaded cloud. This allows us to vary the temperature of the loaded cloud that interacts with the cavity light without changing the number of loaded atoms or the cloud size.

Locking the cavity   To stabilize the laser and the cavity, we use both rubidium isotopes and their relative transitions. The locking scheme for the optical cavity is shown in Fig. 4.6(a) and the used rubidium transitions used for stabilization of intracavity light are shown in 4.6(b) compared to the rest of ^{85}Rb and ^{87}Rb D2 line transitions. For reference, cooling and repumper laser are also shown. The cavity lock laser passes through a Rb spectroscopy vapour cell in the polarization spectroscopy (PS) setup. Since the MOT cloud is loaded from ^{87}Rb atoms, we want to lock the cavity resonance as far as possible from this isotope's resonances to minimize the resonant influence of the intra-cavity light on the atoms. For this, we use a vapour cell that
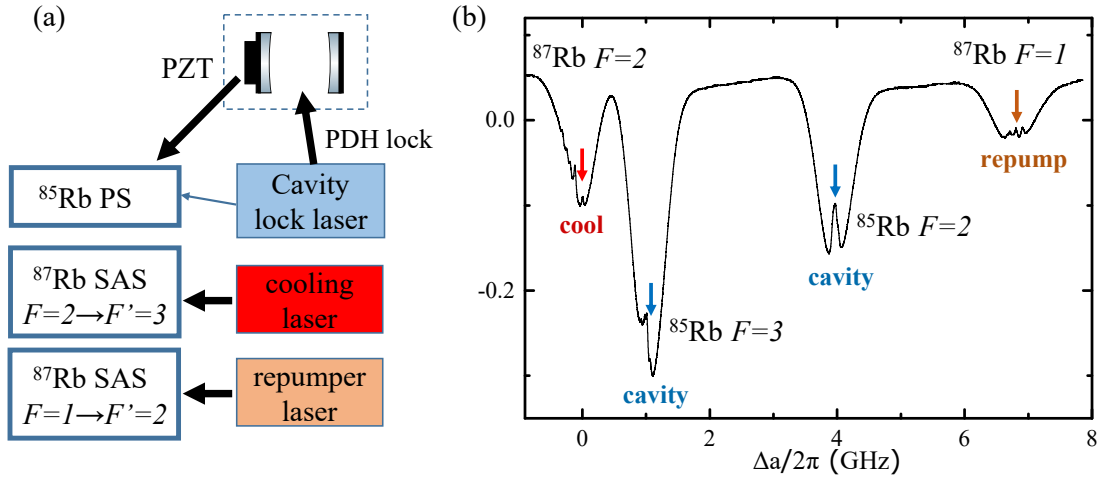
Figure 4.6: Locking scheme for different lasers (a) and their frequency values (b) compared to different D2 line transitions in ^{85}Rb and ^{87}Rb atoms. The spectral lines are measured by saturation absorption spectroscopy (SAS). PS - polarization spectroscopy, PDH - Pound-Drever-Hall, PZT - piezo transducer.

contains ^{85}Rb atoms and use its transitions as a reference for cavity lock. In a MOT, atoms are mostly in the $F = 2$ ground state, so we define the detuning of the cavity laser as compared to the ^{87}Rb $F = 2 \rightarrow F' = 3$ cooling transition frequency, $\Delta_a = 2\pi \cdot (\nu_L - \nu_{2\rightarrow 3}^{87})$. In Fig. 4.6(b) the relative frequency difference is shown between different transitions compared to the ^{87}Rb $F = 2 \rightarrow F' = 3$ cooling transition. By locking the cavity laser on ^{85}Rb $F = 3 \rightarrow F' = 4$ transition, we are detuned $\Delta_a \approx 2\pi \cdot 1$ GHz from the MOT cooling frequency. By locking on ^{85}Rb $F = 2 \rightarrow F' = 3$ transition, we are detuned $\Delta_a \approx 2\pi \cdot 4$ GHz. We first lock the laser to the cavity by feeding the PDH error signal back to the laser and acting on the laser diode current and piezo to stabilize the laser frequency. The laser and the cavity are locked together but drifting away from the spectroscopy resonance. We then feed the polarization spectroscopy error to the cavity piezo, stabilizing the cavity length to match the cavity resonance to the atomic resonance. This closed loop ensures that the lock laser is always on resonance with the cavity mode, $\Delta_c = 0$, and we set the laser detuning from the atomic resonance to either $\Delta_a = 1$ GHz or $\Delta_a = 4$ GHz. This means we are working with blue lattices in this experiment.

Measurement procedure   We start the measurement by loading the MOT cloud slightly above the cavity beam, shown in Fig. 4.7(a). This is achieved by changing the DC magnetic field and the trap centre with the compensation coils around the vacuum chamber. This way we ensure the cavity beam does not influence the loading dynamics and initial cloud parameters can be determined. The initial cloud radius is around 150 μm, while the cavity beam waist is around 100 μm, so only a fraction of atoms will significantly interact with the cavity potential. At $t = 0$

we turn off the MOT beams and let the cloud fall into the cavity beam due to gravity. During the fall time the cloud also expands at a rate determined by its temperature. It takes about 5 ms for the cloud to fall into the cavity waist, and we leave the cavity light on for additional 5 ms. At $t = 10$ ms we turn off the cavity light and leave the cloud to expand freely for a variable amount of time before we record the TOF signal on a camera by fluorescence imaging. We employ a sample and hold protocol during the TOF times not to lose the lock while the cavity beam is turned off. During the TOF time, we hold the locking control voltage at a constant, sampled value, for both the PDH and the SAS error signals. After the TOF time, we stop holding the control signals and the servos catch the error signal again. We can hold the signal up to 30 ms before the error signals drift too much for the servos to catch and lock them again. This way we can repeat the measurement cycles without having to re-lock the system. We then vary the intensity of the laser coupled into the cavity and thus change the depth of the cavity potential. Because we use a blue lattice, which is repulsive, there is no transverse spatial confinement of atoms and they fall through the cavity beam due to gravity. strong confinement is only achieved along the cavity axis.

4.2.2 Results and discussion

The measured TOF traces are shown in Figure 4.7(b) and (c). In 4.7(b) a spatial distribution of atoms along the cavity axis is shown in the left picture, which was acquired by summing the recorded 2D signal (in the right picture) along the vertical axis. The bimodal distribution of the cloud is visible in both 1D and 2D traces, and is a clear signature of the interaction of atoms with the cavity potential. The narrow Gaussian corresponds to atoms influenced or trapped by the cavity potential, while the wide Gaussian corresponds to the rest of the atoms. Because no true 3D trapping can be achieved in this blue lattice, we refer to trapping only as confinement along the cavity axis, in one direction. To quantify this bimodal distribution, we fit a double Gaussian function to the measured 1D data along the cavity axis. From the bimodal fit we can extract the number of atoms interacting with the cavity by looking at the ratio of the area of the narrow Gaussian and of the total distribution. During TOF the widths of both Gaussians evolve, which allows us to determine the temperature of trapped and untrapped atoms. These results are presented in Fig. 4.8 as a function of cavity lattice potential depth. The measurements were done for two initial cloud temperatures, 60 μK and 160 μK. The fractions of trapped atoms are shown for $t = 15$ ms and temperatures are calculated from measured Gaussian widths from TOF images: $\sigma^2(t_{TOF}) = \sigma_0^2 + \frac{k_B T}{m} t_{TOF}^2$. By using this expression, we assume that both Gaussians in the bimodal distribution expand freely and independent. We assume that the atoms contributing to the wide Gaussian distribution are those spatially outside the beam waist, or very
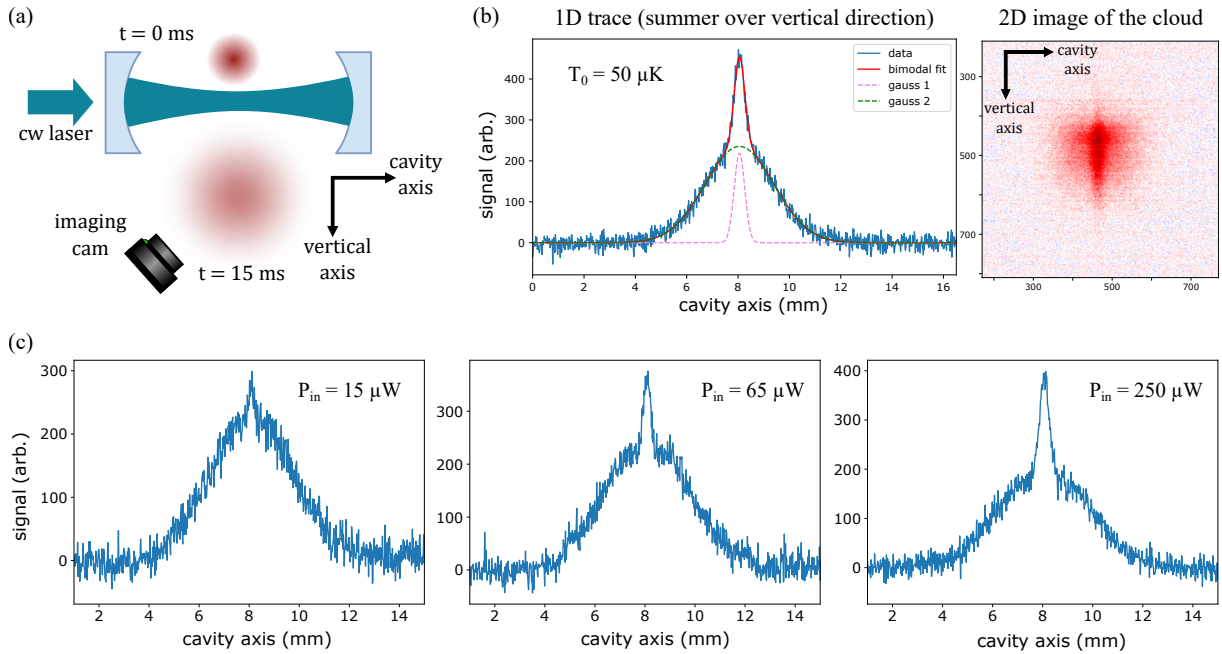
Figure 4.7: (a) A ^{87}Rb cloud is loaded above the cavity beam and at $t = 0$ MOT beams are turned off. The cloud falls into the cavity beam and interacts with it. We image the cloud again during TOF to record its spatial distribution. (b) Distribution of recorded atomic positions after interaction with the cavity beam, at $t = 15$ ms. The left picture shows a distribution along a cavity axis, which is extracted from a 2D image (on the right picture) captured by a camera during fluorescence imaging. The traces show a bimodal spatial distribution, and a fit of two Gaussian functions on the data is shown. The narrow Gaussian distribution corresponds to atoms influenced by the cavity potential, and the wide Gaussian to the rest of the initial cloud. (c) Distribution of positions along the cavity axis for different powers of the cavity beam, hence different cavity potential depths. For a deeper potential, a larger fraction of atoms is influenced by the cavity.

weakly interacting with the cavity potential. This means they've been expanding freely since the moment we turned the MOT beams off, at $t = 0$. So, for the wide distribution we take $t_{TOF,0} = 0$. The narrow distribution has clearly been influenced by the cavity potential and has started expanding freely only when we switched off the cavity beam at $t = 10$ ms; hence for the narrow Gaussian $t_{TOF,0} = 10$ ms. We see in 4.8 that the fraction of trapped atoms and both temperatures increase with the potential depth. A deeper trap can capture atoms with higher velocities, hence trapping a larger percentage of atoms from the loaded cloud. This means that the temperature of trapped atoms also increases, because the hotter atoms are trapped in the potential as well as the colder atoms, and the potential depth becomes more significant even in the Gaussian wings. Because the slower atoms are trapped in the potential, only the hot ones are left to expand freely in the wide Gaussian distribution, effectively increasing its temperature.

(a) $T_0 = 60$ μK

(b) $T_0 = 150$ μK
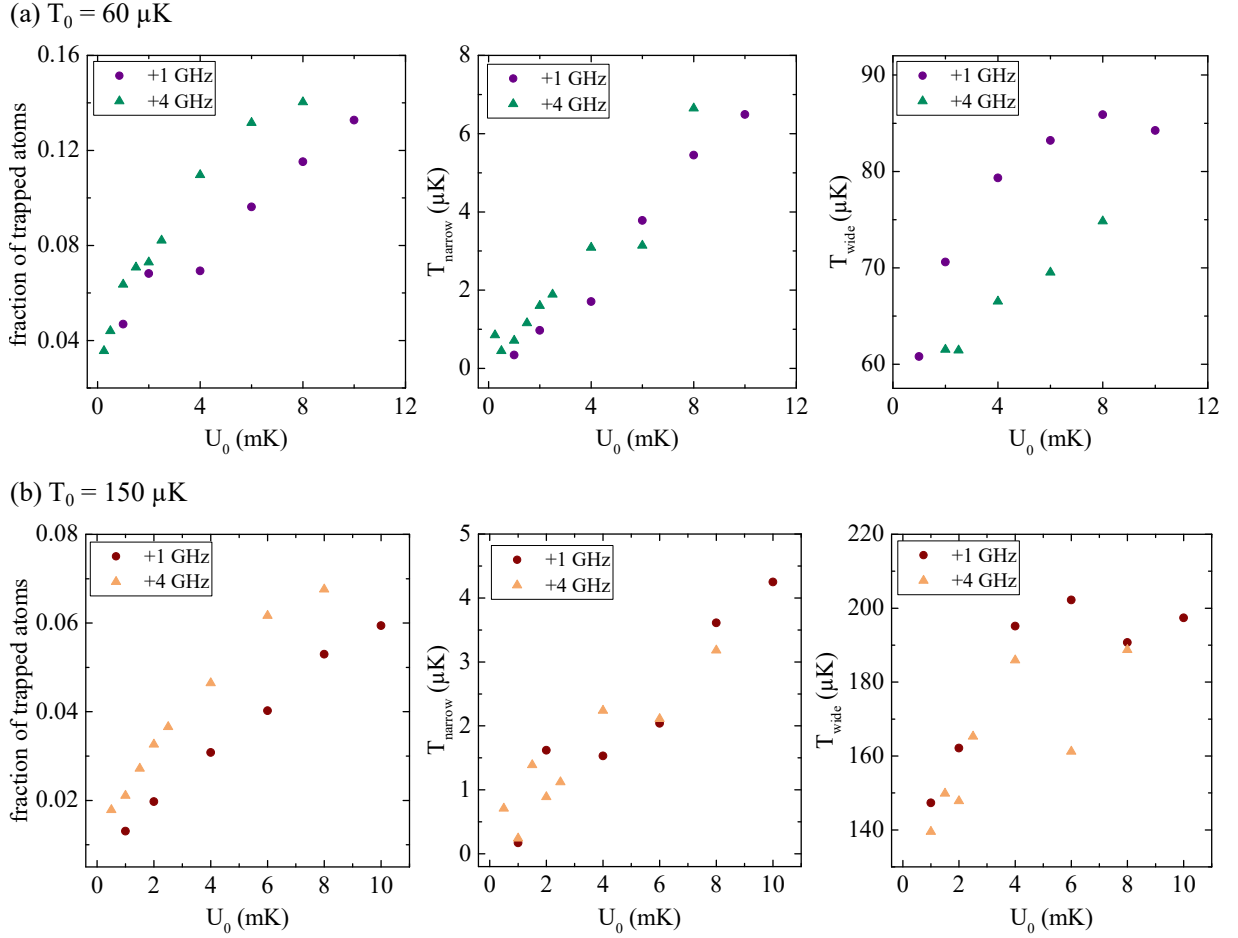
Figure 4.8: Time of flight measurements of the number of atoms trapped by the cavity potential and temperatures of Gaussian distributions in the bimodal shape of the cloud, as a function of cavity lattice potential depth. The number of atoms is shown for $t = 15$ ms and is expressed as a fraction of the area of a narrow Gaussian compared to the total distribution area. Data is shown for two atomic detunings Δ_a and for two initial cloud temperatures: (a) 60 μK and (b) 150 μK.)

For deeper potentials, only the very fast atoms are not trapped by the potential, which leads to the effective heating of the wide Gaussian distribution. We recall here that the initial RMS size of the loaded cloud in $t = 0$ is around 150 μm and the calculated beam waist is around 100 μm, so only a fraction of atoms geometrically cross the cavity potential. When the cloud is in the centre of the cavity waist, its size increases to ≈ 350 mum during TOF. The wide Gaussian distribution is then a combination of these unperturbed atoms that do not cross the cavity waist, and of those of high temperature that are not captured by the cavity potential. For this reason, for low potential depths we measure the temperature of the wide Gaussian to be the initial temperature of the loaded cloud. We note here that for our experimental parameters, the induced intra-cavity potential is very deep, on the mK range, because we're still working with

fairly near-detuned beams ($\Delta_a \sim$ GHz). This means we can achieve deep potential wells even with low power diode lasers, due to high cavity enhancement factor.

The bimodal distribution as seen in Fig. 4.7(b) and (c) can lead to a conclusion that there's been a transfer of momentum between two distributions, hence cooling of a fraction of atoms. This is because the spatial distribution in TOF images is a direct consequence of the momentum distribution. It would be intuitive to conclude that the momentum space also exhibits a bimodal distribution. This might not be true since we have to take into account that the wide Gaussian has been expanding freely since $t = 0$ and the narrow Gaussian since $t = 10$ ms. This means that the two spatial distributions could just have different expansion times since the narrow distribution was trapped during that time. Therefore, the spatial bimodal distribution does not give a straightforward answer about the momentum space. For this reason, we will look at simulations of loading of atoms in an optical lattice in the following section, where trajectories of atoms can be analysed as they move through the cavity potential.

We also compared the trapping of atoms in red and blue lattice conditions. As mentioned, we stabilize to the blue of the ^{87}Rb cooling transition by locking to ^{85}Rb transitions. On the red side there are no spectroscopy lines so we moved the laser and the cavity by hand to about $\Delta_a \approx -1$ GHz. The important distinction was that the red lattice potential influenced the MOT loading stage, even though the atoms were loaded above the cavity beam. This can be seen in Fig. 4.9. Because the red lattice is attractive and atoms move towards the intensity maxima, coupling with the field is strongly enhanced compared to a blue trap. This coupling induces a lightshift in atomic energy levels, which hinders the efficiency of MOT loading stage. For deeper potentials the lightshift is larger, and even less atoms can efficiently be loaded in a MOT [66].

Even though the red lattice influences the loading stage, when we let the cloud fall into the cavity waist, the effect is similar to the one we've seen for the blue trap. This is shown in Fig. 4.10 where we compared the TOF images and the spatial distribution of atoms for the same parameters, just changing the sign of the cavity potential. The bimodal distribution of similar shape is seen for both detuning of the cavity potential. This means that the effect of lattice trapping along the cavity axis is the same in both cases. However, red lattice should pull the atoms from the transverse direction into the cavity waist, which should increase the fraction of trapped atoms. Looking at Fig. 4.10, red lattice does seem to have a slightly more pronounced narrow Gaussian for the same experimental parameters, however this is well within the experimental error, so within the measurement certainty both red and blue cavity potentials give very similar results. This is to be expected since the potential gradient due to standing wave is larger than the gradient of the transverse Gaussian waist of the beam, so attraction/repulsion
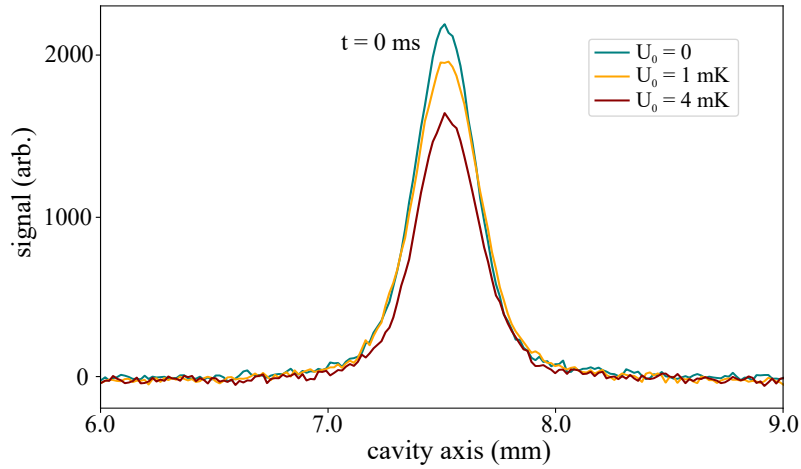
Figure 4.9: Time of flight image of the spatial distribution of a cold cloud right after the loading stage, at t=0. The cloud was loaded above a red-detuned cavity lattice, with the detuning of $\Delta_a \approx -1$ GHz from the ^{87}Rb cooling transition. The cavity potential influences the loading stage due to the induced lightshift in atomic energy levels, which is seen as a reduction of the loaded number of atoms.

from transverse direction is expected to be small compared to longitudinal trapping effects.

4.2.3   Simulation analysis of atoms loaded in optical lattices

To investigate the dynamics of atoms loaded in an optical lattice, we use numerical simulation that follow the time evolution of atomic trajectories. The original version of this Matlab code was developed by Raymon Watson and dr. John McFerran and very recently published [67]. I built upon their version of the code, upgrading it to include the analysis of atomic spatial and momentum distribution as measured during TOF imaging. Gravity is also included, as well as the vertical offset of the cloud, loaded above the cavity waist.

The code allows us to generate a cloud of atoms with a Gaussian spatial distribution with rms radius R. Every atom is randomly assigned a velocity according to the Maxwell-Boltzmann distribution for the set temperature. At t=0, atomic cloud is generated above a standing wave laser beam, into which it falls due to gravity as it freely expands - this way we simulate our exact experimental situation. We can use both red and blue lattices in the simulation by simply changing the sign of the optical potential, which includes the longitudinal standing wave dependence, as well as transversal Gaussian dependence due to the cavity beam waist. The beam waist can also be freely set as a simulation parameter, as well as the potential depth. Output of the simulation are atomic trajectories, giving (x, y, z) positions as well as (v_x, v_y, v_z) velocities for each atom for different evolution times. From these values we can look at the spatial and momentum distribution of atomic cloud by plotting histograms for these values.

a) red lattice

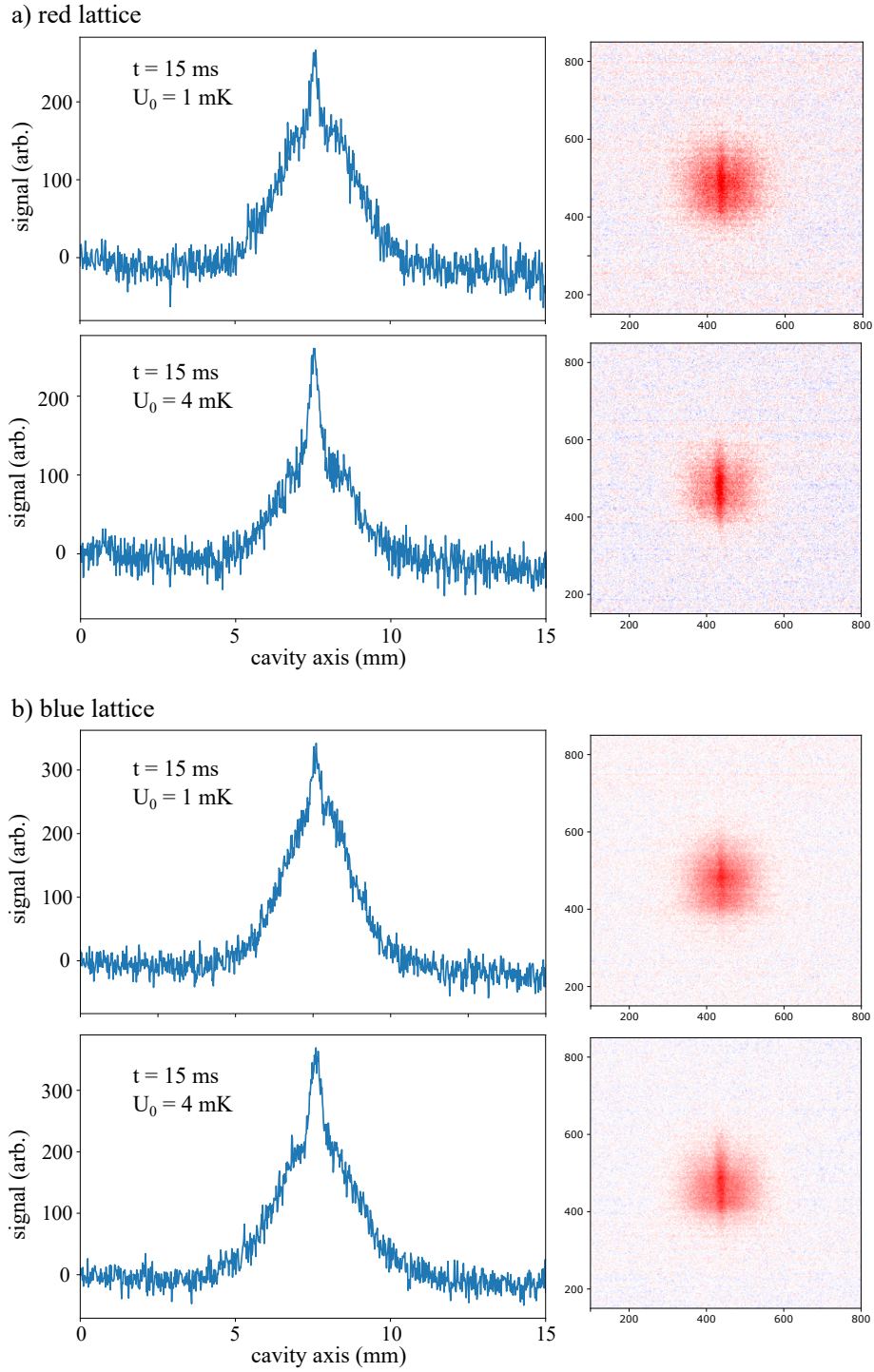b) blue lattice

Figure 4.10: Time of flight images of a cold cloud passing through (a) red and (b) blue cavity lattice potential at $t = 15$ ms, for two potential depths. The initial cloud temperature was 60 μK. In the case of (a) the red lattice, detuning from the ^{87}Rb cooling transition od $\Delta_a \approx -1$ GHz was used, while for (b) the blue lattice, $\Delta_a \approx +1$ was used.

To determine the temperature, we can use three approaches. The first one is the direct copy of the experimental procedure - imaging the spatial distribution during TOF, and fitting $\sigma^2(t_{TOF}) = \sigma_0^2 + \frac{k_B T_{tof}}{m} t_{TOF}^2$ to calculate the temperature. The second approach is directly looking at the momentum space. For a Maxwell-Boltzmann distribution, the width of the velocity distribution is determined with the temperature, $\exp(-mv^2/k_B T)$. By fitting a Gaussian to the momentum distribution and determining its width σ_{vel}, we get the temperature T_{width}:

$$T_{width} = \sigma_{vel}^2 m/k_B. \tag{4.1}$$

If the momentum distribution differs from the Maxwell-Boltzmann, the fit is not an accurate approach. The best and most general approach is determining the temperature from the average kinetic energy of the cloud. For a 1D approach (which is the case for movement along the cavity axis in a standing wave), $m < v^2 > /2 = k_B T_{avg}/2$. Hence, by averaging the velocity values for all atoms, we arrive at the temperature:

$$T_{avg} = \frac{m}{k_B} \frac{1}{N} \sum_i v_i^2 \tag{4.2}$$

We investigate different approaches to temperature determination because, to the best of our knowledge, no systematic study has so far been published about temperature measurements for atoms trapped in optical lattices. This is important for many experiments using optical lattices for many-body quantum simulation. In experiments, temperature is measured by TOF technique, but its validity is questionable if the initial momentum distribution is no more purely Gaussian. Likewise, heating of trapped atoms with increasing lattice depth is well known in the community, but it is not clear what this measured temperature is the signature of. It is therefore instructive to look at the full potential of atomic trajectories and investigate all properties of atoms trapped and untrapped by the optical lattice.

Simulation of the experimental regime   We first reproduce the experimentally observed bimodal distribution of atoms during TOF. The distribution of positions at $t = 15$ ms after the beginning of simulation and falling into the beam is shown in Fig. 4.11. We show the distribution of positions along the cavity axis (x-axis), and a 2D distribution along the cavity and vertical (gravity) axis, as imaged by the camera in the experiment. In Fig. 4.11(a) we show the results for a blue-detuned potential, and in Fig. 4.11(b) for a red-detuned potential. Except the sign of the interaction, the other parameters are the same. For computation, we used our experimental parameters for beam waist ($w_0 = 100$ μm), cloud radius ($R = 150$ μm), vertical displacement from the beam center $z_0 = 300$ μm and initial cloud temperature ($T_0 = 60$

μK). We used $N = 10^4$ atoms for the simulations of this chapter. The numerical results repro-

(a) blue potential
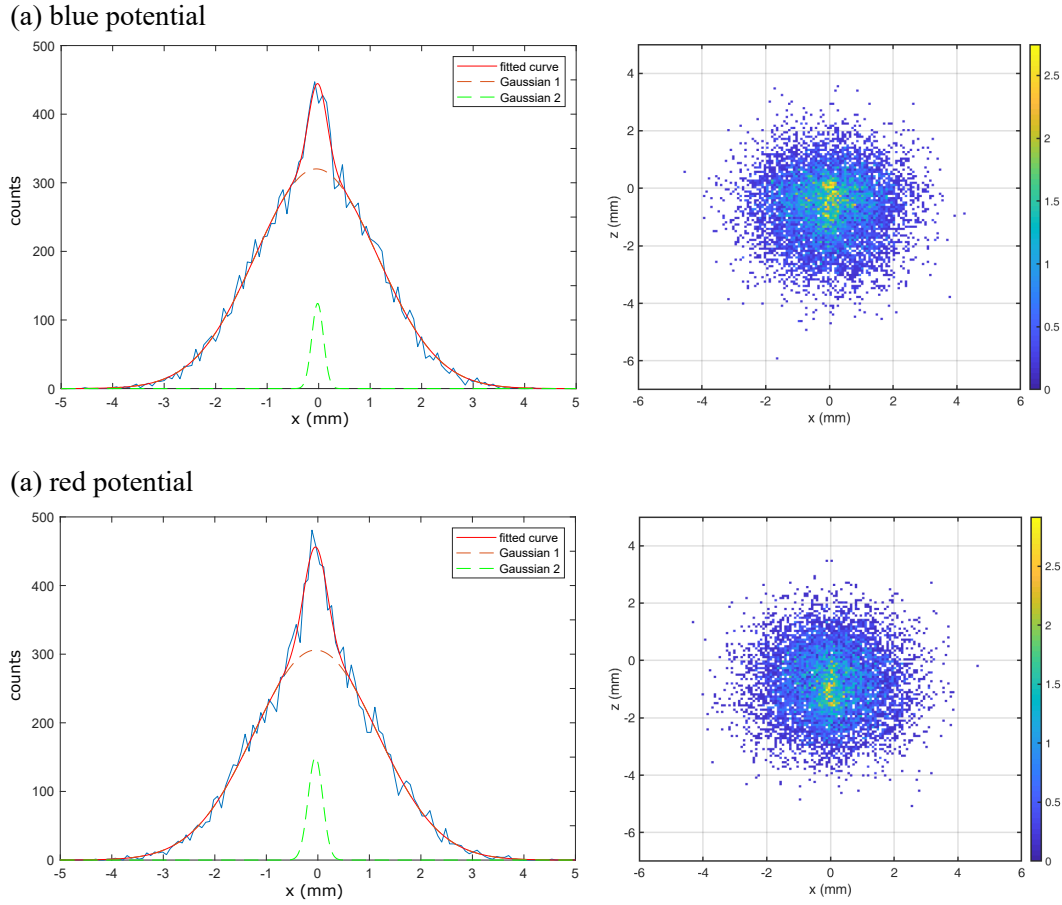
(a) red potential

Figure 4.11: Numerical simulation of the spatial distribution of atoms during TOF after interaction with a conservative lattice potential for (a) blue-detuned potential and (b) red-detuned potential. Left panels show a distribution along the cavity axis, while the right panels show 2D distribution along the cavity and vertical (gravity) axis. Distributions were taken at $t = 15$ ms TOF, with the potential depth $U_0 = 0.5$ mK. Other simulation parameters: beam waist $w_0 = 100~\mu$m, initial cloud radius $R = 150~\mu$m, vertical displacement from the beam center $z_0 = 300~\mu$m, initial cloud temperature $T_0 = 60~\mu$K, number of atoms $N = 10^4$.

duce the bimodal distribution and predict similar behaviour for red and blue lattices, which is in agreement with experimental data (see Fig. 4.10) . The potential used in these simulations is a conservative dipole potential, which means that any effects due to saturation and resonant scattering (which induce cooling/heating of atoms) are neglected. The emergence of a bimodal distribution measured in the experiment can be attributed to the conservative loading of atoms into the cavity potential, and dissipative mechanisms don't have to be included. The experimental data show no clear signature of complex cavity-induced collective dynamics. Because the locking laser is always locked to the cavity resonance, there is effectively no dispersive dy-

namics and no effects due to light-shifts can be measured. In our experimental regime, when the locking electronics is faster than the cavity-atom dynamics, this complex system effectively acts as a standing wave conservative potential.

There is some discrepancy between the measured and simulated distributions for deeper optical potentials. The results of Fig. 4.11 were acquired for $U_0 = 0.5$ mK, and the experimental results in Fig. 4.8 show that we achieve potential depths up to 10 mK. It is important to note that the values of experimental potential depths are estimated and calculated. These calculations take into account the power enhancement inside the cavity, which depends on several parameters, for example the intracavity losses and the quality of the locking of the laser to the cavity. Noise in frequency lock lowers the circulating optical power, and even induces heating of the trapped sample [32]. For this reason, a perfect matching of numerical and experimental parameters is not realistic, and only the qualitative behaviour is examined. Nevertheless, it is instructive to look at the main difference between the red and blue trap for large potential depths. In Fig. 4.12 we show the simulated 2D spatial distributions of atoms in the transverse directions (y, z) for a red and blue trap of depth $U_0 = 5$ mK. The blue trap is repulsive, see Fig. 2.3, and for strong

(a)   (b)
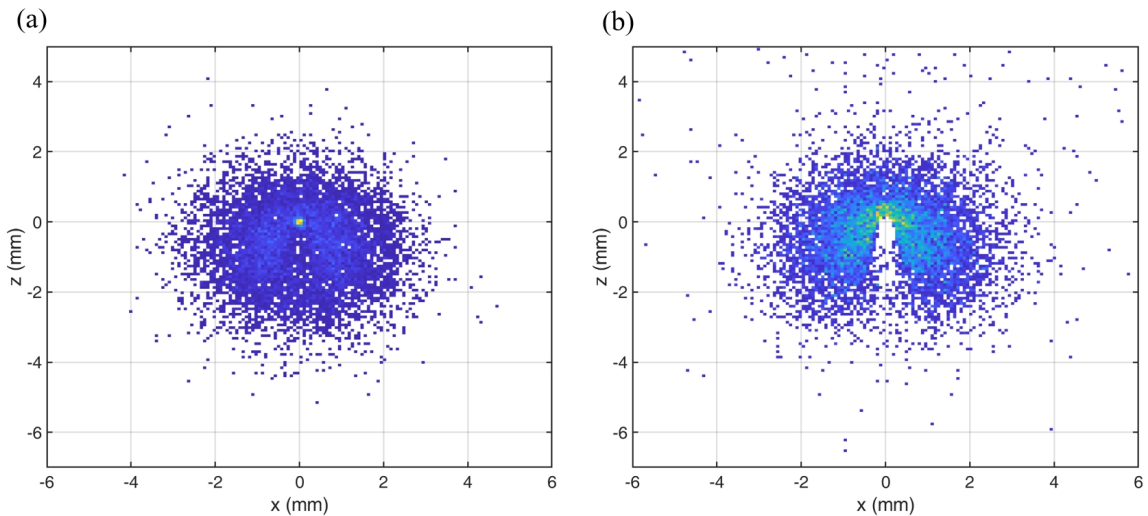
Figure 4.12: Numerical simulation of transverse (y, z) spatial distribution of atoms during TOF for (a) red and (b) blue detuned cavity potential. The parameters are the same as in Fig. 4.11, except for the potential depth $U_0 = 5$ mK.

potentials the atoms bounce off the transverse Gaussian potential and cannot even fall into the cavity trap. A red trap is attractive and the atoms are pulled into the waist. A consequence of the atoms "spilling over" the blue potential is that there is no bimodal distribution along the cavity axis, since most atoms do not fall into it. However, we do not see this effect of "spilling over" in our experiment, as we see a clear bimodal distribution for a blue potential as well. This

means that the effective experimental values of cavity build-up and potential depth are lower than calculated, as we've already discussed.

Influence of the lattice potential on the velocity distribution of atoms   Even though the dipole potential is conservative, some atoms can gain energy when they fall into the potential. The condition that the atoms remain trapped in the potential can be simply expressed - if the kinetic energy of the atom is smaller than the potential depth at the specific point in space where the atom enters the potential, i.e. $mv^2/2 < U(x, y, z)$, the atom will remain trapped in the potential. This expression gives a space-dependent capture velocity for the atoms to remain trapped. The closer the atom initially is to the edge of the potential, the less kinetic energy it needs to have to escape the well. However, if captured, the energy of the atom will increase almost by the potential depth, therefore increasing its average velocity and temperature. It is clear that the deep potentials will therefore spread the initial velocity distribution, however it is not as clear if the final distribution keeps a Gaussian shape or attains a different one.

We start by analysing only the influence of the longitudinal, standing wave potential by removing the transverse Gaussian profile and making the standing wave "pancakes" infinite in the (y, z) directions, as shown in Fig. 4.13(a). We also remove the influence of gravity, and the cloud is loaded in the center of the beam, so it expands symmetrically around the zero coordinates. In Fig. 4.13(b) we show a spatial distribution of a cloud during TOF for $t = 15$ ms in such an infinite standing wave potential, simulated for potential depth of $U_0 = 1$ mK. This means that all velocity groups in the generated cloud of $60\ \mu$K can be captured by the potential. Since the potential is deep, most atoms can only move along the pancake there were loaded in, like along the walls of a tunnel, and do not have enough energy to cross between the pancakes. Only some of the atoms have enough energy to climb the potential and get far away. The velocity distribution of such an atomic sample is shown in Fig. 4.13(c) where we show the initial Maxwell-Boltzmann distribution ($T = 60\ \mu$K) of the initial cloud, and a broadened and modified distribution due to interaction with the lattice potential. The modification of the distribution occurs quickly ($t = 5$ ms was chosen for plot) and has a constant shape for longer TOF times. The modification of the curve occurs on the time scale of the atoms falling into the lattice potential.

We look into the velocity distribution in more detail in Fig. 4.14, where we compare the temperatures acquired by fitting Gaussian curves and by calculating the average kinetic energy. Strong heating along the standing wave direction is visible, with final temperatures of around $400\ \mu$K being far higher than the initial $60\ \mu$K. Distribution slightly deviates from the Gaussian shape, as seen compared to the Gaussian fit in Fig. 4.14(a), however it is still a very good
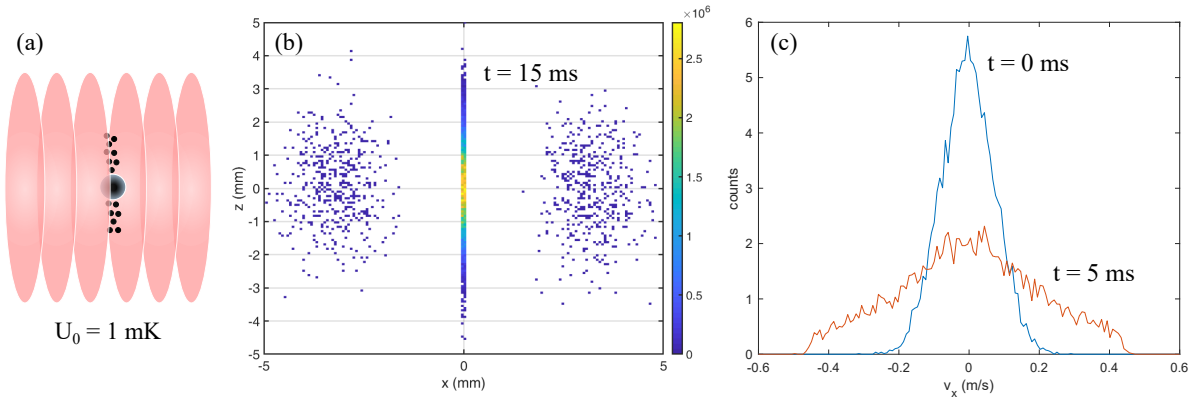
Figure 4.13: a) Standing wave "pancakes" of infinite transverse size used to simulate a pure 1D cavity potential with no influence of transverse directions. For a deep potential, the atoms can only move along the pancake they were loaded in, like along the walls of a tunnel. (b) Spatial density distribution during TOF in an infinite standing wave pancake. Only some of the atoms have enough energy to climb the potential, most atoms are confined. c) Velocity distribution along the cavity axis at $t = 0$ (when the cloud is generated), shown with a blue curve, and at $t = 5$ ms, after falling into the cavity potential, shown with an orange curve. The initial shape corresponds to a Maxwell-Boltzmann distribution ($T = 60 \ \mu$K). Heating of the cloud and a modification of the velocity distribution due to standing wave potential is clearly visible.
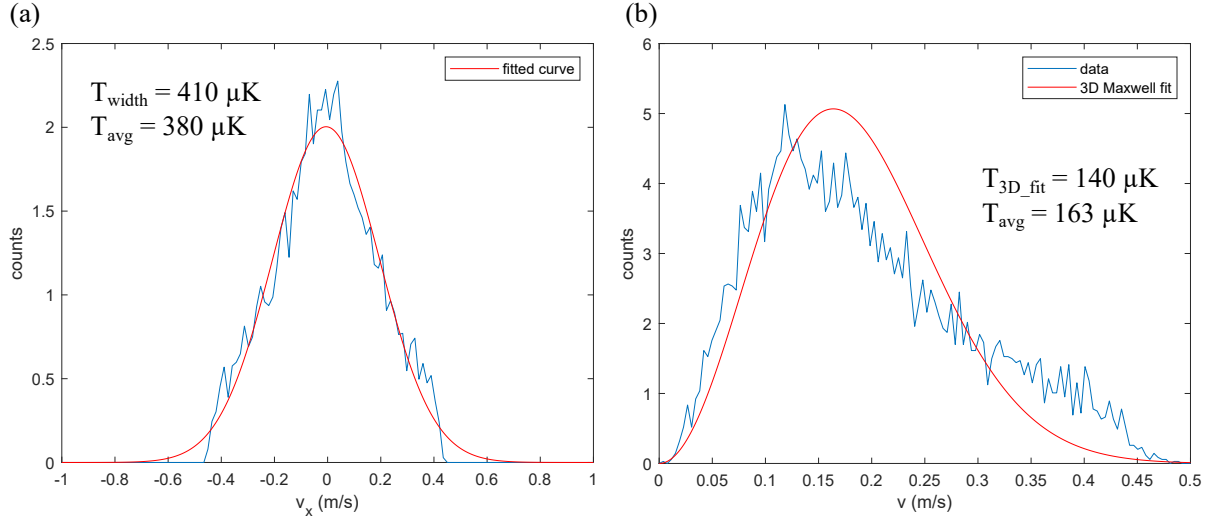
Figure 4.14: a) Velocity distribution along the cavity axis and b) speed distribution (3D M-B) during TOF, at $t = 5$ ms, corresponding to the simulation in Fig. 4.13. In a) a single Gaussian fit is shown, from which we calculate the temperature, while in b) we fit the 3D M-B distribution with the temperature as the only free parameter. Temperatures calculated through mean kinetic energy for a) 1D and b) 3D case are also listed.

approximation, and the temperature acquired from the width of the Gaussian is in very good agreement with the temperature calculated through the mean kinetic energy. In Fig. 4.14(b) a speed (3D Maxwell-Boltzmann) distribution is shown, with the corresponding temperature as the only free parameter. The deviation from the speed distribution is only due to heating and modification along the longitudinal axis, since transverse velocities and temperature are unperturbed by the standing wave. Despite the deviation from the speed distribution, the fitted temperature is in good agreement with the temperature corresponding to mean (3D) kinetic energy. Therefore, even though there is heating along the cavity axis and the distribution does not remain a pure Gaussian, it is still a very good approximation. For shallower potentials, heating and deviation from a Gaussian are even less pronounced. Experimentally, generating a potential of 1 mK depth is not easy, so it is justified to assume a Gaussian distribution of atoms trapped in optical lattices.

Let us also look at the atoms that had enough energy to climb and cross the lattice potential, as was seen in the spatial distribution of atoms in Fig. 4.13(a). If we look into the velocity distribution along the cavity axis for these "free" atoms, which is presented in Fig. 4.15(a), we see that these atoms have even higher energy and there are no atoms with very small velocities among them. This is logical because the very slow atoms are either trapped in the "pancakes"

(a)   (b)
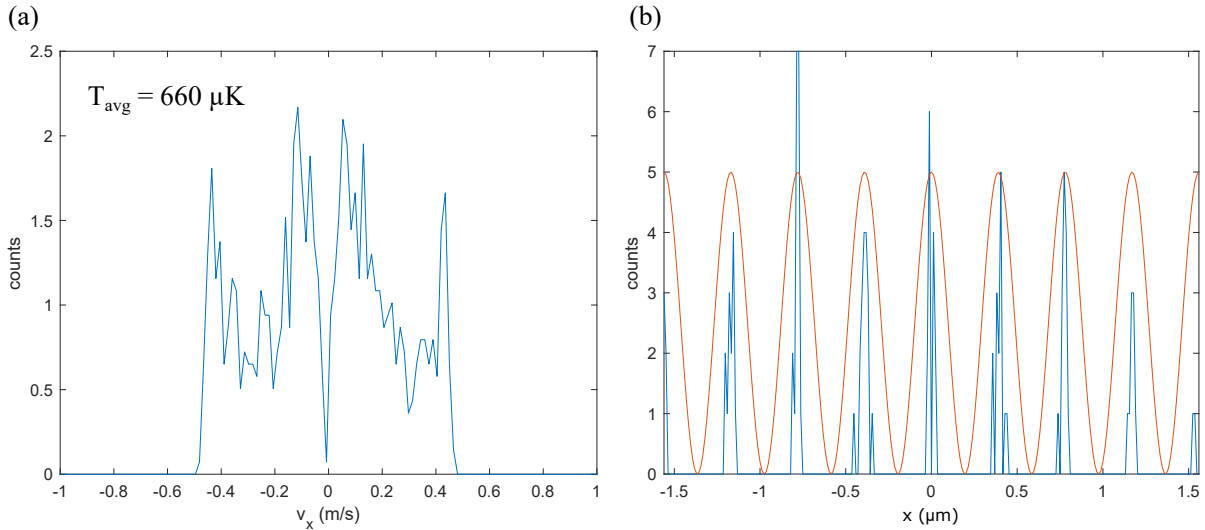
Figure 4.15: a) Velocity distribution of atoms moving freely along the cavity axis during TOF, at $t = 15$ ms. b) Initial spatial distibution, at $t = 0$, of atoms that can move freely along the potential. The lattice potential is also shown as a reference (orange curve). These atoms were loaded on top of the standing wave, so they gain the most energy, but can also move freely through the standing wave.

or moving extremely slowly over the potential, during longer TOF times. For a velocity distribution such as this, the average kinetic energy is the only suitable method of calculating the

temperature the atoms. It is also interesting to look at the "history" of these "free" atoms - what was their position in regard to the cavity potential so that they managed to escape it. The initial spatial distribution of these atoms is plotted for $t = 0$ in Fig. 4.15(b), together with the spatial dependence of the lattice potential. It is clear that these atoms were loaded on the top of the potential, which is why they can climb over the "pancakes" and stay "free". These atoms are also the hottest since the full potential depth was added to their energy as they fall down into it.

Conclusion.   We measured a bimodal spatial distribution of atoms during TOF as a consequence of interaction of atoms inside the cavity with a cw laser in longitudinal pumping geometry. The narrow peak of the distribution corresponds to the fraction of atoms trapped in an intra-cavity standing wave potential as the cloud expands and falls through the laser beam due to gravity. We can capture up to 20% of atoms from the loaded cloud into the narrow peak, with temperatures less than 10 μK, which is significantly below the initial cloud temperatures of either 60 μK or 150 μK. We showed that the fraction of trapped atoms and their temperature increases with the potential depth, since more atoms from the initially loaded cloud can be captured.

We compared the TOF images for red and blue detuned standing wave potentials, while leaving the other experimental parameters unchanged. We measured the same bimodal distribution in both regimes, concluding that the effect of the standing wave trap is the dominant one and the same regardless of the atomic detuning. The red traps, however, influence the MOT loading stage due to their attractive interaction, which results in a lower number of atoms in a MOT after the loading. The blue trap showed no influence on the loading of the cloud.

Finally, we numerically simulated loading of atoms in a conservative standing wave potential. Using our experimental parameters, we reproduced the bimodal distribution for both red and blue traps, as measured in the experiment. This means that for our experimental regime, the results can be explained as a consequence of interaction of atoms with a conservative standing wave potential, and collective cavity-enhanced effects are not necessary. Additionally, we show that for deep optical lattices, the momentum distribution of atoms along the lattice axis does not retain its initial Maxwell-Boltzmann distribution, but is broadened and modified. This is a consequence of atoms gaining energy as they fall into the optical lattice and strong heating can be observed along the lattice axis. Due to this longitudinal heating, the speed distribution also deviates from the 3D M-B distribution. However, even though the new momentum distributions deviate from the M-B shape, the M-B distribution still gives a very good estimate for the temperature of atoms. The deviation from M-B distribution becomes significant only for very large potential depths ($U_0 \approx 1$ mK), which is usually above the typical experimental values.

Therefore, for most experiments, assuming a Gaussian M-B distribution of atomic velocities is a very good estimate for the temperature measurements.

4.3 Frequency comb laser pump

In the second part of this experiment, we replace the cw cavity beam with the frequency comb. This, however was not as straightforward from the experimental point of view, because the cavity still needs to be stabilized. As seen in the previous chapters, the coupled 780 nm laser interacts strongly with the atomic cloud, and it would be hard to distinguish between cw- and FC-induced cavity effects. Likewise, even for very low powers, the cw laser is still much stronger than a single FC mode, so effectively the intracavity potential would still be dominated by the cw standing wave. For this reason, we introduced a locking laser that operates at Cesium cooling frequencies around 852 nm, instead of the 780 nm light used for Rubidium. This way, the cavity can be stabilized to the Cesium laser which is far off-resonance for the Rubidium atoms, and has no measurable effect on the cloud for low optical powers. Any detected interaction can therefore be assigned solely to FC light.

4.3.1 FC-cavity coupling

We coupled the FC into the cavity by propagating it through the same PM fiber as for the cw locking beam. This way we ensure the optimal overlap and mode-matching. To find the matching between FSR and f_{rep}, we scan the cavity length while also manually changing f_{rep} until cavity transmission can be observed on an oscilloscope. This can be seen in Fig. 4.16, where an "envelope of coupling efficiency" can be on the transmission amplitude, as described in the theoretical section (see Fig. 2.12). The transmission peaks occur every f_{rep}, which is around 80.5 MHz. A zoomed in, smaller scan of FC transmission is shown in Fig. 4.16. There are two interesting features visible. The first one is a "tail" on one side of the transmission peaks that are otherwise expected to be symmetric. The second one is the large width of the envelope of coupling efficiency, so it is hard to tell which transmission peak is the optimal, i.e. when we perfectly matched FSR and f_{rep}. This is a consequence of high dispersion of cavity mirrors.

We analyse the cavity dispersion by looking at the FC spectrum transmitted through the cavity. The full FC spectrum is shown in Fig. (4.17). The peak of the spectrum is at 780 nm, and it covers (although weakly) wavelengths from 775 nm to 785 nm. If the mirrors had no dispersion, we could simultaneously couple this whole spectrum into the cavity. Due to dispersion and the walk-off of the cavity modes, only a part of the spectrum is coupled, depending on the
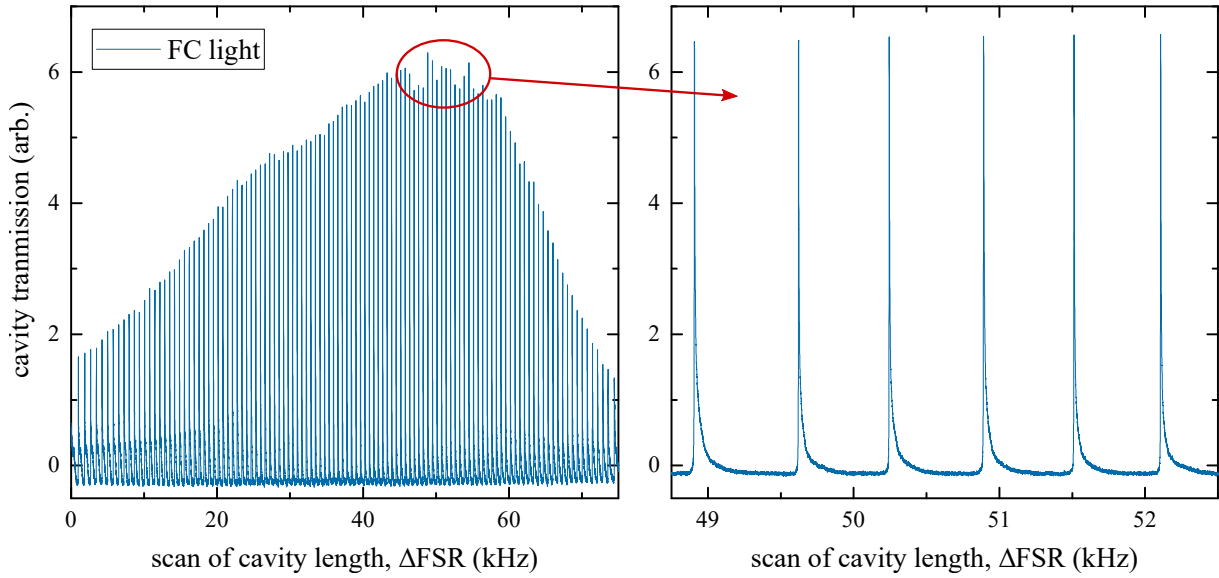
Figure 4.16: Transmission of the FC through the cavity as we scan the cavity length. Transmission peaks occur every f_{rep}, which is around 80.5 MHz. The envelope of the coupling efficiency is seen on the transmission amplitude, as a consequence of mismatched FSR and f_{rep} values. A zoomed in signal exhibits asymmetric transmission peaks, a consequence of high dispersion of cavity mirrors.
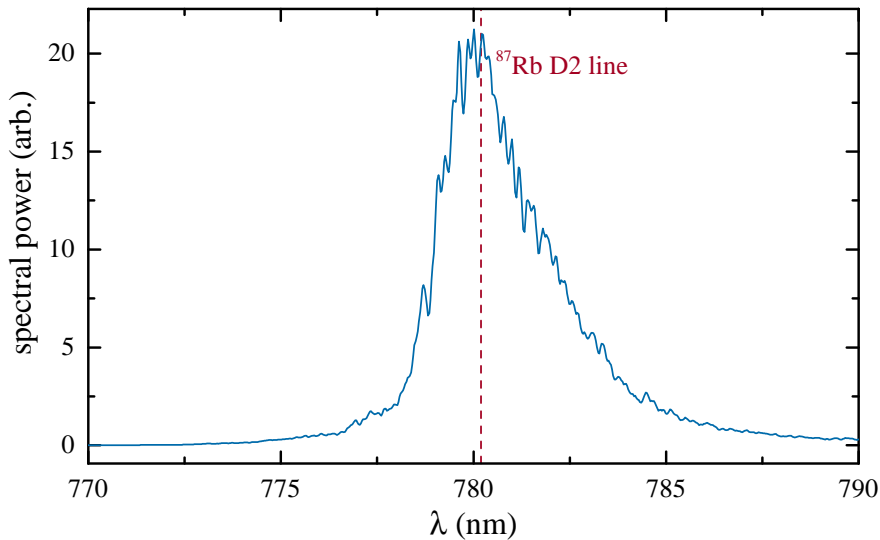
Figure 4.17: Spectrum of the frequency comb before coupling into the optical cavity.

local matching of FSR and f_{rep} around the optimal value of that wavelength. To look into that, we match FSR and f_{rep} around a chosen specific transmission peak (Fig. 4.16) and stabilize both the cavity and frequency comb independently to keep the FC-cavity coupling and the FC transmission stable in time. Locking details are presented in more detail in the next section. For

a stable coupling, transmission signal can be monitored on an optical spectrum analyser (OSA) which measures the transmitted (i.e. coupled) FC spectrum. We can change the value of f_0 for the FC with an AOM, which means we can shift the whole FC spectrum around the cavity modes. By changing f_0 we are effectively scanning over the single transmission peak, see Fig. 4.18(a). This way we can monitor which part of the spectrum is coupled on the top of the peak, and which on the slowly-falling tail. The values of f_0 for a given point on the transmission curve as labelled with (i)-(iv) in Fig. 4.18(a) and their values are givin in the legend of Fig. 4.18(b), where the transmitted spectrum is presented for each of the values, i.e. for different points of the transmission peak. The point of maximum value is set to $\Delta f_0^{FC} = 0$. An interesting behaviour
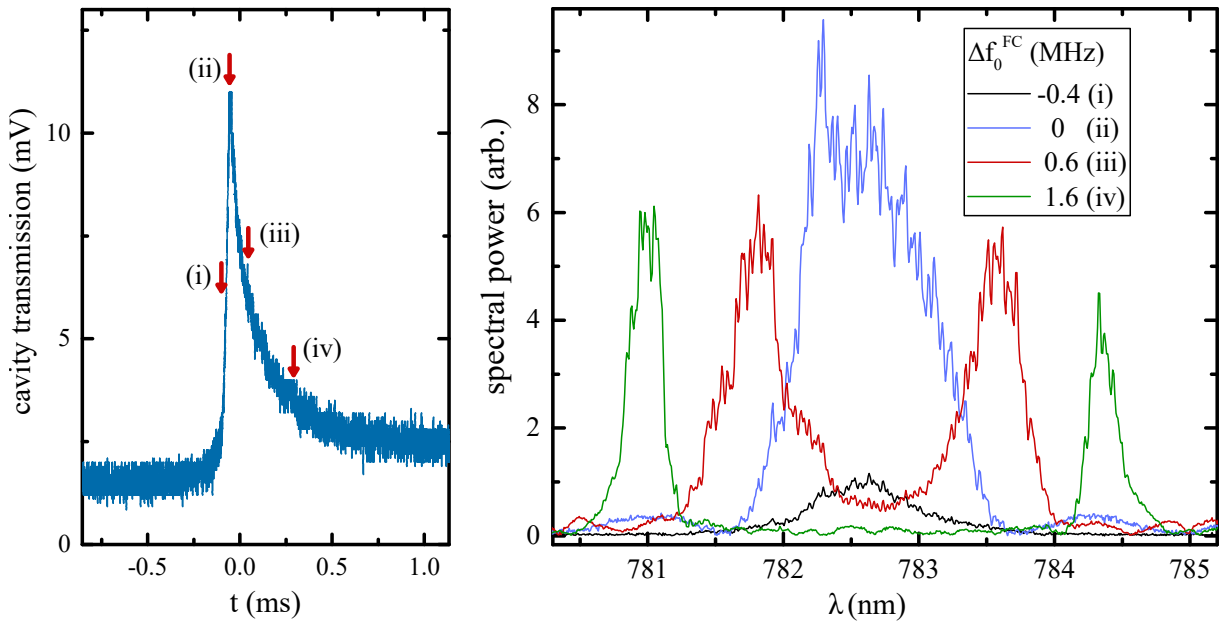
Figure 4.18: (a) Single FC transmission peak as we scan over the cavity resonance. When the cavity and FC are stabilized, we scan over this transmission curve by changing f_0 of FC with an AOM. Different transmission values correspond to different values of Δf_0^{FC}, with $\Delta f_0^{FC} = 0$ corresponding to the maximum value of the transmission peak (labelled (ii)). (b) Spectrum of the transmitted FC light for different points (i)-(iv) of the transmission peak. The values of Δf_0^{FC} for these points are given in the legend.

is seen for the transmitted spectrum. While on the steep side of the single transmission peak, the spectrum consists of a single bump that increases in amplitude as we move from point (i) towards (ii). After that, the bump splits into two parts that move away symmetrically from the centrally coupled wavelength as we move from (ii) towards (iv). It should also be noted that the centrally coupled wavelength is around 782.5 nm, and the center of the FC is around 780 nm. The spectrum around 782.5 nm is also much narrower than the original FC spectrum. This

is due to the chosen single transmission peak in Fig. 4.18(a). For another transmission peak under the wide coupling envelope (Fig. 4.16), we would locally match f_{rep} and FSR around some other wavelength. The splitting of the spectrum would behave the same as shown in Fig. 4.18(b), just for another centrally coupled wavelength.

To understand why the spectrum splits symmetrically, we assume the cavity dispersion such that the cavity FSR constantly increases with frequency. We assume a linear increase of Δ, so that the distance between each consecutive two cavity modes is bigger for the value Δ. This idea is presented in Fig. 4.19(a). We can optimally couple the FC into the cavity around a certain wavelength, for which the optimal FSR is labelled FSR_0. That part of the spectrum is then maximally transmitted. By scanning Δf_0^{FC} we move away from the originally coupled spectrum, however we couple FC modes into the cavity modes on other wavelengths, that were further away due to dispersion, symetrically around the central value. If we can measure the wavelength of the spectrum that gets transmitted as we scan Δf_0^{FC}, we can determine the dispersion value Δ. This is presented in Fig. 4.19(b) and (c). In 4.19(b) for a set value of Δf_0^{FC} the spectrum is split into two peaks whole wavelength we can directly measure. Along with the central spectrum, two sidebands can be seen around 790 nm and 770 nm. The sidebands occur when the cavity modes are shifted due to dispersion by a whole f_{rep}, so that the matching condition is again achieved. The sidebands hence behave like the central peak and the split as we scan Δf_0^{FC}. The measured wavelength values as a function of Δf_0^{FC} are shown in 4.19(c) and can be directly mapped to the behavior of 4.19(b) and 4.18(b). For small values of Δf_0^{FC} there is a single peak which increases in amplitude, then splits into two peaks.

To determine the dispersion term Δ, we look at the condition of FC and cavity matching around a specific central frequency f_c by finding the local optimal value FSR_0. The frequency of the comb mode will be matched with the cavity frequency, $f_c^{FC} = f_c^{cav}$, while n modes away, frequency of the FC mode is $f_n^{FC} = f_c^{FC} + nFSR_0$ and of the cavity mode $f_n^{cav} = f_c^{cav} + nFSR_0 + n(n+1)\Delta/2$. The term $n(n+1)\Delta/2$ is the arithmetic series that comes from summing the frequency shift for each cavity mode up to the n-th mode ($\Delta + 2\Delta + ... + n\Delta$). The n-th FC mode is matched with the n-th cavity mode when we shift the FC spectrum by Δf_0^{FC}. The matching condition is therefore $f_n^{FC} + \Delta f_0^{FC} = f_n^{cav}$, or:

$$\Delta f_0^{FC} = \frac{n(n+1)}{2}\Delta. \tag{4.3}$$

This equation shows that the modes further away walk off faster (with n^2), which is in agreement with the parabolic curve in Fig. 4.19(c). To determine n we calculate the number of cavity modes spaced by FSR_0 from the centrally coupled wavelength for $\Delta f = 0$ and for peaks for
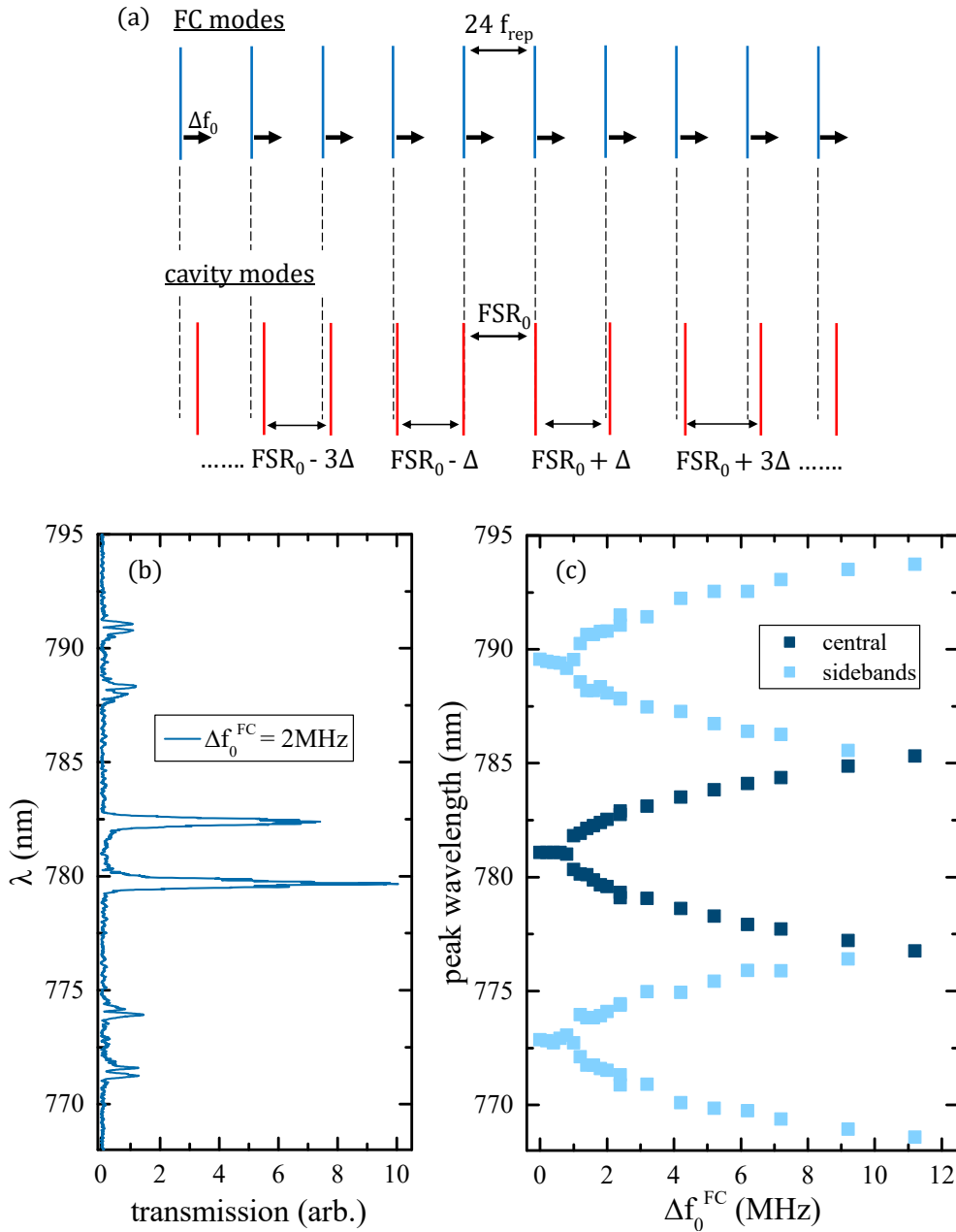
Figure 4.19: (a) Due to cavity dispersion, FSR around a specific wavelength increases by a value Δ with frequency. Optimum matching is locally achieved for a value labelled FSR_0. As we scan Δf_0^{FC}, the central wavelength is decoupled, but FC modes at different frequencies sit into the cavity modes, symmetrically on both sides of the central frequency. (b) For a specific value Δf_0^{FC} the transmitted wavelengths can be measured by reading the value on the peaks. Beside the central spectrum, two sidebands appear which occur when the shift due to dispersion equals f_{rep}, so the matching condition is achieved again. (c)Wavelength of the transmitted spectrum as a function of Δf_0^{FC} for the central peaks and the sidebands.

other Δf_0^{FC}. By fitting a second order polynomial to equation (4.3) using the measured data from Fig.4.19(c), we get $\Delta = (18 \pm 2)$ Hz.

An alternative approach to determine the dispersion term is by using Eq. (2.57). Dispersion term is small compared to the value $FSR_0 = c/2L$ so we can expand the expression:

$$FSR(\omega) = \frac{c}{2L + c\frac{\partial \phi}{\partial \omega}|_{\omega_0}} \approx FSR_0 \left(1 - FSR_0 \frac{\partial \phi}{\partial \omega}|_{\omega_0}\right) \tag{4.4}$$

A frequency dependent phase can be expanded up to the second order $\phi(\omega) = \phi_0 + \phi_1 \omega + \phi_2 \omega^2$, so the dispersion term is $\partial \phi / \partial \omega = \phi_1 + 2\phi_2 \omega$. The dispersion term Δ was defined as a difference between two neighbouring values of FSR, so $\Delta FSR = FSR(\omega_2) - FSR(\omega_1) = -FSR_0^2 \cdot 2\phi_2(\omega_2 - \omega_1) = -FSR_0^2 \cdot 2\phi_2 \cdot 2\pi FSR_0$. According to the datasheet provided by Layertec, the dispersion term around 780 nm is $\phi_2 \approx -200$ fs^2, which gives $\Delta FSR = \Delta \approx 20$ Hz, which is in great agreement with the measured value.

We can simulate this kind of coupling by looking at the matching condition between the cavity modes, which are Lorentzian functions of width κ, and FC modes which are delta functions. By scanning the f_{rep} or FSR, we can simulate the coupling efficiency for experimental parameters. The results are presented in Fig. 4.20, where we used $N = 1300$ cavity modes and $24N$ FC modes coupled into them as we change f_{rep}. The number of modes was chosen to cover the wavelength range from 778 nm to 783 nm, closely corresponding to the measured spectrum of our frequency comb.

The FC spectrum envelope centered at 780 nm was also taken into account. In Fig. 4.20(a) we show the results for the case of no cavity dispersion (red) and for dispersion term of $\Delta = 18$ Hz as measured for our experiment (blue). If there were no dispersion, we could easily identify the optimal matching of FSR and f_{rep}, since it corresponds to the single highest peak. In this case, the dependence on f_0 also becomes important. However, with dispersion term included, the coupling efficiency drops since only a part of the spectrum can be coupled at the same time. The envelope is also much broader, since different wavelengths couple into the cavity as we change f_{rep}. In Fig. 4.20(b) a zoomed in curve of a calculated single transmission peak is shown, which shows the same shape as the experimentally measured traces. This shows excellent agreement between the measured values of dispersion and the corresponding calculated coupling curves.
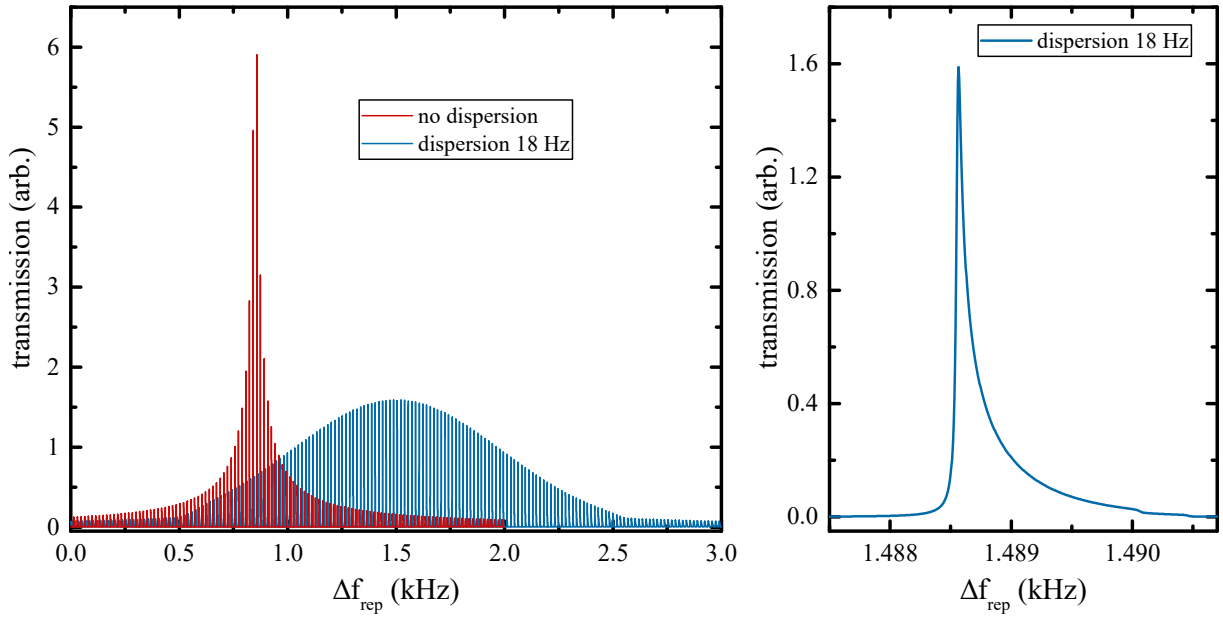
Figure 4.20: (a) Calculated FC-cavity coupling efficiency as we scan f_{rep}. For the case of no dispersion (red) the optimal matching condition is visible as the highest peak. Including the experimentally measured dispersion term $\Delta = 18$ Hz broadens the coupling envelope, and shifts it depending on the local matching conditions around the specific wavelength. (b) Zoomed in single calculated transmission peak exhibits the same shape as the experimentally measured one, indicating great agreement between the theoretical model and experimentally determined cavity dispersion. For calculations, cavity modes are Lorentzian functions of width $\kappa = 2\pi \cdot 150$ kHz and FC modes are delta functions. The number of cavity modes is $N = 1300$, covering a wavelength range from 778 nm to 783 nm, with $24N$ FC modes coupling into them as f_{rep} is scanned.

4.3.2 Locking scheme

To remove the influence of the cavity locking beam on the atomic motion, we now use a weak far-detuned 852 nm laser, referenced to the cesium cooling transition. This way we make sure the atoms only interact with FC light inside the cavity. A simplified experimental setup is shown in Fig. 4.21(a), and the overview of the locking scheme in Fig. 4.21(b). The cooling laser is locked to the rubidium cooling transition via polarization spectroscopy and is also used as a reference for optical locking of the frequency comb. A part of the beam can also be coupled into the cavity using an AOM, to monitor the relative frequency between the rubidium transition and the nearest cavity modes. The cesium laser (Moglabs CEL cateye laser) is used to stabilize the cavity length. We directly modulate the laser frequency by applying a 10 MHz modulation to the laser current. The part of the beam is split for the error signal generation using frequency-modulated saturated absorption spectroscopy. The spectroscopy beam is modulated as it passes through the cesium vapour cell, and the sub-Doppler peaks are visible on the photodiode. By
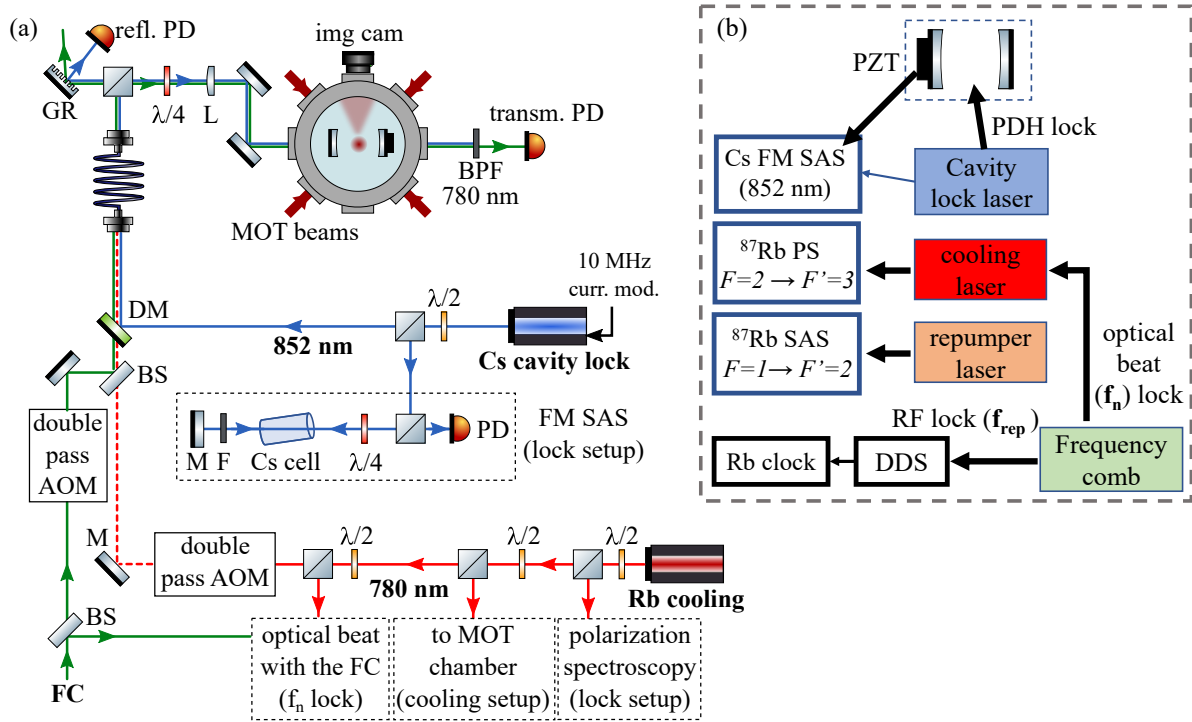
Figure 4.21: (a) Experimental setup and (b) locking scheme for stabilization of different lasers. A part of the cooling laser is also used as a reference for the FC lock, and another can be coupled into the cavity to monitor the distance between cavity modes and the rubidium resonances. Cesium laser is used to stabilize the cavity. It is frequency-modulated with a 10 MHz signal and coupled into the cavity to generate the PDH error signal. A part of the beam is split for FM-SAS and the generation of an error signal corresponding to cesium hyperfine transitions at 852 nm. The FC is locked by stabilizing two degrees of freedom, as shown in Fig. 3.5. The repumper laser is locked as described in previous section, using saturated absorption spectroscopy. BS - beam splitter, M - mirror, $\lambda/2$ ($\lambda/4$) - half (quarter)-wave plate, PD - photodiode, AOM - acusto-optic modulator, DM - dichroic mirror, L - lens, GR - diffraction grating, F - optical filter, BPF - bandpass optical filter

demodulating the phododiode signal, we extract the dispersive error signals for each peak, as shown in Fig. 4.22. The rest of the beam is coupled into the cavity to generate the PDH error signal. We use the same signal generator to modulate the laser current and to demodulate the two photodiode signals for error generation. We lock the cesium laser to the cavity by applying fast and slow feedback to the laser current and piezo, respectivelly. We then lock the cavity frequency by stabilizing the cavity length using the FM-SAS error signal and applying the feedback (Newfocus LB1005) to the cavity PZT.

Locking of the FC is the same as described in Chapter 3. The repetition frequency f_{rep} is referenced to a DDS signal, and the error signal is fed to the FC cavity piezo. The optical frequency f_n is stabilized by locking the beat frequency f_{beat} between the Rb cooling laser and
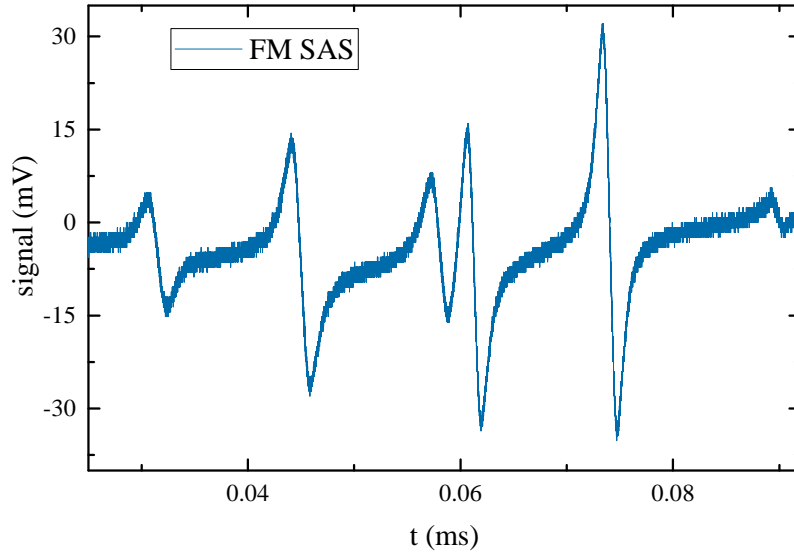
Figure 4.22: Error signal generated using frequency-modulated saturated absorption spectroscopy in a cesium vapour cell. Each dispersive signal corresponds to a hyperfine transition (and the cross-over peaks) in cesium D2 cooling line on 852 nm.

the FC mode f_n, feeding the error signal to the pump diode current. The FC lock is therefore independent from the cavity, so the FC light can be freely switched on/off and frequency-shifted around the cavity modes. We manually adjust the DDS reference values for f_{rep} and f_{beat} so that matching between the FC modes and cavity modes is achieved. Once we lock the FC, fine-tuning with the cavity is achieved by changing the frequency on the AOM in a double-pass configuration, effectively changing f_0. The same could be achieved by changing the beat frequency f_{beat}, but this means changing the locking points. AOM is a preferred option as it doesn't influence the FC locking stability.

4.3.3 Longitudinal pumping effects

Signature of the interaction in transmitted spectrum. We first look at the interaction of FC with atoms in the cavity by continuously loading the MOT cloud in the center of the cavity instead of letting it fall into it, while we scan the cavity FSR. The effect of the interaction are dips in FC transmission, as seen in Fig. 4.23. The dips occur in every transmission peak as the cavity length is scanned, meaning that the interaction exists for all matching conditions of f_{rep} and FSR. This shows that the dips in transmission are not a consequence of the interaction of atoms with a single, near-resonance FC mode, but with a multitude of FC modes. The depth of the dips also depends on the number of loaded atoms in the cloud, which is a clear signature
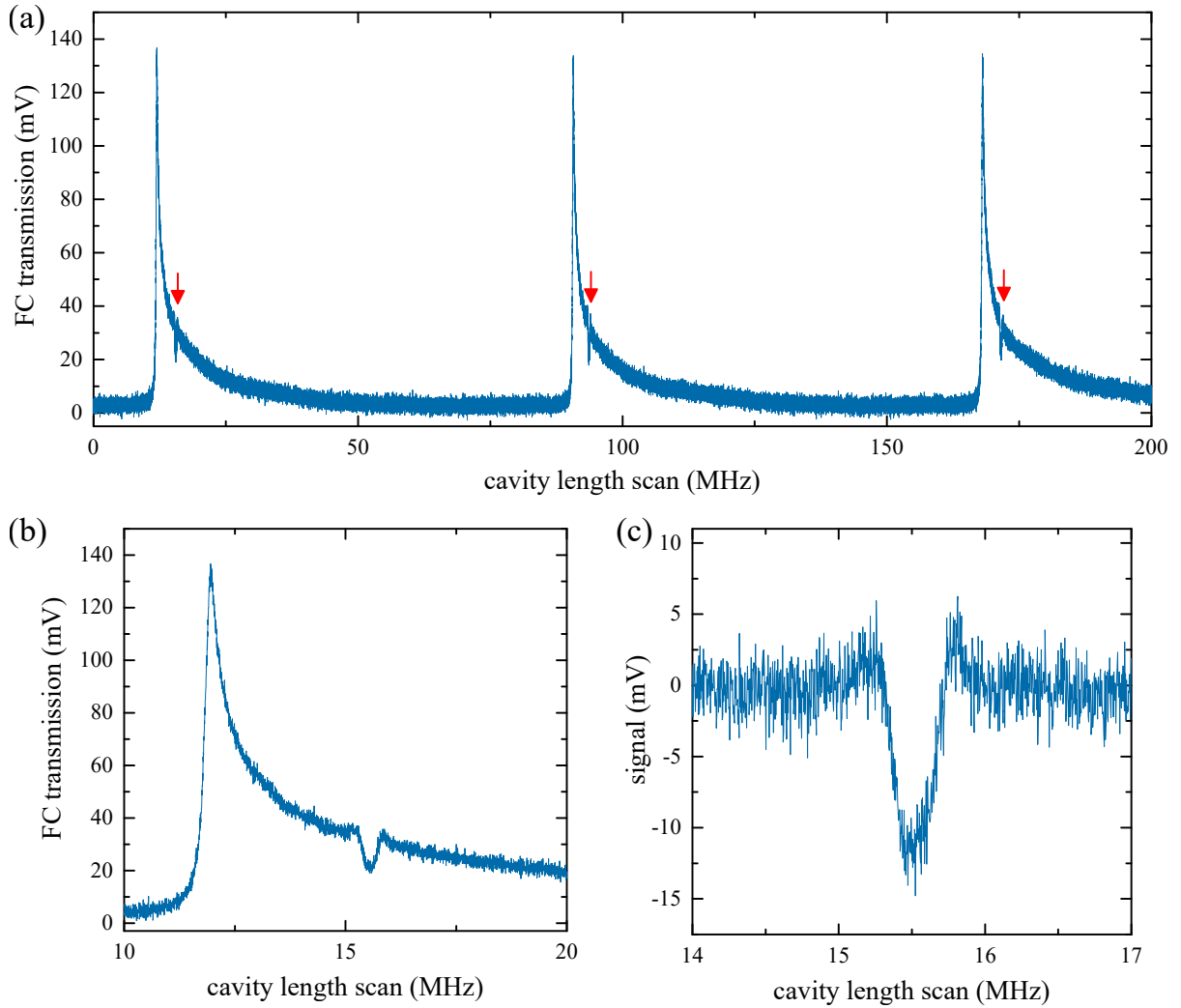
Figure 4.23: (a) Dips in FC transmission due to interaction with atoms loading in the center of the cavity, as we scan the cavity length. Occurrence of dips for every transmission peak, i.e. for every $f_{rep} - FSR$ matching condition means that the interaction is not due to a single FC mode near atomic resonance, but a collective lightshift of off-resonant FC modes. Zooming in on a single curve (b) shows that there's also an increase of transmission around the dips, as can be seen in (c) where the transmission baseline is subtracted.

of collective interaction of atoms in the cavity with the FC light. Due to collective lightshift, a group of cavity modes are pushed off-resonance, which leads to a decrease of coupled FC light. However, as can be seen in Fig. 4.23(c), increase in transmission due to collective light-atom interaction can also be visible. In this region, the collective interaction shifts the cavity modes so that more FC light is coupled into the cavity.

It was also measured that the position of the dip relative to the corresponding transmission peak changes as the cavity FSR is scanned, so the dips can be closer to the peak or further

away in the wings (this is only slightly visible in Fig. 4.23(a), the shift is significant on a larger scan range). To understand this, we look into the spectrum of the transmitted FC light, which was discussed in the last subsection in the discussion about cavity dispersion, and shown in Fig. 4.18 and 4.19. In Fig. 4.18 we chose a transmission peak for which we locally matched f_{rep} and FSR around 782 nm, and shifting the frequency f_0 led to splitting into two spectra, one moving toward lower wavelengths and the other toward higher. For the interaction dip located far on the transmission wing, it means we locally coupled wavelengths away from 780.24 nm, where the light is too far detuned from the resonance for the interaction to be visible. This is shown in Fig. 4.24(a). As we move f_0, the spectrum closer to 780.24 nm starts coupling into the cavity, and the interaction becomes significant, leading to collective coupling and increased transmission, as marked with an arrow. The light of the cooling laser is also recorded on the optical spectrum

Figure 4.24: Spectrum of the transmitted FC light during interaction with a continuously loaded MOT cloud when the dip in transmission is in the tail of the transmission curve. (a) Centrally coupled spectrum is around 782 nm and splits as we change Δf_0^{FC}, bringing the peak closer to 780.24 nm, which results in enhanced coupling and increase of transmission, marked by arrow. (b) Zoomed in spectrum around 780.24 nm for several values of Δf_0^{FC}. A weak cw cooling light is recorded as a reference for the resonant frequency of the atoms. Collective interaction induces lightshift that couples light red- or blue-detuned from the the cavity, depending on the detuning from the atomic resonance.

analyser, serving as a reference of the atomic resonance frequency in Fig.4.24(b). We see that as we scan Δf_0^{FC}, the coupled spectrum moves from the red side of the atomic frequency towards the blue. On the red side, the FC light is still red detuned from the near-resonant cavity modes and the lightshift is negative so FC combs will couple into the cavity, increasing the overall

transmission on the red side of the atomic resonance. On the blue side, the lightshift is positive and the opposite happens. Since the FC modes are blue detuned from the cavity, only the cavity modes on the blue side of the atomic resonance will be shifted, leading to increased coupling. These are the two regimes for which increased coupling occurs, corresponding to the increase of transmission around the dip seen in Fig. 4.23(c). For the values of Δf_0^{FC} for which the coupled spectrum is around 780.24 nm (which is between $\Delta f_0^{FC} = 2.8$ MHz and $\Delta f_0^{FC} = 3.6$ MHz in Fig. 4.24(b)), the collective interaction shifts all the coupled modes out of resonance, leading only to a loss of coupling and the dip in transmission.

By choosing another matching of f_{rep} and FSR and coupling the spectrum closer to 780 nm, we bring the interaction dip closer to the transmission peak. This can be seen in Fig. 4.24, where on the transmission peak, for $\Delta f_0^{FC} = 0$, there is already a sharp cut-off of transmitted spectrum around 780.24 nm, due to lightshift of the cavity modes out of resonance with the cavity, leading to reduced transmission. For other values of Δf_0^{FC}, the increase on the red or blue side of the spectrum can be again achieved as explained. This means that by choosing a local matching of f_{rep} and FSR we can select which part of the FC spectrum the atoms can interact with and how much we need to shift the FC frequency to achieve a significant effect of the interaction.

Signature of interaction in time-of-flight imaging of the cloud. In the results so far, the atoms have been loading in the MOT continuously so that we can sample the transmitted light on an optical spectrum analyser. Now, we look at the signature of the interaction during TOF, by imaging the cloud's spatial distribution. We load the cloud in the cavity, and turn off the MOT beams. We then switch on the FC beam and let it interact with the cloud for 5 ms, after which we turn off the beam and let the cloud expand freely during TOF. We identified two experimental regimes, labelled "cooling" and "heating" regime, occuring when FC light around 780 nm is coupled into the cavity. The images of the atomic cloud for these two regimes are shown in Fig. 4.26, where we show the distribution along the cavity axis in and a 2D image of the cloud. The two regimes are very distinct and have clear effects on atomic distribution during TOF. The cooling regime occurs for blue detunings of the FC frequencies from the cavity resonances, $\Delta_c > 0$, and the atoms are compressed along the cavity axis, seen in both 1D and 2D images of the cloud's distribution. The heating regime occurs for red detunings, $\Delta_c < 0$, and the atoms are stretched along the cavity axis. This is in contrast with the expected behavior, which predicts cooling (heating) for red (blue) detunings. However, this prediction is valid for red-detuned light from the atomic resonance, $\Delta_a < 0$. In the case of FC interaction, there can be modes on both sides of atomic resonance. For example, for $\Delta_a > 0$, cooling can occur for $\Delta_c \geq 0$. We
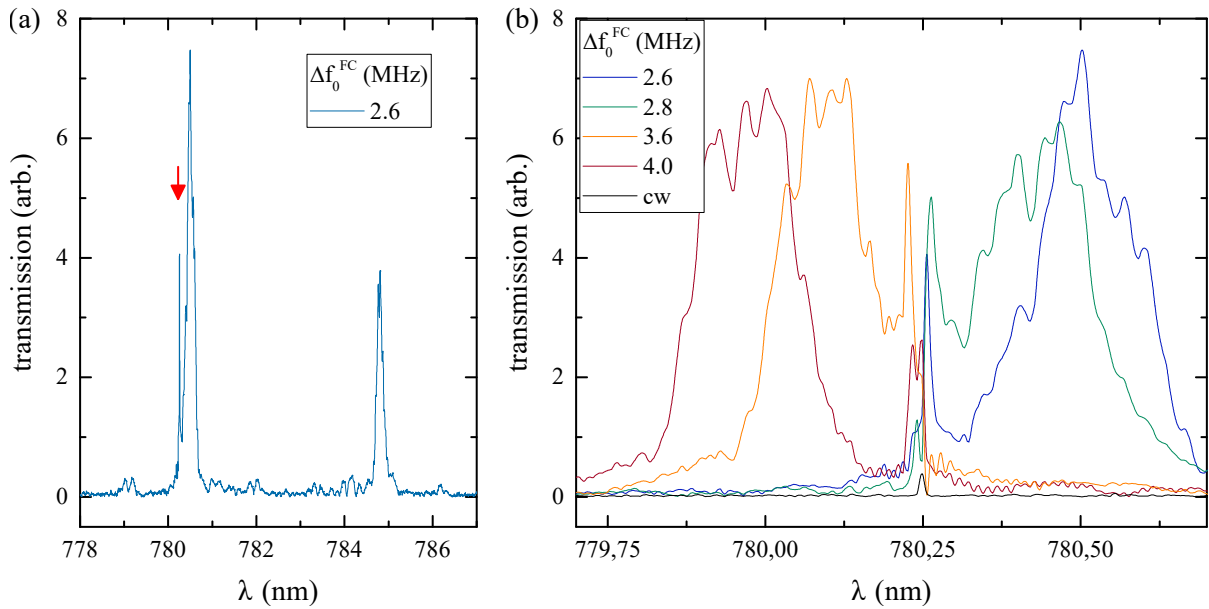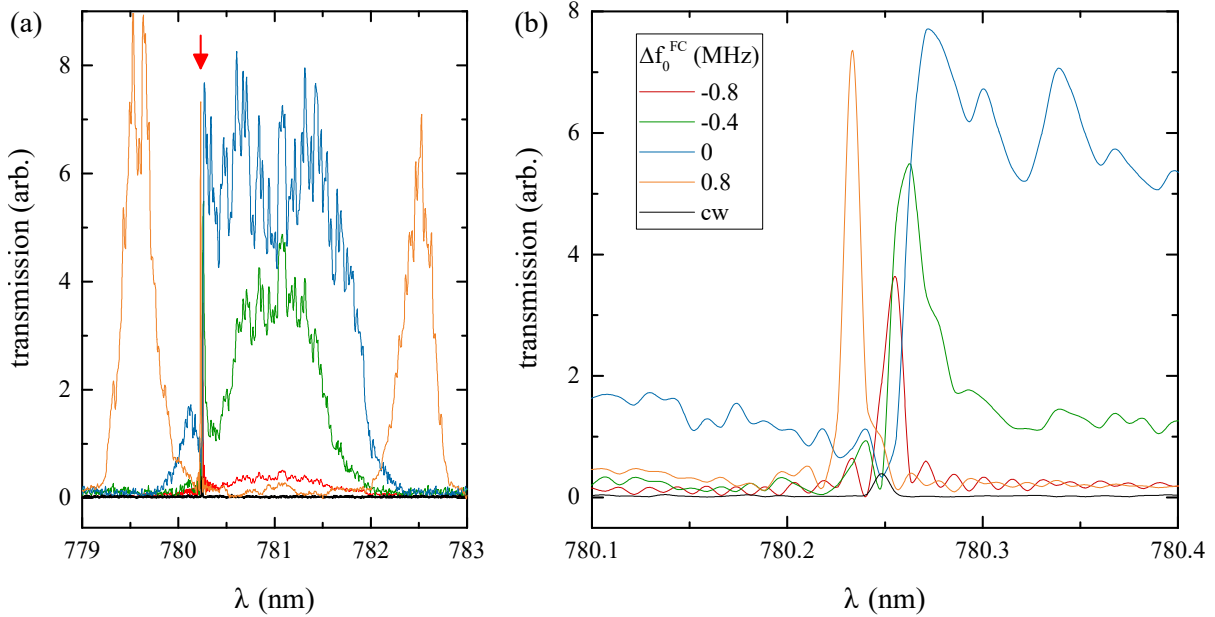
Figure 4.25: Spectrum of the transmitted FC light during interaction with a continuously loaded MOT cloud when the dip in transmission is near the peak of the transmission curve. (a) Centrally coupled spectrum is around 781 nm and a part of it is already near atomic resonance, leading to a cut-off of transmitted light on the transmission peak, for $\Delta f_0^{FC} = 0$. (b) Zoomed in spectrum around 780.24 nm for several values of Δf_0^{FC}. A weak cw cooling light is recorded as a reference for the resonant frequency of the atoms.

checked the possibility that this effect is just a signature of interaction with a single resonant FC mode. For this, we coupled the resonant 780 nm cw light into the cavity during the locking procedure, so we know where the closest cavity modes are compared to the atomic resonance. Since the cavity FSR is around 2 GHz, the largest Δ_a is around 1 GHz, i.e. the closest FC modes coupled into the cavity will be ± 1 GHz detuned from the atomic resonance. By choosing other locking points, we can bring the cavity modes closer to the atomic resonance on either red or blue side. We concluded that the effects in Fig. 4.26 are not a signature of a single, nearest FC mode. If a cavity mode is near resonance on either side, no cavity effects can be visible and resonant absorption and scattering become significant. Therefore, the cooling and heating regimes are not determined by the closest single cavity mode, and are a signature of dispersive interaction of atoms with intra-cavity light, which occurs far from atomic resonance.

Identifying the relevant parameters and their values that determine between the cooling and heating regimes requires further investigation. It is necessary to know which off-resonance FC modes need to be light-shifted due to interaction, and how to eliminate the influence of the unwanted modes. Nevertheless, the results presented in Fig. 4.26 are the first experimental

(a) $\Delta_c > 0$; "cooling" regime

(b) $\Delta_c < 0$; "heating" regime
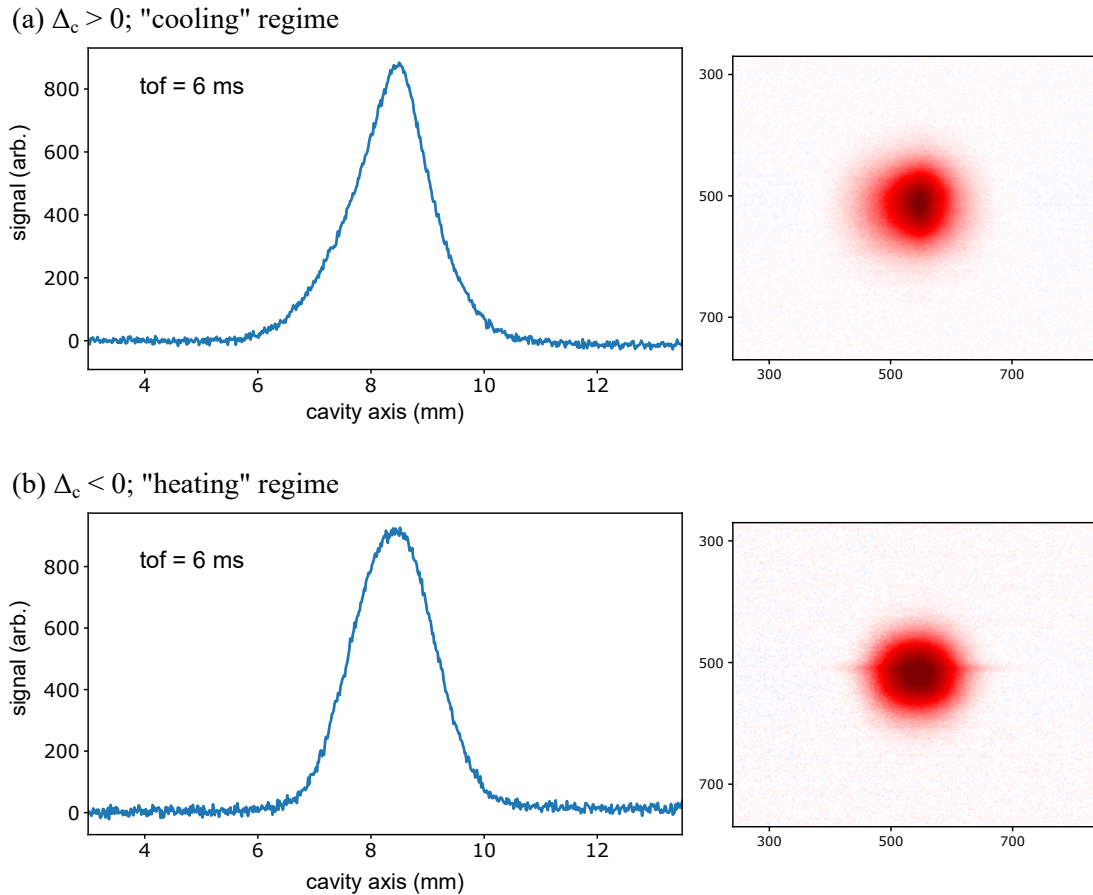
Figure 4.26: Time-of-flight signature of the interaction of an FC with atoms in a cavity. Left panels show 1D distribution of atoms along the cavity axis, and the right panels show 2D images of the cloud. (a) "Cooling" regime in which the atoms are compressed along the cavity axis. (b) In the "heating" regime the atoms are stretched along the cavity axis.

demonstration of TOF results suggesting cavity-enhanced cooling and heating effects with off-resonance FC light.

4.3.4 Transversal pumping effects

So far we pumped the atoms in the cavity longitudinally, so the atoms could feel the cavity potential only if the pump light was near the cavity resonance, i.e. some light had to be coupled into the cavity and was then strongly enhanced. By switching to the transversal pumping geometry, we illuminate the atoms from the side, which loosens the requirement of cavity coupling. To switch the geometry, we put a beam splitted on the FC beam, so that 90% of the power is free-spaced onto the atoms in retro-reflected geometry, and 10% is coupled into the cavity so that we can lock the FC relative to the cavity modes. In this geometry, the atoms can scatter on-

and off-resonantly into free space or into the cavity. The ratio of cavity to free space scattering is almost purely geometrical, corresponding to the solid angle covered by the cavity compared to the full solid angle, and it can be shown [8] that it corresponds to the cooperativity parameter $\mathcal{C}$. However, if the scattered light is resonant with the cavity modes, scattering into the cavity mode can be enhanced when the atoms are pumped above a certain threshold intensity.

For our experiment with an FC transversal pump, we are effectively pumping the atoms with modes of 80.5 MHz repetition (f_{rep}), because now there is no 2 GHz filtering provided by the cavity FSR. By inspecting at the FC-induced force in free-space (Fig. 3.7(b) and (c)), we see that within one f_{rep} the FC modes are always near an atomic resonance, either $|F = 2\rangle \rightarrow |F' = 3\rangle$ or $|F = 2\rangle \rightarrow |F' = 2\rangle$ transition. For this reason, the free space effects along the transverse axis are dominating, and cavity effects could not be observed in any parameter range, near or far from cavity resonance.

To circumvent this issue, we put a Rb glass cell on the FC beam path and heat it to around 70 °C, so that the near-resonant FC modes are attenuated. This way, we ensure only the off-resonant modes pumping the atoms and resonant free-space effects can be suppressed. In this regime, we observed no effects of interaction of atoms with FC light, neither in light scattering nor in TOF images of the cloud. We tested this for different detunings of FC modes from cavity modes, and measured no effects. This is due to low available power per comb mode in our femtosecond laser system and in this geometry there is no strong intra-cavity enhancement as in the longitudinal pumping geometry.

Conclusion   Even though the atoms are transversally pumped with a multitude of FC modes with a smaller frequency spacing compared to longitudinal geometry, we conclude that it is still not enough power per FC mode to induce any measurable effect related to cavity-enhanced cooling/heating or trapping of atoms. For future research in transverse FC pumping geometry, an outlook and some upgrade ideas for the experiment are presented in the next chapter.

Chapter 5

Thesis summary and outlook

5.1 Summary of this Thesis

In this thesis I presented the results of my research on two topics, both of which are connected with the idea of investigation of radiative forces on cold atoms in a magneto-optical trap as a result of interaction with continuous-wave and pulsed femtosecond lasers.

In the first part, we investigated the influence of collective effects on frequency-comb-induced radiation pressure force on cold ^{87}Rb atoms in free-space. We have observed reduction and broadening of the FC force as the optical thickness of the atomic cloud increases. By discussing different scattering mechanisms and their contributions to the force, we showed that for our experimental conditions a single scattering mechanism dominates the radiation pressure force. It comes as a result of progressive attenuation of light intensity in the cloud due to diffuse scattering of light, i.e., the shadow effect. The influence of the off-resonance FC modes on the FC–atom interaction is minor and can be neglected even in the case of increased cloud optical thickness, and models developed for cw excitation can be readily applied even for FC interaction. For the applications of FC cooling in free-space and for near-resonant excitation, our results show that a semi-classical approach based on the Beer-Lambert law is sufficient to describe the FC-induced force up to $b_0 \approx 20$.

The results of this topic were published in a peer-reviewed paper where I am the first and the corresponding author (see Publications). These results contribute to the understanding of scattering of the FC light by an dense ensemble of cold atoms in free space, which is of importance for FC applications in the field of cooling, quantum communication, and light–atom interfaces based on structured and disordered atomic systems.

In the second part of my research, the atoms were located in the center of a high-finesse optical cavity, and pumped longitudinally (through the cavity mirrors) or transversally with cw

and FC light. Using a cw laser pump, we observed a bimodal spatial distribution of atoms during time-of-flight (TOF) imaging as a consequence of interaction of atoms with a cavity standing wave potential. The fraction and temperature of atoms captured in the standing wave increases with the potential depth. We can capture up to 20% of atoms from the loaded MOT cloud, with temperatures less than 10 μK, which is significantly below the initial cloud temperatures of 60 μK and 150 μK. By comparing the TOF images for red- and blue-detuned standing wave potentials, where we observed the same bimodal distribution in both cases, we showed that the effect of the standing wave trap is the same regardless of the atomic detuning. Using numerical simulations, we concluded that our experimental results using cw pump can be explained as a consequence of interaction of atoms with a conservative standing wave potential, and the inclusion of collective cavity-enhanced effects are not necessary. Additionally, we showed that for deep optical lattices, the momentum distribution of atoms along the lattice axis does not retain its initial Maxwell-Boltzmann (M-B) distribution. However, the M-B distribution still gives a very good estimate for the temperature of atoms. The deviation from M-B distribution becomes significant only for very large potential depths ($U_0 \approx 1$ mK), which is usually above the typical experimental values. Therefore, for most experiments, assuming a Gaussian M-B distribution of atomic velocities is a very good estimate for the temperature measurements.

By using an FC pump in the longitudinal geometry, we observed the signature of interaction in FC transmission through the cavity and in TOF images. We showed that these effects are not a consequence of a single, resonant FC mode, but of a dispersive interaction of a multitude of FC modes with atoms inside the cavity. In light transmitted from the cavity, we observe enhanced scattering due to dispersive interaction with atoms, which brings the cavity modes on resonance with the FC modes. This dispersive interaction is in good agreement with theoretical expectations for both red and blue detunings of FC and cavity modes from the atomic resonance. In TOF images of atomic distribution, we show signatures of cooling and heating, corresponding to two different experimental regimes. These results present the first experimental demonstration suggesting cavity-enhanced cooling and heating effects with off-resonance multi-mode FC light.

The results of this research topic are in preparation to be submitted as a publication.

5.2 Outlook

In the transverse FC pumping geometry, even though the atoms are pumped with a multitude of FC modes, we saw no measurable effect related to cavity-enhanced cooling/heating or trapping of atoms. To continue the research in transverse FC pumping geometry, a few upgrades of the

experiment could be implemented. The most important one is to increase the available intensity per FC mode. For this, an additional fiber amplifier could be bought and used to increase the output power of our FC laser system. Likewise, the size of the FC beam could be focused tightly at the position of atoms to increase the intensity even further. However, a small beam means that we could interact with only a small fraction of atoms from the original MOT cloud, so most of the atomic sample would just be a source of noise. To solve this, it would be useful to implement a far off-resonance dipole trap (FORT) that would allow us to hold a small sample of atoms trapped for a longer time (10s of miliseconds) in the center of the optical cavity. This would allow not only that the focused FC beam interacts with the whole trapped sample, but to also increase the interaction time during the whole trapping period. Usually, a small number of atoms is trapped in a FORT compared to an initially loaded MOT, and for small samples the absorption imaging technique is more sensitive compared to the fluorescence imaging. If future experiments continue along the path of using a FORT with atoms in a cavity, it would be useful to implement absorption imaging for TOF measurements. To implement absorption imaging, some redesigning of the optical setup around the vacuum chamber is necessary, due to a limited number of available viewports and optical paths on the vacuum chamber.

References

[1] H. J. Metcalf and P. van der Straten. *Laser Cooling and Trapping*. Springer-Verlag, New York, 1999.

[2] C. Cohen-Tannoudji, S. Chu, and W. D. Phillips. The nobel prize in physics 1997. `https://www.nobelprize.org/prizes/physics/1997/summary/`.

[3] E. A. Cornell, W. Ketterle, and C. E. Wieman. The nobel prize in physics 2001. `https://www.nobelprize.org/prizes/physics/2001/summary/`.

[4] N. Šantić. *Synthetic Lorentz force for neutral atoms*. Doctoral Thesis. Faculty of Science, University of Zagreb, 2018.

[5] D. M. Stamper-Kurn. *Cavity Optomechanics with Cold Atoms. In: Aspelmeyer, M., Kippenberg, T., Marquardt, F. (eds) Cavity Optomechanics. Quantum Science and Technology*. Springer, Berlin, 2014.

[6] H. Ritsch, P. Domokos, F. Brennecke, and T. Esslinger. Cold atoms in cavity-generated dynamical optical potentials. *Rev. Mod. Phys*, 85, 2013.

[7] H. W. Chan, A. T. Black, and V. Vuletić. *Phys. Rev. Lett.*, 90:063003, 2003.

[8] M. Hosseini, Y. Duan, K. M. Beck, Y. Chen, and V. Vuletić. *Phys. Rev. Lett.*, 118:183601, 2017.

[9] A. T. Black, H. W. Chan, and V. Vuletić. *Phys. Rev. Lett.*, 91:203001, 2003.

[10] F. Brenncke, T. Donner, S. Ritter, et al. *Nature*, 450:268–271, 2007.

[11] P. Asenbaum, S. Kuhn, S. Nimmrichter, U. Sezer, and M. Arndt. *Nat. Comm.*, 4, 2013.

[12] U. Delić, M. Reisenbauer, K. Dare, D. Grass, V. Vuletić, N. Kiesel, and M. Aspelmeyer. *Science*, 367(6480):892–895, 2020.

[13] W. Niedenzu, T. Grießer, and H. Ritsch. *EPL*, 96(4):43001, 2011.

[14] B. L. Lev, A. Vukics, E. R. Hudson, B. C. Sawyer, P. Domokos, H. Ritsch, and J. Ye. *Phys. Rev. A*, 77:023402, 2008.

[15] R. Boyd. *Nonlinear Optics*. Academic Press, 2008.

[16] J.-C. Diels and W. Rudolph. *Ultrashort Laser Pulse Phenomena*. Academic Press, 2006.

[17] D. Kielpinski. *Phys. Rev. A*, 73:063407, 2006.

[18] N. Šantić, D. Buhin, D. Kovačić, I. Krešić, D. Aumiler, and T. Ban. *Sci Rep*, 6:2510, 2019.

[19] A. M. Jayich, X. Long, and W. C. Campbell. *Phys. Rev. X*, 6:041004, 2016.

[20] D. Buhin, D. Kovačić, Fabian Schmid, M. Kruljac, V. Vulić, T. Ban, and D. Aumiler. *Phys. Rev. A*, 102:021101(R), 2020.

[21] I. Krešić, M. Kruljac, T. Ban, and D. Aumiler. *JOSA B*, 36:1758–1764, 2019.

[22] D. Main, T. M. Hird, S. Gao, I. A. Walmsley, and P. M. Ledingham. *Opt. Lett.*, 46:2960–2963, 2021.

[23] D. Hayes, D. N. Matsukevich, P. Maunz, D. Hucul, Q. Quraishi, S. Olmschenk, W. Campbell, J. Mizrahi, C. Senko, and C. Monroe. *Phys. Rev. Lett.*, 104:140501, 2010.

[24] G. Maltese, M. I. Amanti, F. Appas, et al. *npj Quantum Inf*, 6:13, 2020.

[25] R. J. Galuber, J. L. Hall, and T. W. Hänsch. The nobel prize in physics 2005. https://www.nobelprize.org/prizes/physics/2005/summary/.

[26] V. Torggler, I. Krešić, T. Ban, and H. Ritsch. *New J. Phys.*, 22:063003, 2020.

[27] V. Torggler, S. Krämer, and H. Ritsch. *Phys. Rev. A*, 95:032310, 2017.

[28] N. Hodgson and H. Webber. *Laser Resonators and Beam Propagation*. Springer, Berlin, 2005.

[29] M. O. Scully and M. S. Zubairy. *Quantum Optics*. Cambridge University Press, 2012.

[30] W. Nagourney. *Quantum Electronics for Atomics Physics and Telecommunication*. Oxford Graduate Texts, 2014.

[31] J. Dalibard and C. Cohen-Tannoudji. *JOSA B*, 6:2023–2045, 1989.

[32] R. Grimm, M. Weidemüller, and Y. B. Ovchinnikov. Optical dipole traps for neutral atoms. volume 42 of *Advances In Atomic, Molecular, and Optical Physics*, pages 95–170. Academic Press, 2000.

[33] A. Heinz. *Ultracold Strontium in State-Dependent Optical Lattices*. Doctoral Thesis. Fakultät für Physik der Ludwig-Maximilians-Universität München., 2020.

[34] D. Anderson. *Appl. Opt.*, 23:2944–2949, 1984.

[35] P. W. Milloni and J. H. Eberly. *Laser Physics*. John Wiles and Sons, Ltd, 2010.

[36] F. Adler, M. J. Thorpe, K. C. Cossel, and J. Ye. *Annual Review of Analytical Chemistry*, 3(1):175–205, 2010.

[37] V. Vuletić and S. Chu. *Phys. Rev. Lett.*, 84:3787–3790, 2000.

[38] V. Vuletić, H. W. Chan, and A. T. Black. *Phys. Rev. A*, 64:033405, 2001.

[39] P. Horak and H. Ritsch. *Phys. Rev. A*, 64:033422, 2001.

[40] M. H. Schleier-Smith, I. D. Leroux, H. Zhang, M. A. Van Camp, and V. Vuletić. *Phys. Rev. Lett.*, 107:143005, 2011.

[41] A. Dombi et al. *New J. Phys.*, 23:083036, 2021.

[42] J. K. Asbóth, P. Domokos, H. Ritsch, and A. Vukics. *Phys. Rev. A*, 72:053417, 2005.

[43] F. Brennecke K. Baumann, C. Guerlin et al. *Nature*, 464:1301–1306, 2010.

[44] R. H. Dicke. *Phys. Rev.*, 93:99, 1954.

[45] R. Bachelard, N. Piovella, W. Guerin, and R. Kaiser. *Phys. Rev. A*, 94:033836, 2016.

[46] W. Guerin, M. O. Araújo, and R. Kaiser. *Phys. Rev. Lett.*, 116:083601, 2016.

[47] D. A. Steck. *Rubidium 87 D Line Data*, revision 2.2.2, July 2021.

[48] A. Camara, R. Kaiser, and G. Labeyrie. *Phys. Rev. A*, 90:063404, 2014.

[49] W. Ketterle, Kendall B. Davis, Michael A. Joffe, A. Martin, and David E. Pritchard. *Phys. Rev. Lett.*, 70:2253, 1993.

[50] I. Yavin, M. Weel, A. Andreyuk, and A. Kumarakrishnan. *American Journal of Physics*, 70:149, 2002.

[51] T. Bienaimé, S. Bux, E. Lucioni, P. Courteille, N. Piovella, and R. Kaiser. *Phys. Rev. Lett*, 104:183602, 2010.

[52] S. Bromley, B. Zhu, M. Bishof, et al. *Nat Commun*, 7:11039, 2016.

[53] B. Zhu, J. Cooper, J. Ye, and A. M. Rey. *Phys. Rev. A*, 94:023612, 2016.

[54] T. Bienaimé, R. Bachelard, J. Chabé, M. Rouabah, L. Bellando, P. W. Courteille, N. Piovella, and R. Kaiser. *Journal of Modern Optics*, 61:18–24, 2014.

[55] S. D. Jenkins, J. Ruostekoski, J. Javanainen, S. Jennewein, R. Bourgain, J. Pellegrino, Y. R. P. Sortais, and A. Browaeys. *Phys. Rev. A*, 94:023842, 2016.

[56] W. Guerin, M. T. Rouabah, and R. Kaiser. *JOSA B*, 64:9, 2017.

[57] M. Rouabah, M. Samoylova, R. Bachelard, P. W. Courteille, R. Kaiser, and N. Piovella. *JOSA A*, 31:5, 2014.

[58] H. Bender, C. Stehle, S. Slama, R Kaiser, N. Piovella, C. Zimmermann, and P. W. Courteille. *Phys. Rev. A*, 82:011404, 2010.

[59] R. Bachelard, P.W. Courteille, R Kaiser, and N. Piovella. *EPL*, 97:14004, 2012.

[60] T. Bienaimé, M. Petruzzo, D. Bigerni, N. Piovella, and R. Kaiser. *Journal of Modern Optics*, 58:1942–1950, 2011.

[61] J. Javanainen, J. Ruostekoski, B. Vestergaard, and M. R. Francis. *Phys. Rev. A*, 59:649, 1999.

[62] P. W. Courteille, S. Bux, E. Lucioni, K. Lauber, T. Bienaimé, R. Kaiser, and N. Piovella. *Eur. Phys. J. D*, 58:69–73, 2010.

[63] M. Araújo, I. Krešić, R Kaiser, and W. Guerin. *Phys. Rev. Lett.*, 107:073002, 2016.

[64] P. Maunz, T. Puppe, I. Schuster, et al. *Nature*, 428:50–52, 2004.

[65] E. D. Black. *American Journal of Physics*, 69(1):79–87, 2001.

[66] N. Friedman, A. Kaplan, and N. Davidson. Dark optical traps for cold atoms. volume 48 of *Advances In Atomic, Molecular, and Optical Physics*, pages 99–151. Academic Press, 2002.

[67] R. S. Watson and J. J. McFerran. *JOSA B*, 38:36–43, 2021.

Curriculum vitae

Mateo Kruljac was born in Zagreb, Croatia on February 5, 1995. From 2009 to 2013 he attended "I. gimnazija" high school in Zagreb. In 2013 he enrolled at the Department of Physics at the Faculty of Science in Zagreb, in an integrated undergraduate and graduate study of research physics. During his student days, he was an active participant in Open Door Days of the Faculty, was a member of student organizations Primus and SSHFD, and a student representative in the Scientific Council of the Physics Department. He graduated in 2018 with a masters' degree in Physics. The master thesis is titled "Coherent effects in cold atomic gases" and was done at the Institute of Physics in Zagreb under supervision of dr. sc. Damir Aumiler. Since September 2018 he is employed at the Institute of Physics as a research assistant. Since the same year he's enrolled in the doctoral study of Atomic, Molecular and Optical Physics at the Faculty of Science in Zagreb. During his doctoral study he was a teaching assistant at the Faculty of Science for experimental courses Physics Lab 2 and Microelectronics Lab. He participated in popular science events.

Refereed publications

Published

1. **M. Kruljac**, D. Buhin, D. Kovačić, V. Vulić, D. Aumiler, T. Ban, *Frequency-comb-induced radiation pressure force in dense atomic clouds*, JOSA B **39**, 1411-1418 (2022).

2. D. Buhin, D, Kovačić, F. Schmidt, **M. Kruljac**, V. Vulić, T. Ban, D. Aumiler, *Simultaneous dual-species laser cooling using an optical frequency comb*, Phys. Rev. A **102**, 021101(R) (2020).

3. I. Krešić, **M. Kruljac**, T. Ban, D. Aumiler, *Electromagnetically induced transparency with a single frequency comb mode probe*, JOSA B **36**, 1758 (2019).